The Thesis Committee for Himanshu Yadav
Certifies that this is the approved version of the following thesis:

Hydraulic Fracturing in Naturally Fractured Reservoirs and the Impact of Geomechanics on Microseismicity

APPROVED BY
SUPERVISING COMMITTEE:

Supervisor:

Mukul M. Sharma

Jon E. Olson

Hydraulic Fracturing in Naturally Fractured Reservoirs and the Impact of Geomechanics on Microseismicity

by

Himanshu Yadav, B.Tech.

Thesis

Presented to the Faculty of the Graduate School of

The University of Texas at Austin

in Partial Fulfillment

of the Requirements

for the Degree of

Master of Science in Engineering

The University of Texas at Austin

December 2011

Dedication

Dedicated to my ever loving Family

Acknowledgements

I would like to express my deepest appreciation to my advisor and mentor, Dr. Mukul M. Sharma for his constant guidance and support throughout the duration of my master's program. Without his persistent help and motivation, this thesis would not have been possible. I would also like to thank Dr. Jon E. Olson for reading this thesis and providing valuable comments and suggestions. I am also thankful to Dr. Jon Holder, Glenn Baum, and Gary Miscoe for their help and support in some of the experiments that were tried out during the research work. I am also thankful to Jin Lee for all the administrative help and support.

My stay at college was made pleasant and smooth by my friends in graduate school, who were very encouraging, supportive, and helpful throughout my research. In particular, I would like to thank Sahil Malhotra, Abhinav Sharma, Abhishek Goel, Somnath Mondal, Ripu Manchanda, Karn Aggarwal, Vikram Devarajan, Sayantan Bhowmick, and many others.

Finally, I would like to thank my loving and awesome parents and all my sisters for their endless love and support. I am also thankful to my wife, Kasey, for constant support and motivation and for providing a useful vent for both my frustration and success. Without my family, this thesis would not have been possible.

Abstract

Hydraulic Fracturing in Naturally Fractured Reservoirs and the Impact of Geomechanics on Microseismicity

Himanshu Yadav, M.S.E.

The University of Texas at Austin, 2011

Supervisor: Mukul M. Sharma

Hydraulic fracturing in tight gas and shale gas reservoirs is an essential stimulation technique for production enhancement. Often, hydraulic fracturing induces fracture patterns that are more complex than the planar geometry that has been assumed in the past models. These complex patterns arise as a result of the presence of planes of weakness, faults and/or natural fractures. In this thesis, two different 3D geomechanical models have been developed to simulate the interaction between the hydraulic fracture and the natural fractures, and to observe the impact of geomechanics on the potential microseismicity in these naturally fractured formations. Several cases were studied to observe the effects of natural fracture geometry, fracturing treatment, mechanical properties of the sealed fractures, etc. on the propagation path of the hydraulic fracture in these formations, and were found to be consistent with past experimental results. Moreover, the effects of several parameters including cohesiveness of the sealed natural fractures, mechanical properties of the formation, treatment parameters, etc. have been studied from the potential microseismicity standpoint. It is shown that the impact of

geomechanics on potential microseismicity is significant and can influence the desired fracture spacing.

In this thesis, the presented model quantifies the extent of potential microseismic volume (MSV) resulting from hydraulic fracturing in unconventional reservoirs. The model accounts for random geometries of the weak planes (with different dip and strike) observed in the field. The work presented here shows, for the first time, a fracture treatment can be designed to maximize the MSV, when the fractures form a complicated network of fractures, and in turn influence the desired fracture spacing in horizontal wells. Our work shows that by adjusting the fluid rheology and other treatment parameters, the spatial extent of MSV and the desired fracture spacing can be optimized for a given set of shale properties.

Table of Contents

List of Tables

List of Figures

Chapter 1: Introduction

Hydraulic fracturing is a very common and an important stimulation technique for production enhancement in the oil and gas industry. It is basically a process of initiating and subsequently propagating a crack (or, fracture) in the subsurface rock layer by means of a pressurized fluid. This fracture then acts as a conductive conduit through which hydrocarbons stored in the rock flow to the wellbore thereby increasing production rates and extending the life of the reservoir (Figure 1-1). It was first used more than 100 years ago in 1903, but the first commercial fracturing treatment was performed in 1948. The treatment was so successful that by the end of 1955 more than 100,000 fracturing treatments had been performed. Even today, it remains one of the most extensively used stimulation technique to improve wells' productivity. In 1995, it was reported that since 1950s, approximately 70% of the gas wells and 55% of the oil wells in North America region have been hydraulically fractured in one way or the other. Initially, it started only as a stimulation treatment for secondary recovery of the production wells since exploration and production was mainly confined to reservoirs having moderate to high permeability. However, with time, oil companies started to explore and produce from not so permeable reservoirs and hydraulic fracturing then became a treatment design for primary recovery. Especially today, as conventional permeable reservoirs are hard to find and due to the subsequent rise in drilling activity in unconventional reservoirs like shale gas, tight sands, coalbed methane etc., where permeability can go as low as nanodarcy, production from these reservoirs without a comprehensive fracturing treatment is inconceivable.

Hydraulic fracturing is used not only for hydrocarbon production enhancement but also for stimulating groundwater wells, solid waste disposal, injection wells, fault reactivation in mining, measurement of in-situ stresses etc.

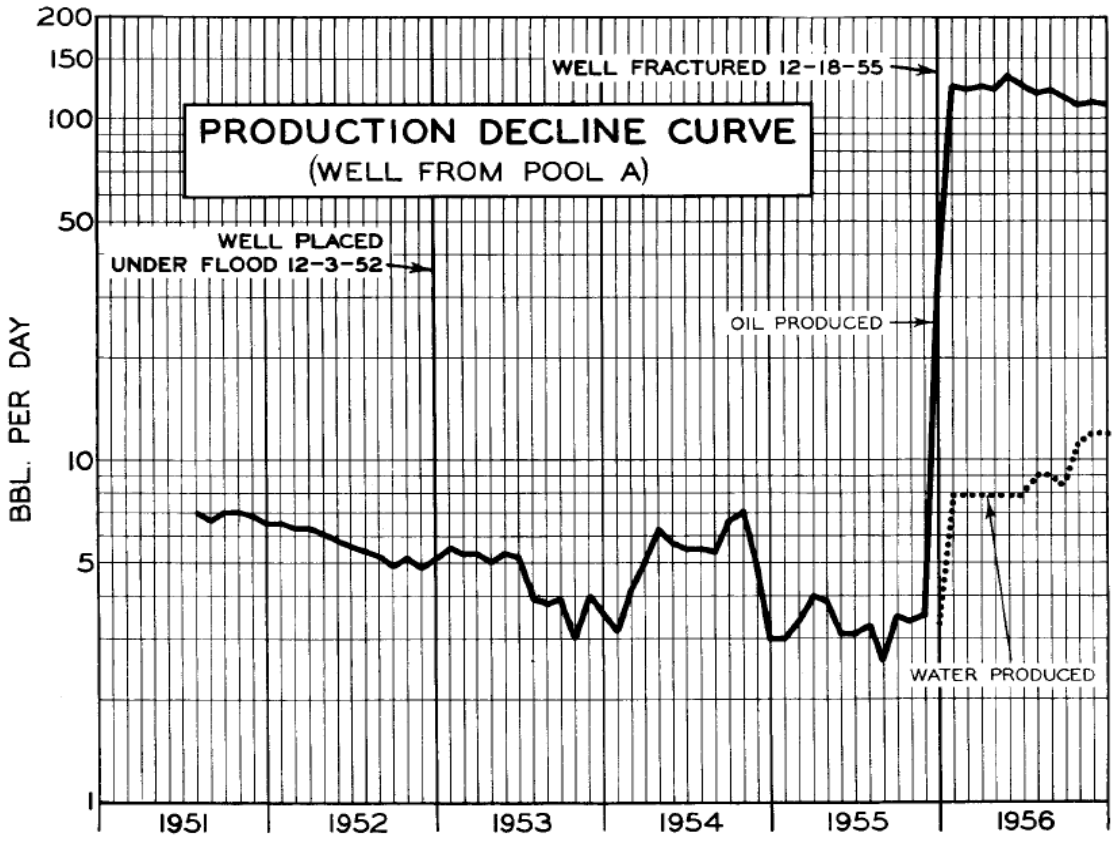

Figure 1-1: Production profile of a well before and after the hydraulic fracture treatment. (from Paul and Taylor, 1958)

Hydraulic fracturing consists primarily of four stages. In the first stage, a large volume of special fluid(s) is injected into the prospective producing formation at a very high rate that causes the formation rock to split (or crack open). This stage is termed as the “Pad” and depending on the formation permeability; it could comprise 10-90% of the total fluid volume. In the next stage, a slurry of additional fracturing fluid mixed with

sorted sand (termed as proppant) is pumped into the reservoir. These sand particles, or proppant, help in keeping the created fracture open even when the pump pressure is relieved. In the third stage, a tubular volume of clean fluid is pumped to clear tubulars of proppant. This is termed as the “Flush” stage. In the last stage, known as the “Recovery” stage, fracturing fluid is recovered by flowing back the well. Typically, the widths of these propped fractures are on the order of 0.5 in. or less, while the lengths could be quite large (on the order of 500 ft) depending on the total fluid injected. This entire fracturing process generally takes only a few hours and the resultant production may jump up to 20 times.

Laws of mechanics state that the growth of the hydraulic fracture will be perpendicular to the least compressive principal stress. For most reservoirs at large depths, the least principal stress is in the horizontal direction, thus making these fractures grow in a vertical plane. The traditional view of the fracturing assumes fracture geometry to be simple bi-wing planar as shown in the Figure 1-2 below.

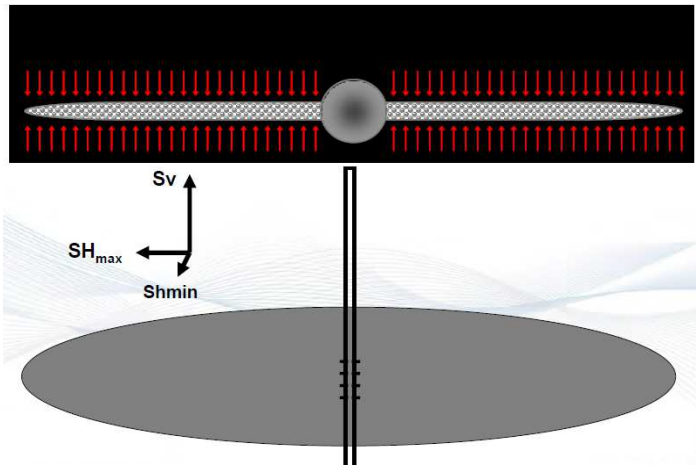

Figure 1-2: Top view and side view of the traditional hydraulic fracture geometry (from LaFollette, 2010)

However, nearly 60% of the total recoverable onshore natural gas (in U.S.) is stored in unconventional plays (Navigant Consulting (2008)). As mentioned earlier, these unconventional reservoirs have very low permeability (from few nanodarcy to few hundred nanodarcy). Thus, hydraulic fracturing is the key to successfully develop these unconventional plays. Equally important is the presence of natural fractures (sealed or open) in these reservoirs. The interaction between the hydraulic fracture and the natural fractures is critical to the success of any stimulation treatment. To be most effective, hydraulic fracture should cross and connect the natural fracture system. However, in practice, it is not always the case, and complex fracture geometry is usually created (Figure 1-3). This complex fracture network is sometimes also referred to as Stimulated Rock Volume (SRV). Extent of this SRV and fracture design in these naturally fractured formations is poorly understood, and provides a motivation for the work described in this thesis.

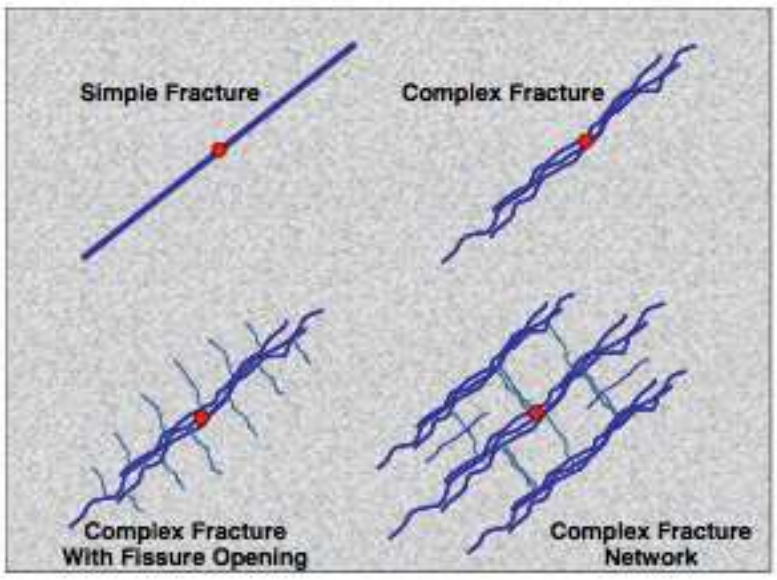

Figure 1-3: Schematic of complex fracture geometries observed (from Warpinski, 2008)

New technologies, like microseismic mapping, are commonly used to estimate the size and orientation of hydraulic fractures, and thereby the extent of the SRV created. Microseismic activity is typically measured by placing an array of geophones in a nearby wellbore, and by mapping the locations of small seismic events associated with the growing hydraulic fracture, an approximate geometry of fracture can be estimated. Apart from microseismic, tiltmeter arrays are sometimes also used to monitor the fracture growth in the sub-surface. The microseismic maps shown in the Figure 1-4 show the difference in the hydraulic fracture geometry in the conventional and the unconventional reservoirs.

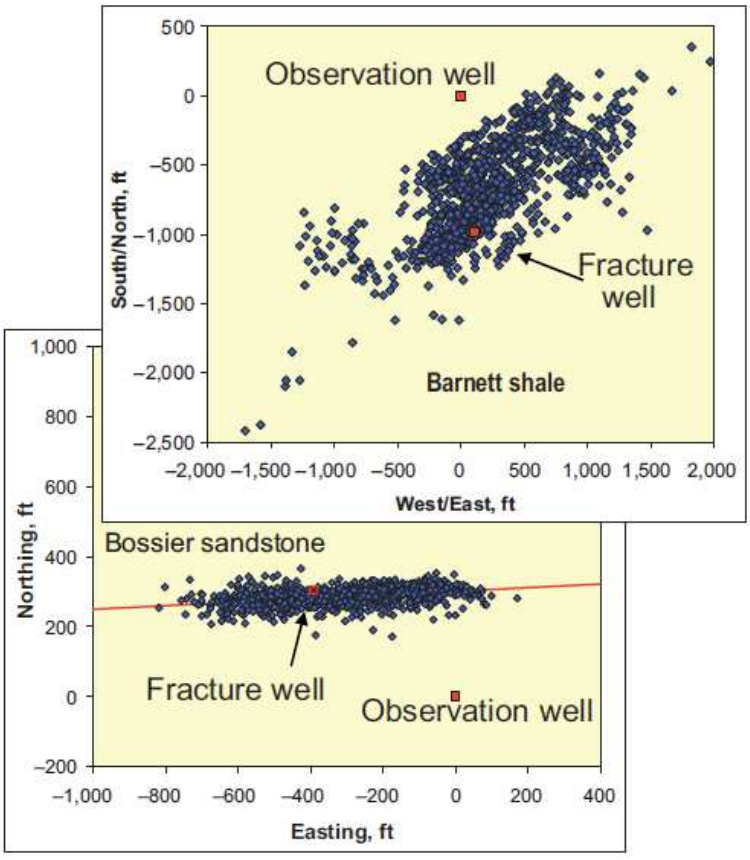

Figure 1-4: Example microseismic maps indicating complex fracture geometry (Top: from Fisher, 2005, and Bottom: from Sharma, 2004)

RESEARCH OBJECTIVES AND OVERVIEW OF CHAPTERS

The objective of this research is to analyze the hydraulic fracture interaction with natural fractures already existing in the formation. Specifically, the research objectives are as followed:

- Build a geomechanical model to simulate the hydraulic fracture interaction with natural fractures and predict the propagation path once it intersects the natural fracture
- Build a geomechanical model to predict and quantify the extent of potential microseismic activity cloud when a hydraulic fracture is created in a naturally fractured formation
- Perform a sensitivity analysis to observe the effect of different parameters on the extent of this microseismic cloud

This thesis is divided into five chapters. Chapter 2 presents the work that has been done in the past on hydraulic fracturing in conventional and unconventional reservoirs. Merits and demerits of various approaches have been compared and presented. Chapter 3 presents the theory and formulation of the geomechanical model developed to predict the fracture propagation path after intersecting with natural fractures, and to predict the microseismic cloud in naturally fractured formations. This chapter contains a detailed background on FLAC 3D (a commercial software used for all modeling purposes in this thesis). Chapter 4 provides the results obtained for different cases and discussion of those results. Chapter 5 presents the summary of the work done, conclusions reached and recommendations for future work.

Chapter 2: Literature Review

As mentioned in Chapter 1, hydraulic fracturing in unconventional reservoirs is significantly different than fracturing in conventional reservoirs. The presence of large as well as small scale heterogeneity, natural fractures/weak planes, and faults adds complexity to the fracture propagation path. Since the introduction of hydraulic fracturing to the oil and gas industry in 1940s (the concept was first introduced by Dow Chemical Company), there have been numerous attempts to model and better understand the physics of the phenomenon. However, the focus of these studies, until recently, was limited only to the conventional reservoirs. Thus, while the literature for hydraulic fracturing in the conventional reservoirs is rich, literature for fracturing in unconventional reservoirs has been somewhat limited and provides scope for more research in years to come. This chapter provides the literature review for both traditional fracturing models as well as fracturing in unconventional reservoirs, and compares the two approaches.

TRADITIONAL HYDRAULIC FRACTURING MODELS

The very first systematic modeling study in the field of hydraulic fracturing was done in 1957 by Hubbert and Willis (1957). They offered a theoretical analysis of rock fracturing and concluded that the fracture should always propagate in the direction perpendicular to the least principal stress. Their theory was backed by laboratory experiments and field evidence. In the same year, Carter (1957) presented the following formula for the area of a fracture with constant width formed by injection at a constant rate with fluid loss to the formation:

$$A(t) = \frac{Q_i W}{4C^2 \pi} \left\{ e^{\left[\frac{2C\sqrt{\pi t}}{W} \right]} . erfc \left[\frac{2C\sqrt{\pi t}}{W} \right] + \frac{4C\sqrt{t}}{W} - 1 \right\} \quad (2.1)$$

where

A = area of the fracture face,

Q_i = rate of fluid injection (assumed constant),

W = constant fracture clearance, ft,

t = total pumping time, mins, and

C = a constant (measure of the flow resistance of the fluid leaking off into the formation)

His paper also gave the fracture length as a function of time for vertical fractures. However, the assumptions made in his study, including constant width of the fracture, were argued by many and led to further refinements in the fracture modeling.

The width of a vertical hydraulic fracture was first investigated by Khristianovic and Zheltov (1955) under the assumption of plane strain state in the vertical direction. This implied that the width of the fracture doesn't change in the vertical direction. Their solution, however, neglected fluid leak-off and pressure variation inside the fracture. This model was then improved by Geertsma and de Klerk (1969) as they incorporated fluid losses in their fracture model. They too assumed plain strain in the horizontal planes and thus, constant width in the vertical direction. The fracture geometry modeled by Geertsma and de Klerk is shown in the Figure 2-1 below. They were the first to suggest that in the case of a fracture propagating in a brittle solid, fluid distribution inside the fracture should be such that the faces of fracture close smoothly at the tip. This condition implied that:

$$\left(\frac{dw}{df_L}\right)_{f_L=1} = 0 \tag{2.2}$$

where

w = width of the fracture, and

f_L= fracture length

This tip condition was later proved by mathematician Barenblatt (1962) and has always been used in the hydraulic fracture simulators since then. Moreover, they presented a very simple formula to calculate the fracture width at the wellbore:

$$w_w = 2.1\times\sqrt[4]{\frac{\mu Q L^2}{Gh}} \tag{2.3}$$

where

w_w = width at the wellbore, in,

μ = fluid viscosity, cp,

Q = rate of fluid injection, bbl/min,

L = fracture length, ft,

G = shear modulus of the formation, psi, and

h = fracture height, ft

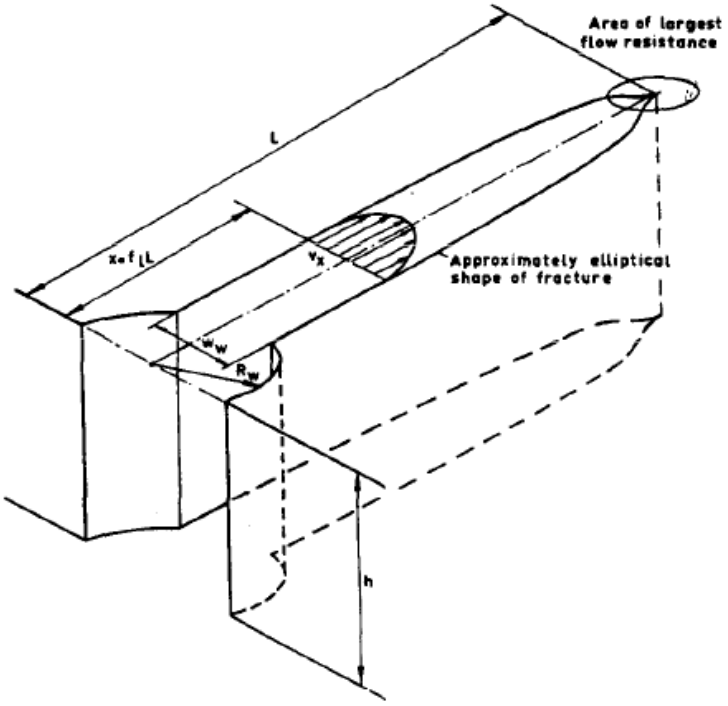

Figure 2-1: Schematic view of the fracture geometry assumed by Geertsma and Klerk (1969) (also known as KGD geometry)

In practice, assumption of plane strain is applicable only when the fracture height is much greater than the fracture length, or if there is slip at the boundaries of the pay zone.

Another comprehensive work in determining fracture width and shape was done by Perkins and Kern (1961) in what remains to be one of the most defining works in the field of hydraulic fracturing. They assumed plane strain, where the out-of-plane, non varying direction is along the length instead of the fracture height. This implied that the fracture width varies in the vertical direction and that the pressure at any section is dominated by the height of the section rather than the length of the fracture. Thus, the vertical cross-section of the hydraulic fracture is elliptical in Perkins and Kern geometry (Figure 2-2). A similar work had been done by some Russian authors, but they did not

present the formulas for fracture width under dynamic conditions (i.e. while the fracture is being created and extended). Perkins and Kern presented a simple analytical formula for the fracture width at the wellbore:

$$W = 0.38\left[\frac{Q\mu L}{E}\right]^{1/4} \tag{2.4}$$

where

W = maximum width at the wellbore, in,

Q = total pump rate, bbl/min,

μ = fracturing fluid viscosity, cp,

L = length of the vertical fracture measured from the wellbore, ft, and

E = Young's modulus of the formation, psi

In practice, this assumption of plane strain in vertical planes works well when the fracture length is much greater than the fracture height. This study, however, did not take into account the effects of fracture fluid loss and fracture volume change into the continuity equation. Thus, the above formula works well only at early times and tends to overestimate the fracture widths at large times.

This model was later modified and improved by Nordgren (1972) who used the fracture geometry assumed by Perkins and Kern in his analysis (later known as PKN geometry). He included the effects of fluid leak-off and fracture volume change in his numerical analysis of the fracture propagation. He found out that at large times, fracture length given by Carter's formula (1957) works well. However, at early times width variation plays an important role in the fracture length, which was neglected by Carter.

He also presented analytical formulas for the fracture width and length for the cases of high fluid leak-off and large times as following:

$$L(t) = \frac{q_i \sqrt{t}}{\pi C h} \tag{2.5}$$

$$W(0,t) = 4\left[\frac{2(1-\upsilon)\mu q_i^2}{\pi^3 G C h}\right]^{1/4} t^{1/8} \tag{2.6}$$

where

L = fracture length,

W = maximum width of the fracture at the wellbore,

q_i = injection rate of the fluid,

t = time,

C = fluid loss coefficient,

G = shear modulus of the formation rock,

h = fracture height,

μ = viscosity of the fracturing fluid, and

ν = Poisson's ratio of the formation rock

The two different fracture models described above differ mainly in how one approaches the problem. In the case of PKN model, focus is on the effect of fluid flow and pressure gradients within the fracture, and tip does not play an important role. However, in the KGD model, tip region plays a very important role.

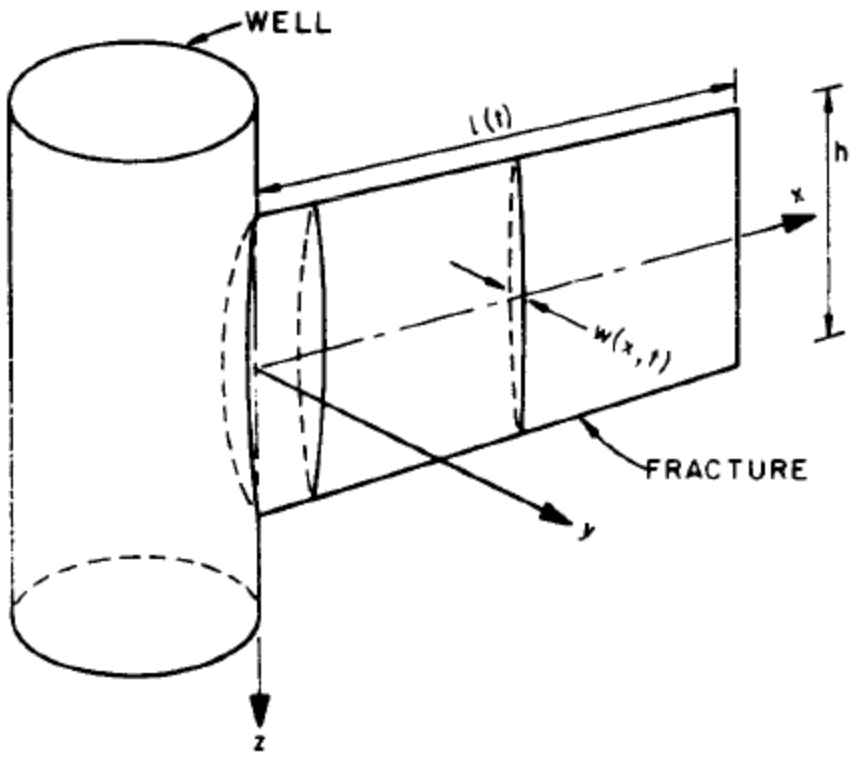

Figure 2-2: Schematic of the PKN fracture geometry. Note that the cross-section of the fracture is elliptical in shape.

Though these analytical solutions are limited to very simple planar fracture geometries in a homogeneous, isotropic medium, they do provide a valuable insight about the asymptotic behavior of the pressure distribution near the fracture tip. They also provide considerable insight in understanding the parameters and conditions that influence hydraulic fracture propagation. In the past, there have been numerous attempts to revisit these simple analytical solutions in order to have a better understanding of different fracture propagation regimes. As mentioned above, these models were limited by the assumption of two-dimensional fracture growth i.e. height was assumed to be a constant (equal to the pay zone).

One of the first attempts at 3-D fracture modeling was done by Simonson et al. (1978). They studied the effects of several parameters on the fracture height and containment from the wellbore pressure data. However, they did not take into account the actual fracture height in determining the pressure, and the fracture was assumed to be infinitely long in this analysis. Subsequent 3D fracture modeling was done by Cleary (1980), Settari and Cleary (1984), and Nolte and Smith (1981). Settari and Cleary approximated the fluid flow by 1D fluid flow in the horizontal direction (along the pay zone) and 1D fluid flow in the vertical direction. This approach, though not the most accurate, was computationally very cheap as compared to the fully coupled 3D fracturing models. Clifton and Abou-Sayed (1981) used a variational approach to model the 3D fracture propagation. They formulated the elasticity equations by an approach similar to the finite element method but was applicable to cases in which physical problem was formulated in terms of integral equations instead of differential equations. They allowed a more accurate representation of the fluid velocity in the fracture through 2D flow modeling. However, their model was computationally very expensive and required further development especially in the cases of advancing crack and non-Newtonian fluids.

Their work was extended by Thiercelin et al. (1990), where they used the boundary integral method for the displacement field, and allowed the simulation of out-of-plane growth in the vertical direction, and analyzed the effect of interfaces in the formation. Their technique allowed stable solutions with the minimum number of linear elements. Moreover, they solved the coupled elasticity and fluid problem in a single pass thereby reducing the computation time. However, there were numerical and geometrical issues associated with modeling simultaneous growth of multiple fractures in their model.

This method was also limited by the fact that it could not incorporate non-planar fractures.

Advani and Lee (1990) presented their work on a generalized three dimensional fracture propagation in a layered media. They used the finite element method as their numerical scheme to solve the governing equations. They also incorporated the capability to handle non-Newtonian fluid flow within the fracture. Their model, however, was not very efficient and stable, and also did not take poroelastic effects into account. This model too was limited to only planar fractures. Moreover, there was no grid re-meshing capability in the model, thereby increasing the computation time. Similar work on simulating the three dimensional fracturing problem was done independently by Gu and Leung (1993), Morita, Whitfill, and Wahl (1988), and, Lam, Barr, and Cleary (1986).

All the abovementioned models concentrated exclusively on coupling the fluid flow and elastic fracture-opening processes, and thus treating fracture propagation in an a-posteriori fashion. Choate (1992) developed a new three dimensional fracture simulator (GEOFRAC) that included implicit coupling of the fracture propagation criterion and associated boundary movements. Moreover, the stability of the simulator was enhanced by using an overall volume-balance criterion instead of the then conventional rock elasticity/fluid-flow coupling at the finite element level. This simulator, however, worked well for very simple cases, and could not handle any sort of heterogeneity in the formation.

Another pioneering work in the field of hydraulic fracturing was presented by the mathematicians Spence and Sharp (1985) as they laid out a self-similarity solution for the fracturing problem. Their work has been adapted by many researchers in numerical studies of hydraulic fracturing. According to their definition, any object that “looks” approximately the same on any scale is said to be self-similar. They made use of power

law self-similar relations (also tried exponential self-similar relations) between the fracturing fluid pressure and the fracture opening. Using asymptotic behavior of fracture opening at the tip from the fracture mechanics, they determined the fluid pressure by integrating the elasticity equation and used stress intensity factor as the criterion for fracture propagation.

As noted earlier, their work was then adapted with some modifications in later years to apply for numerical studies of fracturing problem. Adachi and Detournay (2002) used the proposed self-similar solution in their model, and numerically solved the problem using an explicit time-marching algorithm. Their numerical scheme incorporated moving or stretching spatial mesh (i.e. automatic re-meshing was possible) but neglected the fracture toughness. Moreover, no fluid lag between the fracture tip and fluid front was taken into account during fracture propagation in their study.

Traditionally, the numerical solutions for the fluid-driven crack problem have employed mainly two techniques to discretize the elasticity equation. First is formulating integral equations, like in displacement discontinuity method, and second is the discretization of the differential equations using finite element/finite difference methods. Yew and Liu (1993) used the displacement discontinuity method to investigate the effects of the presence of plastic zone in front of the fracture tip on the stress intensity factor. The bottomhole pressure from their model matched the higher than predicted values of bottomhole pressure from the field data. However, they assumed KGD geometry in their analysis and thus their results were limited to smaller fracture lengths. Moreover, this model too was limited to only planar fractures and other possible factors resulting in high bottomhole pressures (for example, condition of fracture opening and surface tortuosity) were not considered.

As mentioned earlier, there have been attempts to review the simple analytical solutions comprehensively over time. A significant amount of research has been carried out to obtain analytical solutions for special cases. Desroches et al. (1994) used the fact that there is usually a fluid lag inside the fracture, and that the singularity disappears as the solution is not continued up to the crack tip. They presented some analytical formulas for fluid pressure and fracture width as a function of space and time for the case of very small fracture toughness and no fluid leak-off. Lenoach (1995) extended the previous works on self-similar analytical solutions for fluid driven fracture propagation and proposed asymptotic solutions for arbitrary values of rock permeability. His analytical solution worked well for the cases of very small fracture toughness and very high leak-off (highly permeable formation). Detournay and Garagash (2003) also worked independently to investigate the near-tip region of a fluid driven crack in a permeable medium. They took into account the flow of fluid from the formation to the dry region near the tip (i.e. the region of "fluid lag") and the flow of fracture fluid back to the formation. They highlighted the importance of two variables; permeability and the crack propagation velocity. They also laid out an analytical solution for the fracture width for the case of very high propagation velocity.

A very comprehensive and efficient three-dimensional hydraulic fracturing model in a multi-layer elastic medium was developed by Siebrits and Peirce (2002). This model could incorporate various layers with random elastic properties, and used a Fourier-Transform based approach to solve the governing equations. However, the model was limited to only the planar fracture geometries and only the geomechanics aspect of the problem since all the fluid coupling effects were neglected in that study.

Simulation of non-planar fracture geometry was modeled by Olson (1995). He used the boundary element technique to simulate two-dimensional non-planar fracture

propagation from highly deviated and horizontal wells. His work focused primarily on quantifying the effects of well deviation, in-situ stress state, and fracturing fluid rheology on the fracture propagation path and width restrictions. His model assumed only a single fracture already existing along the wellbore covering the length of perforated interval and did not consider multiple, non-intersecting fractures. A similar work was later carried out by Rahman et al. (2000). He obtained closed-form analytical solutions for simple cases and compared them with his numerical model for initiation of transverse, complex multiple fractures with or without perforation.

Most of the theoretical and numerical fracturing models described in this section do not take multiple fractures or interaction of induced fracture with pre-existing natural fractures into account. With the rise in the drilling activity in the unconventional gas reservoirs (shale gas, tight gas, etc.), it has been observed that these reservoirs exhibit tremendous amount of both small-scale and large-scale heterogeneity. Moreover, these unconventional reservoirs also have pre-existing natural fractures/weak planes and bedding surfaces present in them. Thus, it is the need of the hour to migrate from the traditional fracturing models to the ones that model fracture propagation by taking all the abovementioned factors into account. The following section describes the research work that has been carried out in the literature for hydraulic fracturing in naturally fractured formations.

HYDRAULIC FRACTURING IN NATURALLY FRACTURED FORMATIONS

Experimental Studies

One of the very first studies to investigate the effect of rock heterogeneity (pre-existing fractures in particular) was carried out by Lamont and Jessen (1963). They

conducted a series of triaxial laboratory experiments on six different types of rocks. They "simulated" the existing fractures in their rock samples by creating hairline fractures of essentially zero width by cutting the rocks into two parts with a diamond saw, and replacing the two parts back together along the cut (Figure 2-3). They also used finite-width existing fractures by placing a layer of sand grains inside the fracture. They observed that in most of the successful cases, the induced fracture was able to cross the existing fracture, and orientation of induced fracture was such that it turned and intersected the existing fracture at right angles. It was also observed that the location of the point of exit on the existing fracture was not controlled by the length or the stress concentration at the tip of the existing fracture, but rather by some "flaw" or weak point in the rock matrix. However, the rates of fracture extension observed in the experiments were considerably greater than the in-filed tests, raising a possibility that fracture extension might have been unstable.

Daneshy (1974) carried out laboratory experiments on granite blocks containing three types of "flaws": crystal and matrix boundaries, small fractures (less than 0.5 in. in length), and large natural fractures. His experimental results indicated that the first two types of "flaws" had little to no effect on the overall direction of the propagation of induced fracture. In the most cases, induced fracture was able to cross the large natural fractures. He also tried to study the effect of deviatoric stresses on fracture propagation direction and concluded that in the case of hydrostatic state of stress, hydraulic fracture can propagate in any direction and is likely to follow the prevailing weakness in the rock. He, however, did not study fracture propagation direction in severely fractured reservoirs with high permeabilities.

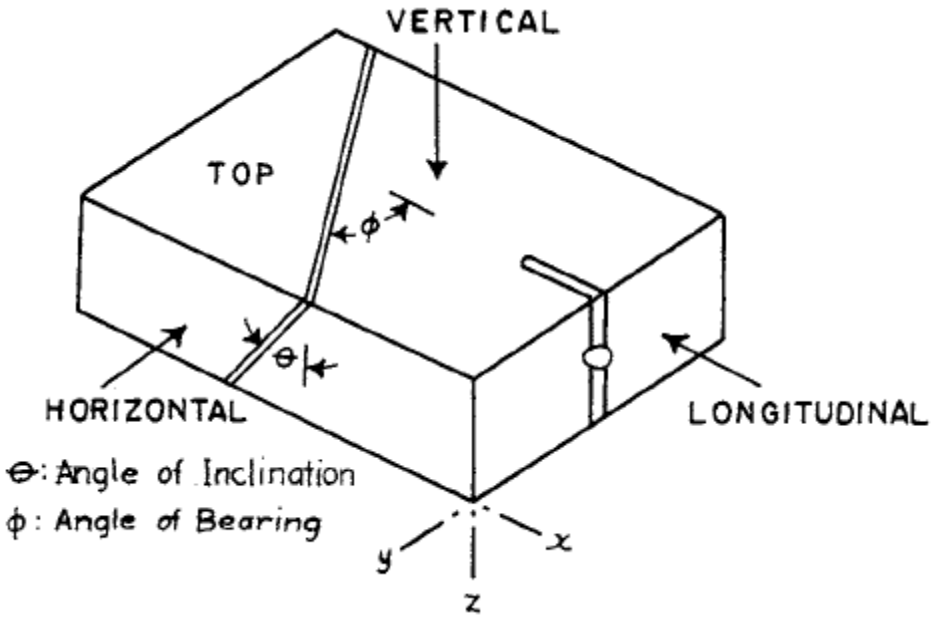

Figure 2-3: Schematic of the rock model with existing fracture used in the experiments by Lamont and Jessen (1963)

Later, Blanton (1982) conducted triaxial tests on naturally fractured Devonian shale as well as hydrostone (cement) blocks to observe and analyze the qualitative effect of angle of approach (see Figure 2-4) and differential stress on the hydraulic fracture propagation. He observed three types of interaction between hydraulic and pre-existing fractures: opening, arrest, and crossing. He concluded that at low angle of approach and low differential stress, the existing fracture opened, diverting the fracturing fluid, and preventing the hydraulic fracture from crossing. At higher angle of approach and high differential stress, hydraulic fracture crossed the pre-existing fractures (Fig. 2.5a and 2.5b).

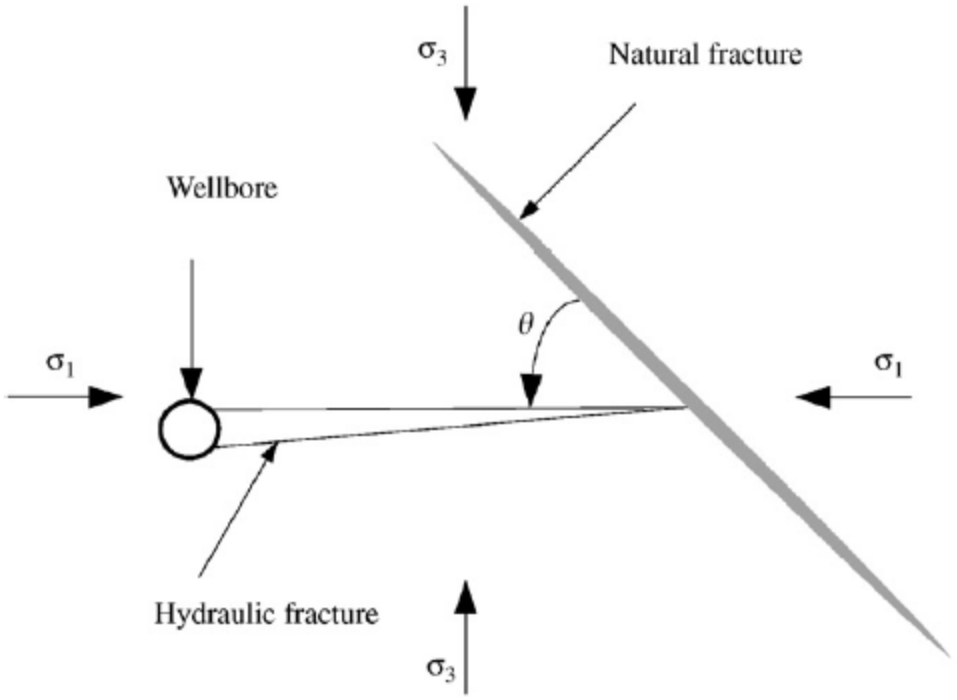

Figure 2-4: Schematic of a natural fracture affecting the propagation of a hydraulic fracture. Note that θ is called as "angle of approach". σ_1 and σ_3 denote the far-field maximum and minimum horizontal principal stresses respectively.

Blanton (1986) later also carried out a theoretical analysis, and gave a simple analytical criterion for fracture propagation path after interaction with pre-existing fractures. According to him, crossing will occur if pressure required for re-initiation is less than the opening pressure. His criterion for crossing of the hydraulic fracture is as following:

$$\frac{\sigma_1 - \sigma_3}{T_0} > \frac{1}{\cos 2\theta - b \sin 2\theta} \tag{2.7}$$

where

$$b = \frac{1}{2a}\left(v(x_0) - \frac{x_0 - l}{K_f} \right), \tag{2.8}$$

$$v(x_0) = \frac{1}{\pi}\left[(x_0 + l)\ln\left(\frac{x_0 + l + a}{x_0 + l} \right)^2 + (x_0 - l)\ln\left(\frac{x_0 - l - a}{x_0 - l} \right)^2 + c\ln\left(\frac{x_0 - l - a}{x_0 - l - a} \right)^2 \right],$$

and

$$x_0 = \left(\frac{(1+a)^2 + e^{\frac{\pi}{2K_f}}}{1 + e^{\frac{\pi}{2K_f}}} \right)^{\frac{1}{2}} \tag{2.9, 2.10}$$

where σ_1 and σ_3 are the maximum and minimum horizontal principal stresses as shown in Fig. 2-4, a is the length of zone of slippage, l is the half length of open section of the natural fracture, θ is the angle of approach, and K_f is the coefficient of friction. This criterion was in fair agreement with the experimental results and it was observed that the angle of approach was the most sensitive parameter in determining propagation path.

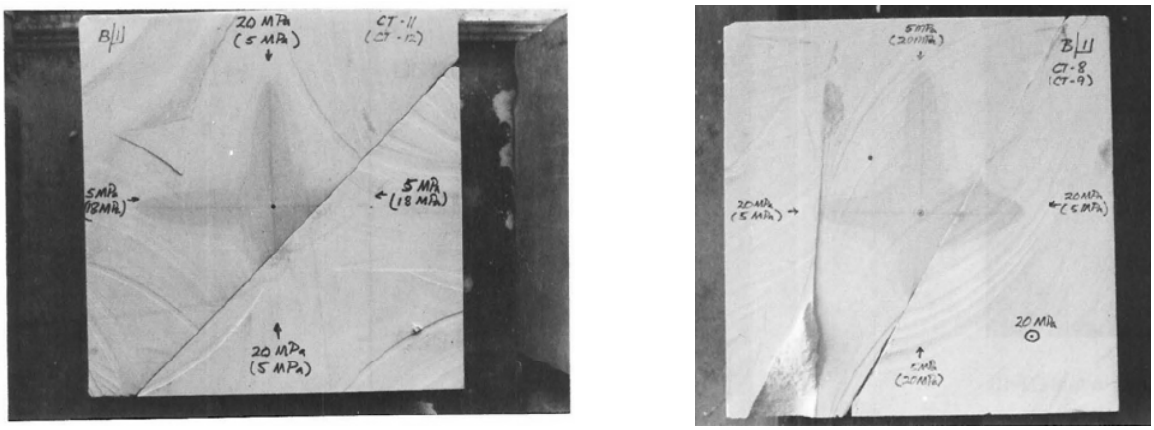

(a) (b)

Figure 2-5: Hydraulic fracture getting arrested in both the tests (2.5 a); Hydraulic fracture being arrested & crossing the pre-fracture in the two tests (2.5 b). (from Blanton, 1982)

Warpinski and Teufel (1987) conducted mineback experiments to study the effects of geologic discontinuities on hydraulic fracture propagation. They studied the effects of joints, faults, and bedding planes on both the fracture containment in vertical direction as well as fracture length and propagation. They concluded that crossing occurs at very high differential stress (~ 1500 psi), which was in good agreement with Blanton's experimental results. They observed that fractures were offset and that multiple stranding was more predominant than previously thought. They too derived a fracture interaction criterion to predict whether the hydraulic fracture causes a shear slippage on the natural fracture plane leading to its arrest, or dilates the natural fracture causing excessive leak-off. For arrest of the induced fracture, criterion is:

$$(\sigma_1 - \sigma_3) > \frac{2\tau_0 - 2p_\sigma K_f}{\sin 2\theta + K_f \cos 2\theta - K_f} \qquad (2.11)$$

and for natural fracture dilation as:

$$p_{\sigma} > \frac{(\sigma_1 - \sigma_3)(1 - \cos 2\theta)}{2} \tag{2.12}$$

where p_σ is the treatment overpressure, τ_0 is the inherent shear strength of the natural fracture plane.

Another simple and analytical fracture interaction was later provided by Renshaw and Pollard (1995). They derived their criterion by applying a first-order analysis of the stresses near a mode I fracture impinging on a frictional interface (i.e. natural fractures). Their criterion, though validated by experimental results later, was limited to orthogonal intersections between the approaching hydraulic fracture and the interface. Moreover, they assumed that crossing occurs via reinitiation of the fracture on the other side of the interface rather than by continuous propagation of the fracture through the interface. Their criterion could be stated as follows:

compressional crossing will occur if the magnitude of the compression acting perpendicular to the frictional interface is sufficient to prevent slip along the interface at the moment when the stress ahead of the fracture tip is sufficient to initiate a fracture on the opposite side of the interface

Since the material on the either side of the interface was assumed to be brittle, elastic, homogeneous, and isotropic, they used the principles of Linear Elastic Fracture Mechanics (LEFM) to derive a simple mathematical formula for their criterion (limited to orthogonal intersections) as follows:

$$\frac{-\sigma_3}{T_0 - \sigma_1} > \frac{0.35 + \frac{0.35}{K_f}}{1.06} \tag{2.13}$$

where T_0 is the tensile strength of the rock in psi.

Some other experiments were carried out in the past by Blair et al. (1989), who used fine tungsten wires embedded in gypsum to track the fracture propagation path, and Beugelsdijk et al. (2000), who studied the effect of shrinkage cracks in Portland cement blocks on fracture propagation path. The latter observed that at higher treatment pressures, the hydraulic fracture was more likely to divert along the pre-existing cracks. He also found out that high flow rate or viscosity of the fracturing fluid results in fluid-driven fractures, and crossing is more likely. On the other hand, low flow rate just opens up the pre-existing cracks.

Some of the researchers have conducted field studies in order to better understand the impact of natural fractures on hydraulic fractures, stimulation design, production decline, etc. These field studies (Rodgerson (2000), Britt and Hager (1994), Vinod et al. (1997), Azeemuddin et al. (2002), Murphy and Fehler (1986)) have indicated the following effects of natural fractures on hydraulic fracturing:

- High net pressures
- Premature screen-out
- Enhanced leak-off
- Arrest of the fracture propagation
- Formation of multiple fractures
- Fracture offsets

Some other experimental studies were conducted to determine the far-field geometry of the hydraulic fractures in these naturally fractured formations. Doe and Boyce (1989) conducted experiments to observe the fracture geometry in salt under hydrostatic and non-hydrostatic stress. They concluded that for stress ratios below 1.5-1.0, hydraulic fracture will have more branching and higher fracture multiplicity with decreasing stress orientation. These results highlight the significance of deviatoric stresses on fracture geometry. They also suggested that the more reliable method of observing fracture geometry is mineback experiments, where a hydraulic fracture is made with a dyed fluid and the fracture is mined out for mapping. These mineback experiments were later carried out by Jeffrey et al. (1992), who observed irregular, multiple fracture geometries consisting of both horizontal and vertical cracks. Similarly, Wawersik and Stone (1989) conducted their own mineback study and concluded that the fracture patterns can be divided into four different types of categories.

In the recent past, a very comprehensive experimental study was conducted by Zhou et al. (2008) to clarify the mechanism of hydraulic fractures interaction with pre-existing fractures. He conducted true tri-axial tests in the laboratory to observe the effect of strength parameters, deviatoric stress ratio, and angle of approach on the fracture geometry for different stress regimes (tectonic and normal stress regime). He simulated the natural fractures by casting three different types of paper (rice paper, wrapping paper, and ordinary paper) into the cement blocks. These papers have different thicknesses and friction properties, and thus served as the natural fractures with varying aperture and strength. Figure 2-6 and Fig. 2-7 show the test blocks after a series of experiments.

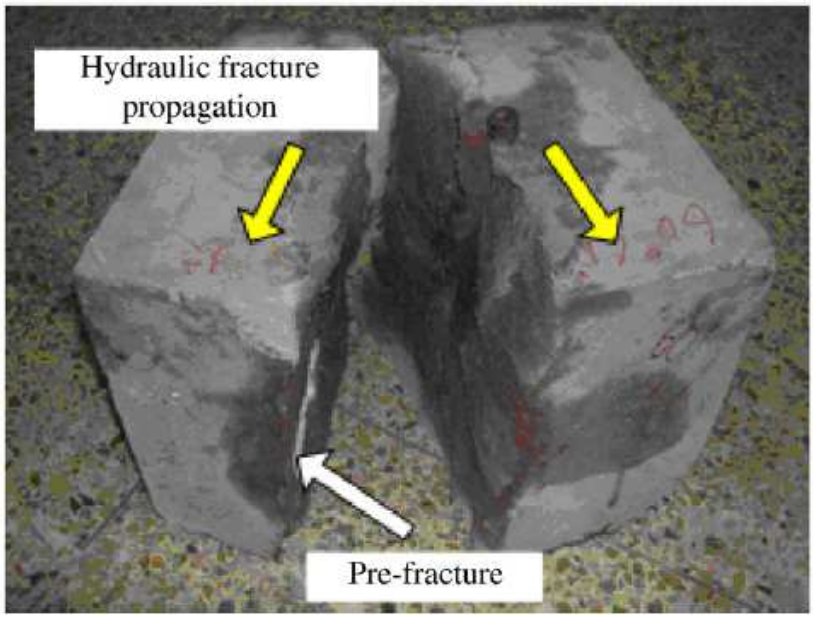

Figure 2-6: Test block specimen after a series of experiments. Here, the hydraulic fracture crossed the pre-existing fracture and propagation direction was not changed ($\theta=60^{o}$, $\Delta\sigma=7$ MPa and normal stress regime) (from Zhou, 2008)

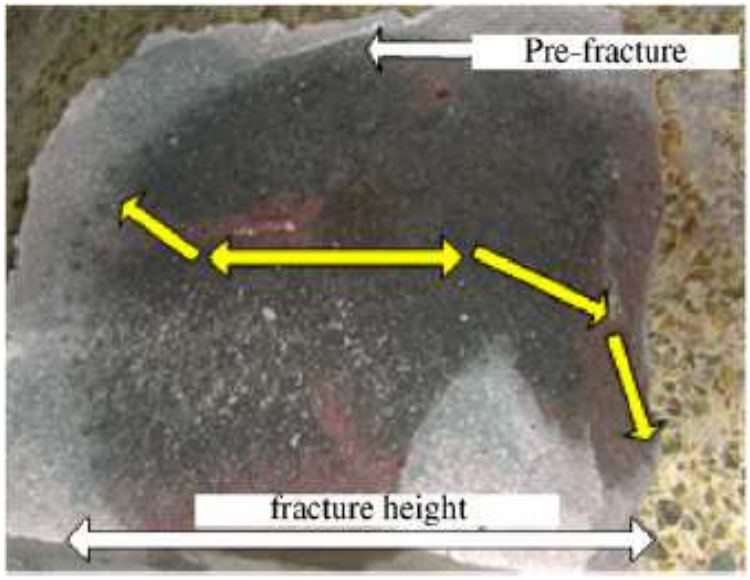

Figure 2-7: Test block specimen after the experiments. Here, horizontal direction is the fracture height direction; yellow arrow shows the propagation direction of the fracture. (from Zhou, 2008)

He concluded that apart from the deviatoric stress and the angle of approach, strength of pre-fractures also plays a key role in affecting fracture geometry. He observed that the pre-fractures with the least shear strength caused the least arrested area of the hydraulic fracture and with the increase in shear strength of the pre-fractures, arrest area also increases. He also observed that crossing is a dominant behavior for pre-fractures with very small aperture whereas dilation tendency increases if the pre-fracture has a larger aperture. Different stress regimes also play a key role in determining fracture geometry.

Modeling Studies

Apart from the experimental studies mentioned in the section above, there has been a tremendous focus on the modeling aspect of the fracturing in naturally fractured formations in the recent past. Some researchers have developed predictive tools/models for fracture behavior in these formations. However, the very first step in building these models, which is inputting the characteristics and locations of the natural fractures and/or weak planes, is a major hurdle as it is very difficult to characterize these natural fractures in the formation. There have been attempts at advancement of technology to capture these natural fractures in the seismic, yet it remains pretty unreliable.

In the literature, the usual practice has been to generate these natural fractures by using some sort of random generator (e.g. Zhang and Sanderson (2002)). However, in reality, they might be a result of tectonic movements, and not purely a random phenomenon. Therefore, Olson (1993) studied the development of these joint patterns in rocks from a continuum and fracture mechanics perspective. He tried to reproduce the joints spacing, lengths, and apertures taking several mechanical parameters into account

and used the subcritical growth law in his two dimensional numerical model. He concluded that fracture patterns are highly dependent on the subcritical growth index (n). He showed that for high values of n, fractures grow in clusters, with many short fractures in between a few longer ones, whereas for intermediate to low values of n, the fracture spacing is quite regular and the lengths of the fractures is large too. This was an important step towards modeling the interaction between hydraulic fractures and natural fractures.

After the fracture pattern is input into any fracturing model, the next step is to model the interaction between the hydraulic fracture and natural fractures. Lam and Cleary (1984) modeled the effects of bedding planes or frictional interfaces on the hydraulic fracture growth. They assumed a plane strain condition for their model and used the displacement discontinuity method to solve the problem. In their model, slippage, not the opening, along the natural fracture played an important role, and the fluid pressure inside the fracture was assumed to be constant. Jeffrey et al. (1987) also used the displacement discontinuity method to develop a two-dimensional model for interaction between the fractures. They were able to model the slippage along the natural fractures (using Mohr-Coulomb Failure Criterion) and concluded that these fracture interactions might result in higher treatment pressures. Similar study was done by Akulich and Zvyagin (2008), De Pater and Beugelsdijk (2005), and, Zhao and Young (2009) using the distinct element method to model the effects of the natural fractures on the hydraulic fracture behavior. Though Akulich and Zvyagin's model did not incorporate fracture intersections, it did give an idea about the slippage along the fault and the resulting effects on the stress intensity factors at the tip of the hydraulic fracture. Rahman et al. (2009) used the finite element method to simulate the same problem, and observed the effects of poroelasticity in these reservoirs. Olson (2008) developed a

numerical code based on a pseudo-3d displacement discontinuity solution to model the propagation of multiple fractures. He demonstrated the effects of several in-situ and operational parameters on the stress shadowing and thereby the resultant fracture network geometry from horizontal wells and in naturally fractured formations. His model, however, did not take into account the fluid flow inside the fracture, and used a constant pressure condition.

In the recent years, attempts have been made to use advanced mathematical and numerical techniques to simulate this problem. Lecampion (2009) used the Extended Finite Element Method (XFEM) to solve the elasticity equation. The advantage of using XFEM is that the fracture is allowed to propagate independently of the mesh configuration by permitting it to cross the elements. However, he did not incorporate the fracture propagation and the coupling process, thus neglecting the main advantage of XFEM. Dahi-Taleghani (2009) and, Dahi-Taleghani and Olson (2011) used XFEM in their two-dimensional model and addressed these issues. They used critical energy release rate ratio as the criterion for interaction between the hydraulic fracture and the natural fractures. Weng et al. (2011) developed a pseudo-3d unconventional fracturing model (UFM) to simulate complex fracture network propagation in naturally fractured formation. They model took into account the fracture interaction, multiple fractures propagating from the wellbore, stress shadowing effects, proppant transport, etc. They demonstrated the effects of rock fabric, reservoir parameters on the resulting fracture network geometry.

Chapter 3: Model Formulation

This chapter presents the numerical model used to predict the hydraulic fracture propagation path once it intersects the natural fracture, and, to predict and quantify the extent of the microseismic activity cloud when a hydraulic fracture is created in a formation having natural fractures/weak planes. First, a detailed description of the software used for this project (FLAC3D) is provided to show the algorithm flowchart, computation cycles, and principles of the software. Then the governing equations for different constitutive models and their theories are presented for better understanding the physics embedded in the software. The subsequent section deals with the steps in creating the geomechanical model in FLAC3D, including grid geometry, assumptions, boundary conditions, challenges, and post processing. The last section presents some initial results, and compares them with the literature to validate the formulated geomechanical model.

INTRODUCTION TO FLAC3D

Fast Lagrangian Analysis of Continua in 3 Dimensions (or, FLAC3D) is an explicit finite difference program to study, numerically, the mechanical behavior of a continuous three-dimensional medium as it reaches equilibrium or steady plastic flow. The mechanics of the medium are derived from general principles (definition of strain and laws of motion), and the use of constitutive equations defining the idealized material. It is particularly useful in solving elastoplastic material behavior or large strain problems as the grid can deform. The explicit, Lagrangian calculation scheme and the mixed-discretization zoning technique embedded in FLAC3D ensure that the plastic collapse and flow are modeled very accurately. The software has twelve different constitutive models to simulate different materials and conditions, including elastic, elastoplastic,

strain hardening and strain-softening. In addition to that, FLAC3D has the capability to model single phase fluid flow (darcy flow only) through porous media along with performing coupled flow/deformation analysis. However, fluid flow is not modeled explicitly in this thesis and poroelastic effects are neglected in this study.

In order to set up a model to run a simulation with FLAC3D, three fundamental components of a problem must be specified: a) a finite difference grid; b) constitutive model (or behavior) and material properties; and c) initial and boundary conditions.

Grid and Boundaries

A gridblock (or, zone) is the smallest geometric domain within which the change in any phenomenon (e.g., stress versus strain) is evaluated. It is generated by built-in meshing feature in FLAC3D. By default, discretization of the material body is done into hexahedral zones. The vertices of a gridblock are called the gridpoints. Some of the variables used in FLAC are stored in the gridblocks (e.g., density, pore pressure, etc.), while some are stored in the gridpoints (e.g., displacement, velocity, etc.).

Boundary conditions can vary from the mechanical boundary conditions, like fixed stress or displacement, to fluid boundary conditions, like constant pore pressure, specific discharge, and leaky conditions. For implementation in the code, all stresses and nodal velocities are initially set to zero; then, initial stresses are specified as initial conditions.

Main Calculation Steps

As mentioned earlier, FLAC3D uses an explicit “time-marching” finite difference solution scheme (Figure 3-1). For every timestep, new strain rates are derived from the

nodal velocities. Then constitutive equations (described in the next section) are used to calculate the new stresses from the strain rates and stresses at the previous time. Equations of motion are then invoked to derive new nodal velocities and displacements from the stresses and forces. This sequence is repeated at every timestep until the maximum out-of-balance force is within the tolerance limit specified by the user.

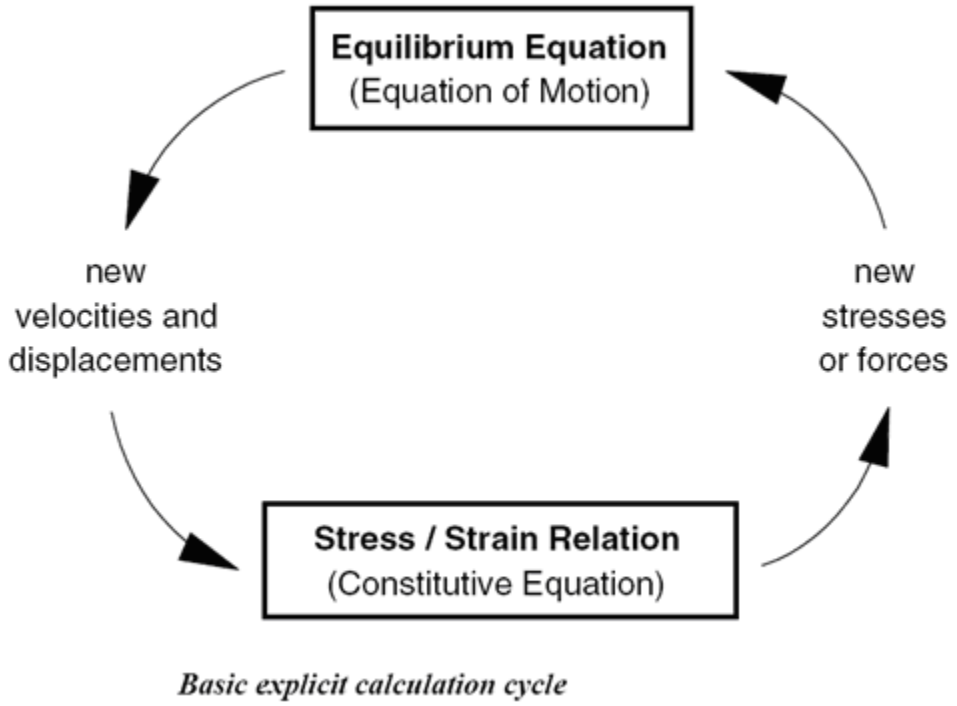

Figure 3-1: Calculation cycle in FLAC3D (from User Manual, FLAC3D 3.1)

CONSTITUTIVE EQUATIONS

In this project, the two constitutive models, elastic and elastoplastic, have been used for different simulations. Thus, the governing equations behind both the models are presented briefly in this section for better understanding of the physics.

Elastic Model

Here, the mechanical behavior of a continuous three-dimensional material is described mathematically by the equations of equilibrium (Eq. 3.1), the definition of strain (Eq. 3.2) and the constitutive equations (Eq. 3.3).

$$\sigma_{ij,j} + \rho g_i = \rho \frac{\partial^2 u_i}{\partial t^2} \tag{3.1}$$

$$\varepsilon_{ij} = \frac{1}{2}\left(u_{i,j} + u_{j,i}\right) \tag{3.2}$$

Since the medium is assumed to be homogeneous, isotropic, and perfectly elastic, strain increments can be related to the stress increments according to the linear and reversible law of Hooke (constitutive equation) as follows:

$$\Delta\sigma_{ij} = 2G\Delta\varepsilon_{ij} + \alpha\Delta\varepsilon_{kk}\delta_{ij} \tag{3.3}$$

where the Einstein summation convention applies, δ_{ij} is the Kroenecker delta symbol, and α is a material constant related to the bulk modulus, K, and shear modulus, G, as

$$\alpha = K - \frac{2}{3}G \tag{3.4}$$

This system of 15 equations for 15 unknowns (6 components of stress tensor σ_{ij} and strain tensor ε_{ij}, plus the 3 components of the displacement vector u_i) is solved at each node using an explicit, finite difference numerical scheme. New stresses are then obtained from the relation:

$$\sigma_{ij}^{N} = \sigma_{ij} + \Delta\sigma_{ij} \tag{3.5}$$

The deformation in the elastic medium is independent of the stress path since the constitutive equation is linear in nature.

Plastic Model

All plastic models potentially involve some degree of permanent (i.e. irreversible), path-dependent deformations (failure) which is a consequence of the nonlinearity of the stress-strain relations. In plasticity literature, a so-called yield function (often denoted by the symbol f) and a flow rule (with plastic potential function, often denoted by the symbol g) are commonly employed to distinguish plastic from elastic states. The yield function basically defines the stress combinations for which plastic flow takes place in the medium. The flow rule specifies the direction of the plastic strain increment vector as that normal to the potential surface; it is called associated if the potential and yield functions coincide, and non-associated otherwise (Vermeer and deBorst (1984)).

The plastic theory, in FLAC3D, and in general, states that the total strain increment can be decomposed into an elastic contribution, ε^e, and a plastic contribution, ε^p, with only the elastic part contributing to the stress increment by means of an elastic law discussed in previous section (i.e. Hooke's Law).

$$\Delta\underline{\varepsilon}_i = \Delta\underline{\varepsilon}_i^e + \Delta\underline{\varepsilon}_i^p \tag{3.6}$$

$$\Delta\underline{\sigma}_i = S_i(\Delta\underline{\varepsilon}_1^e, \Delta\underline{\varepsilon}_2^e, ..., \Delta\underline{\varepsilon}_n^e), \qquad \text{i=1,n} \tag{3.7}$$

where S_i is a linear function of the elastic strain increments.

Now, to model elastoplastic behavior in materials, FLAC offers several constitutive models like Drucker Prager Model, Mohr-Coulomb Model, Hoek-Brown Model, etc. In this thesis, Mohr-Coulomb model has been used to model the elastoplastic behavior in the materials. The Mohr-Coulomb model uses the Mohr-Coulomb criterion as a shear yield function, with a tension cutoff (tension yield function). The yield function

for Mohr-Coulomb criterion is described by means of two functions, f^s and f^t, used to define shear failure and tensile failure, respectively.

$$f^s = \sigma_1 - \sigma_3 N_\phi - 2c\sqrt{N_\phi} \tag{3.8}$$

where σ_1 and σ_3 are the maximum and minimum principal effective) stresses respectively (compressive stresses are positive), ϕ is the friction angle, c is the cohesion, and

$$N_\phi = \frac{1+\sin(\phi)}{1-\sin(\phi)} \tag{3.9}$$

The tensile failure criterion can be written as:

$$f^t = \sigma_3 - \sigma^t \tag{3.10}$$

where σ^t is the tensile strength of the material.

The function f is negative as long as the stress circle makes no contact with the Mohr-Coulomb envelope, while it vanishes when they touch. The material cannot sustain a stress circle that intersects the envelope (this would imply f>0) (see Figure 3-2). Hence, a material is said to be in an elastic state if f<0, and in a plastic state when f=0. An element may pass from an elastic state to a plastic state and vice-versa. For plastic yielding, the element needs to be in a plastic state (f=0), and to remain in a plastic state (df/dt=0). The yield function surface in 3-D principal stress state is shown in Figure 3-3 below.

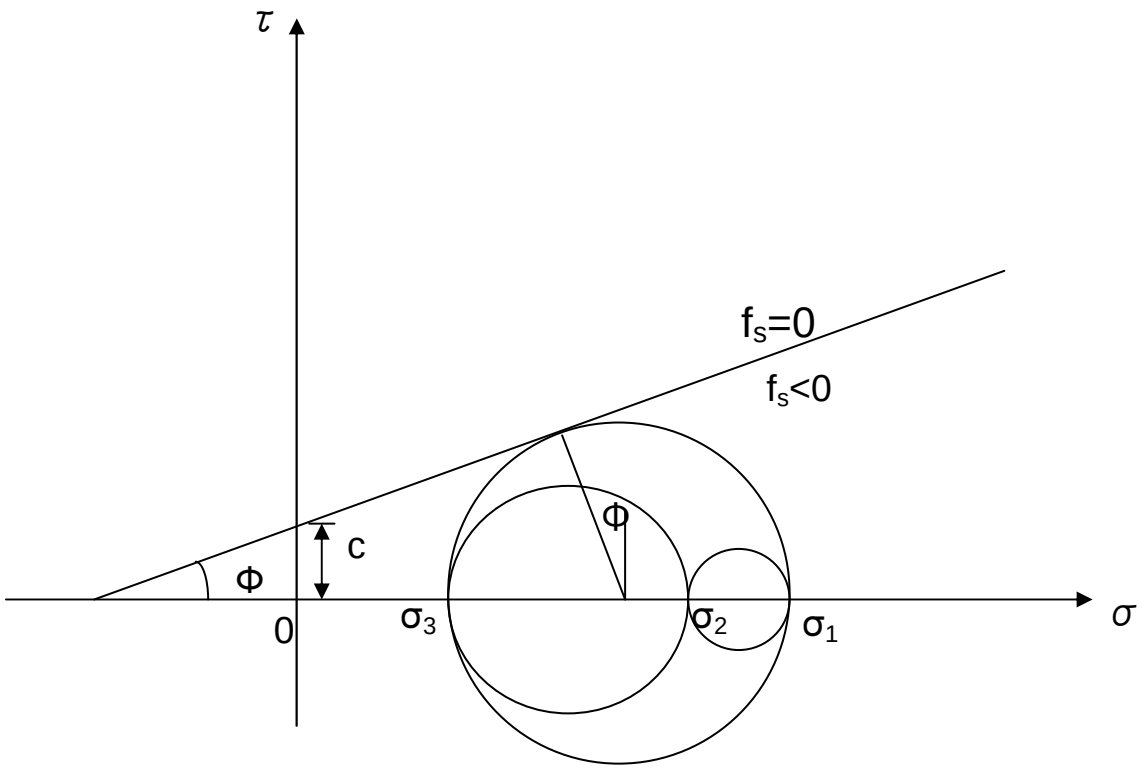

Figure 3-2: Mohr-Coulomb criterion representing stress circle at yield (touching the envelope) (plane representation)

Now, in contrast with the elastic theory, there is no direct correspondence between the total stress and total (plastic) strains. Instead, the plastic strains are assumed to be derived from a scalar function g, called the plastic potential function, of the stresses as follows:

$$\Delta \underline{\varepsilon}_i^p = \lambda \frac{\partial g}{\partial \underline{\sigma}_i} \tag{3.11}$$

where λ is constant. λ is a non-negative multiplier if plastic loading occurs (f=0 and df/dt=0), whereas, it vanishes in the elastic state. It has no physical meaning. The plastic

potential function can again be described by means of two functions, g^s and g^t, used to define shear plastic flow and tensile plastic flow, respectively.

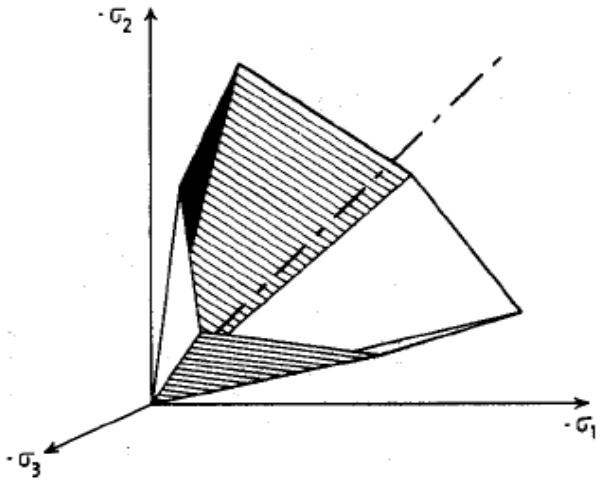

Figure 3-3: Mohr-Coulomb yield surface in principal stress space (from Vemeer & deBorst,1984)

$$g^s = \sigma_1 - \sigma_3 N_\psi \tag{3.12}$$

where ψ is the dilation angle and

$$N_\psi = \frac{1+\sin(\psi)}{1-\sin(\psi)} \tag{3.13}$$

Dilation angle, ψ, basically represents the ratio of plastic volume change over plastic shear strain. Generally, for concrete and rocks, the dilation angle is significantly smaller than the friction angle. The function g^t can be written simply as:

$$g^t = -\sigma_3 \tag{3.14}$$

As mentioned earlier, the flow rule is said to be associated if g≡f, and non-associated otherwise. Thus, it can be seen that the function g^s corresponds to a non-associated law whereas the function g^t corresponds to an associated flow rule.

Substituting Eq. 3.6 in Eq. 3.7, and making use of linear property of the function S_i, we can write:

$$\Delta\underline{\sigma}_i = S_i(\Delta\underline{\varepsilon}_1, \Delta\underline{\varepsilon}_2, ..., \Delta\underline{\varepsilon}_n) - S_i(\Delta\underline{\varepsilon}_1^p, \Delta\underline{\varepsilon}_2^p, ..., \Delta\underline{\varepsilon}_n^p) \tag{3.15}$$

Now, Eq. 3.11 can further be substituted into Eq. 3.12 and again making use of the linearity of S_i, it can be written:

$$\Delta\underline{\sigma}_i = S_i(\Delta\underline{\varepsilon}_1, \Delta\underline{\varepsilon}_2, ..., \Delta\underline{\varepsilon}_n) - \lambda S_i\left(\frac{\partial g}{\partial\underline{\sigma}_1}, \frac{\partial g}{\partial\underline{\sigma}_2}, ..., \frac{\partial g}{\partial\underline{\sigma}_n}\right) \tag{3.16}$$

FLAC3D IMPLEMENTATION

In FLAC3D, an elastic guess $\underline{\sigma}_i^I$, i=1,n, for the stress state at time t+Δt is first evaluated by adding the stress increments, calculated from the total-strain increments for the step, to the stress components at time t, as follows:

$$\underline{\sigma}_i^I = \underline{\sigma}_i + S_i(\Delta\underline{\varepsilon}_1, \Delta\underline{\varepsilon}_2, ..., \Delta\underline{\varepsilon}_n) \tag{3.17}$$

If the elastic guess violates the yield function (either Eq. 3.8 or Eq. 3.10), either shear failure or tensile failure is declared (depending on which yield function is violated), and Eq. 3.18 is used to place the new stress exactly on the yield curve. Otherwise, the elastic guess gives the new stress state at time t+Δt, and no plastic flow takes place in the material.

$$\underline{\sigma}_i^N = \underline{\sigma}_i^I - \lambda S_i\left(\frac{\partial g}{\partial\underline{\sigma}_1}, \frac{\partial g}{\partial\underline{\sigma}_2}, ..., \frac{\partial g}{\partial\underline{\sigma}_n}\right) \tag{3.18}$$

where $\underline{\sigma}_i^N$ is termed as *new* stress components, and is defined as:

$$\underline{\sigma}_i^N = \underline{\sigma}_i + \Delta\underline{\sigma}_i \tag{3.19}$$

MODEL DESCRIPTION AND SIMULATION PROCEDURE

The model developed was implemented using the commercial code FLAC3D which is an explicit finite difference simulator that handles mechanical deformation in continuum. The inbuilt programming language, FISH, was used to write the required routines to track the fracture width, interaction criterion, and the failure region around the fracture tip. The simulation procedure can be described by the flowchart below (Figure 3-4).

Grid Generation and Boundary Conditions

In simulating the cases for interaction between the hydraulic fracture and an existing natural fracture, only a quarter of the physical domain was modeled (due to symmetry) with the wellbore at the corner of the grid, i.e. at the origin (0,0). The region near the fracture tip was meshed heavily to capture the near tip phenomena as accurately as possible. However, the grid becomes coarser progressively as we move away from the tip in the either direction. This is partially because of the limitation on the number of gridblocks in the software, and partially to save the computation time for a single simulation.

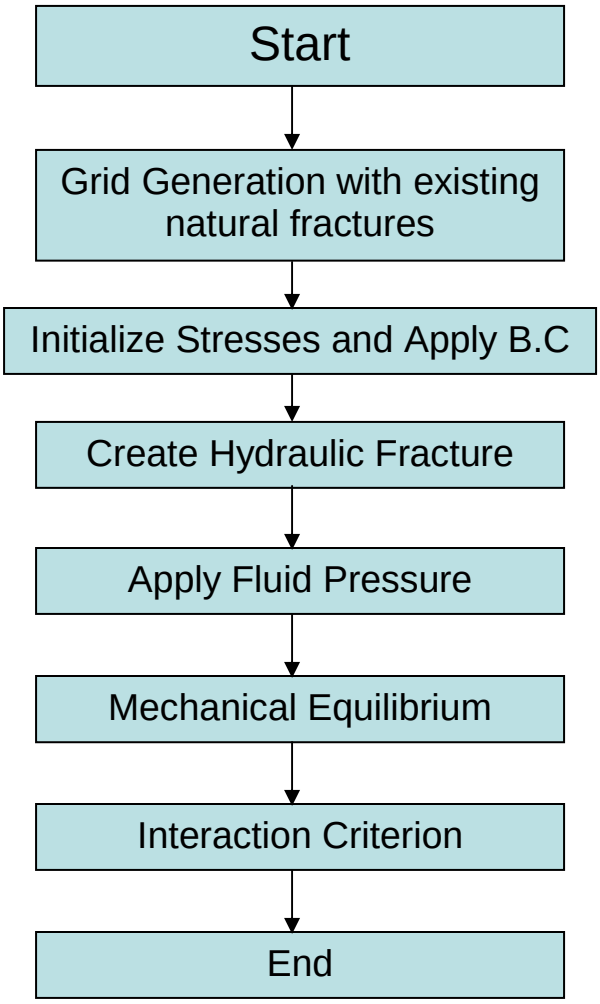

Figure 3-4: Simulation Flow Chart

Initially, a 2D plane strain model (i.e. KGD fracture geometry) was used to validate the model by simulating only a single layer of pay zone and no adjacent layers. After the model was validated, the geomechanical model was made 3D (i.e. PKN fracture geometry) by adding an overburden layer on top, and an underburden layer below the pay zone.

The natural fractures were simulated by using “interface elements” (inbuilt feature in FLAC3D). These elements basically represent planes on which sliding and/or

separation can occur. They are characterized by properties of cohesion, friction, dilation, normal and shear stiffnesses, and, tensile and shear bond strength. However, when modeling the failure envelope near the hydraulic fracture, a different approach was followed to simulate these natural fractures. In that case, very thin zones (or the gridblocks) in the grid were specified “weak properties” (low cohesion, tensile strength, stiffness, etc). The selection of those thin zones (or, weak planes) was purely random in nature. This was done so because using more than a few interface elements in FLAC3D makes grid generation very awkward and also increases computation time drastically.

After the grid is generated, the model is subjected to the stresses in the normal faulting regime with the in-situ vertical stress being the highest, followed by the major and minor horizontal stresses. The boundary conditions correspond to zero normal displacement at the bottom and the vertical walls of the grid and a constant vertical stress at the top of the grid, corresponding to the in-situ vertical stress. Though poroelastic studies were not carried out in this model, pore pressure was also specified in the initializing conditions. This was done to just use the effective stresses while calculating failure envelope or propagation criterion. The schematic of the generated grid along with the stress state and the boundary conditions can be seen in the Figure 3-5 below.

Creating Hydraulic Fracture

As mentioned in the previous section, only a quarter of the physical domain was modeled in this project. Thus, only one wing of the fracture and half width was modeled. Hydraulic fracture of a known length was created by relaxing the zero normal displacement boundary condition on those gridpoints and applying a normal stress (i.e. the fluid pressure), higher than the value of S_{hmin}, on the faces, thus allowing them to deform under the application of the fluid pressure on the faces of those gridblocks. It is

worth mentioning here again that the model is static in nature, i.e. the hydraulic fracture length is fixed, and not changing with time. Thus the fluid pressure inside the fracture is specified by the user, and is constant. However, in some cases, an analytical expression (Eq. 3.20) for fluid pressure along the fracture length was used to simulate more realistic cases.

$$P(x) = (P_{wf} - S_{h,\min}) * \left(1 - \frac{x}{L_f}\right)^{0.25} + S_{h,\min} \tag{3.20}$$

where P_{wf} is the fluid pressure at wellbore and L_f is the fracture half-length.

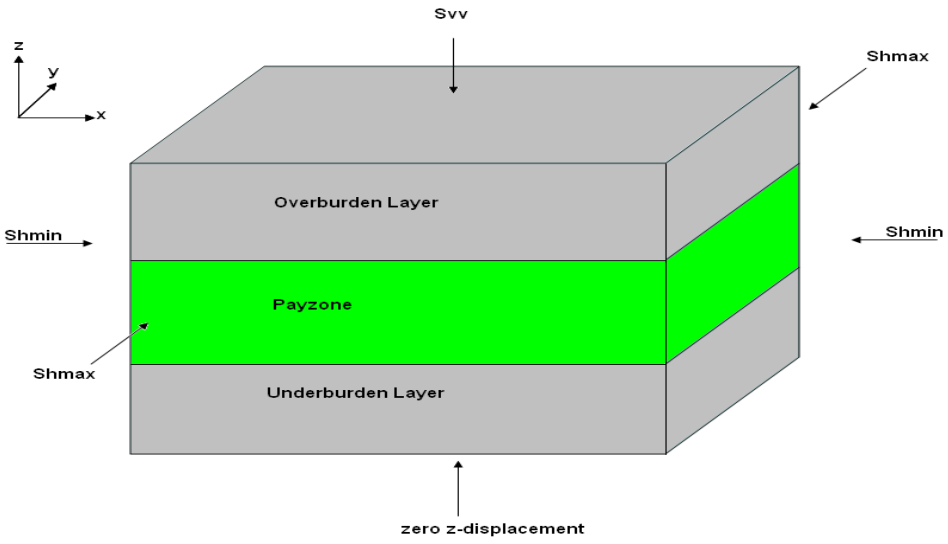

Figure 3-5: Schematic of the model grid with stress state and boundary conditions

Propagation of the hydraulic fracture by coupling the fluid flow inside the fracture with the deformation was tried in this project. However, due to large pressure and stress gradients near the tip, and pressure singularity at the tip, numerical convergence was very hard to achieve, and the scheme was unsuccessful. Figure 3-6 below shows the schematic

of the plane view of the grid along with the application of the fluid pressure and the boundary conditions. Note that the region around the fracture tip is meshed intensively.

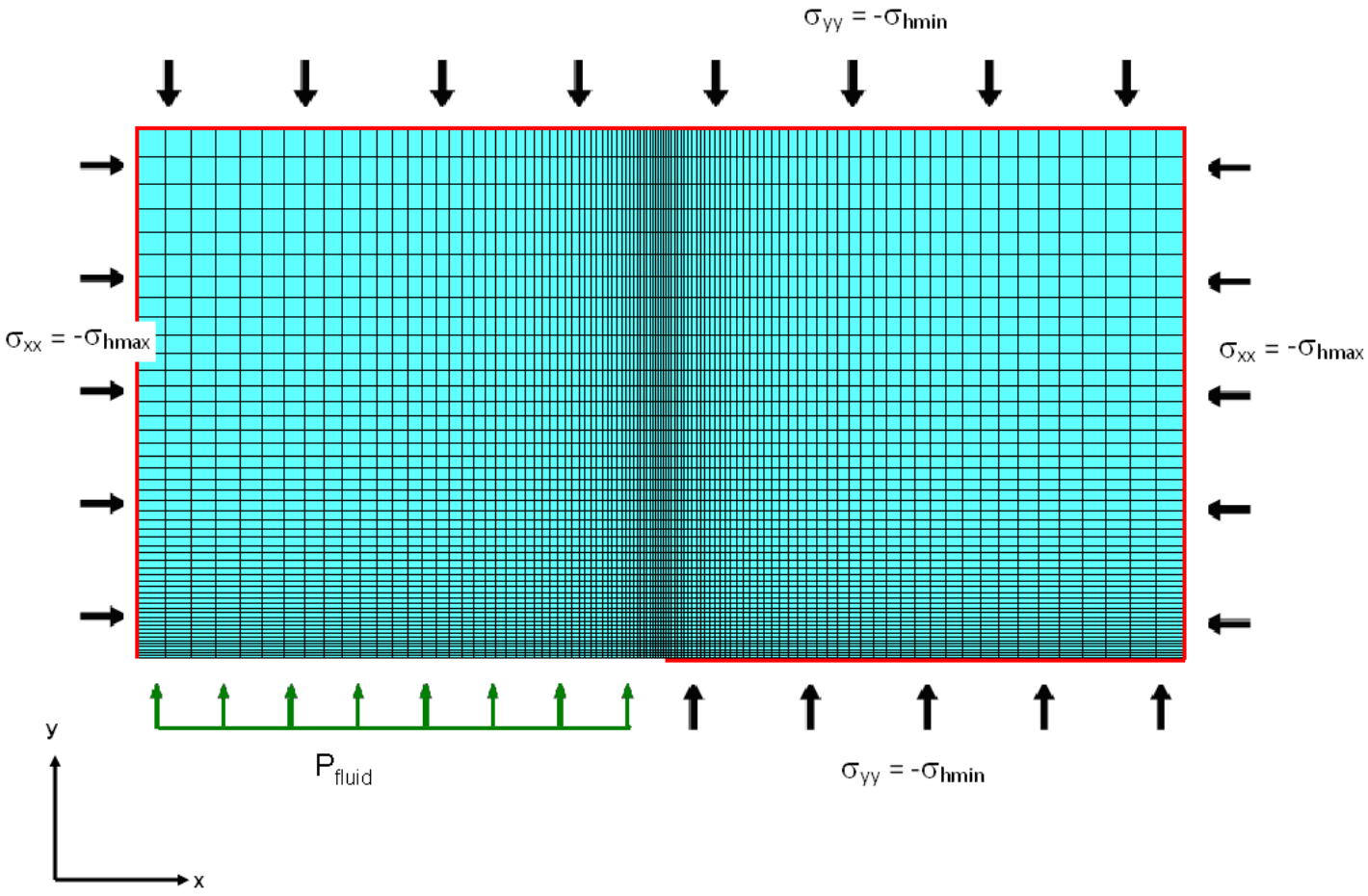

Figure 3-6: Plane view of the grid. Solid red line indicates the gridpoints with zero normal displacement boundary condition. Wellbore is at the origin (0, 0)

Mechanical Equilibrium and Interaction Criterion

After the grid is generated, stresses are initialized, boundary conditions are applied and the hydraulic fracture geometry is created, we *solve* the model, and allow it to reach the steady state (or, the mechanical equilibrium). FLAC's default mechanical timestep was chosen in the simulations. The condition to define mechanical equilibrium

is highly flexible, and can be defined by user. For all the simulations described in this work, system was said to have reached mechanical equilibrium when the ratio of unbalanced forces reached the tolerance limit of 1e-6.

After the system reaches mechanical equilibrium, we apply a simple, yet realistic, interaction criterion to predict the path of the hydraulic fracture. The grid was generated in such a way that the hydraulic fracture tip was just touching the interface (i.e. natural fracture). Thus, fluid pressure at the tip can be assumed to be zero since in reality there is usually a fluid lag, and thus interaction between the natural fracture and the hydraulic fracture can be analyzed purely from mechanical standpoint without considering fluid flow. Now, there are two possibilities at this moment. Hydraulic fracture can either cross the natural fracture, or get arrested by it. For a new fracture to initiate on the other side of the natural fracture, the maximum effective principal stress must reach the tensile strength of the rock. And for this fracture re-initiation to occur, the stresses acting on the interface (or, natural fracture) should be such that the interface must not slip, so that the tip stresses can be transmitted to the other side of the interface. If, however, interface slips, the stresses are relaxed, and are not transmitted across the interface, and the hydraulic fracture will be arrested at this moment. At later times, if the flow continues, the dilated natural fracture becomes a part of the hydraulic fracture network, i.e. the hydraulic fracture turns and propagates along the natural fracture (see Figure 3-7). However, in this study we are interested only in the first timestep, i.e. the moment when fracture tip intersects the natural fracture. This is because, to model the next timestep, the fluid flow has to be modeled and coupled with deformation problem thus making it a dynamic problem (just like the fracture propagation problem). As mentioned before, the scheme that was tried to model the fracture propagation was unsuccessful, thus limiting us to only the static solution.

It will be shown in the next chapter that the simulation results using this interaction criterion were compared with the experimental results available in the literature, and that the results were found to be a close match.

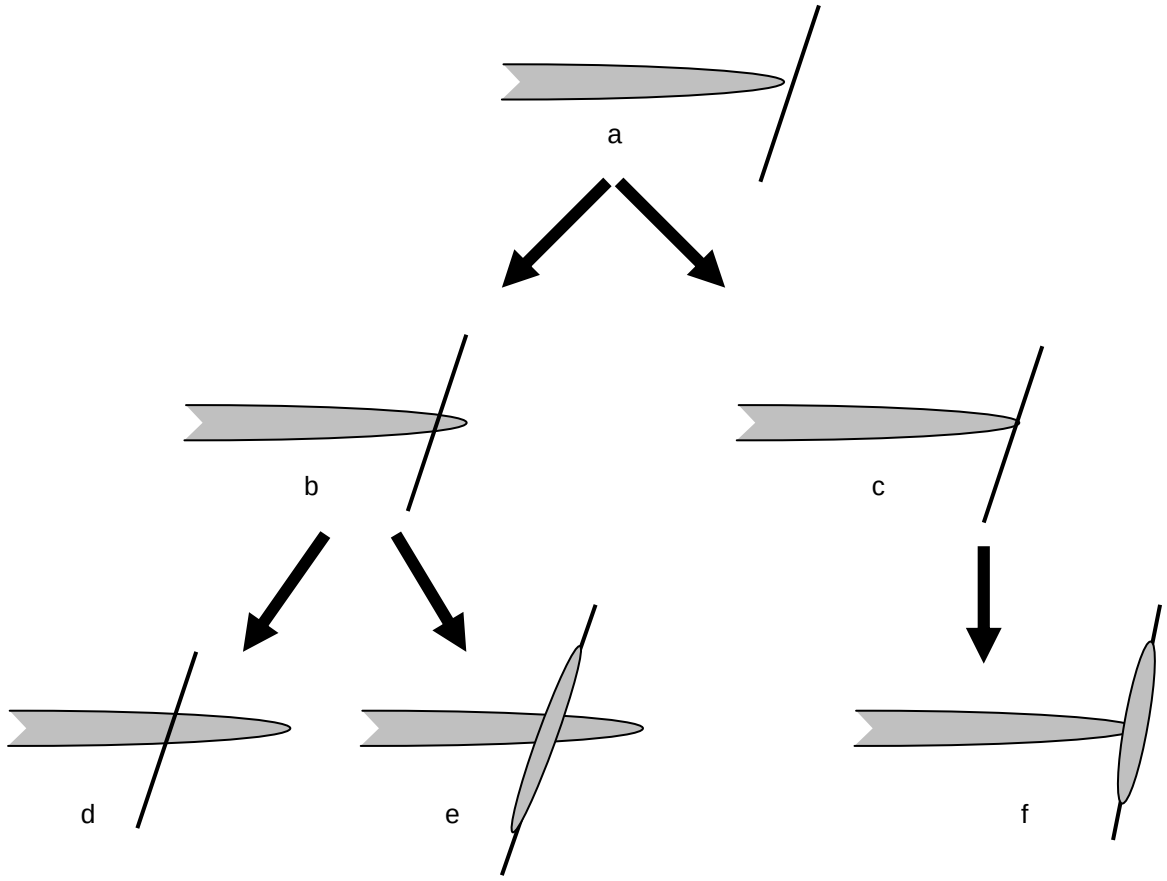

Figure 3-7: Schematic showing different possible scenarios for the hydraulic fracture and natural fracture interaction.

In addition to the model described above, another numerical model was developed to observe the impact of geomechanics on the microseismicity in the unconventional reservoirs. In simple words, microseisms are micro-shear slippages. Thus, these slippages are not tensile opening/fracturing, but some sort of shear movements associated with, a) hydraulic fracture itself, and, b) re-activation of planes of weakness already present in the

reservoir due to changes in stress. There are several mechanisms that can cause a microseismic activity. It is well known that a pressurized fracture disturbs the stress field around it, and results in a different stress state around itself. Now, if there are any weak planes present in this perturbation zone, microseisms could potentially be generated. However, most often, the hydraulic fracture creates a zone of compressive stress around it which is typically not favorable for inducing shear movements. Second factor is fluid leak-off, which increases pore pressure and thus can destabilize weak planes resulting in microseisms. However, since the unconventional formations have very low permeability, movement of the fluid far away in the formation is difficult to conceive. But, if the hydraulic fracture intersects the natural fracture and opens those fissures, it results in high permeability, and the fluid moves faster and goes farther away in the formation, potentially generating microseisms. One other factor is the stress changes around the hydraulic fracture tip. The region ahead of the crack tip usually generates very high shear stresses, and thus could potentially generate microseisms if the weak planes have favorable orientation and properties. The extent of this region is dependent on many factors including fracture size, net fluid pressure, in-situ stress state, etc. (Warpinski (2009)). In this thesis, focus has been on this factor only as the other factors (leak-off, etc.) require a propagating fracture to represent the phenomena accurately. Two different approaches were considered to model the microseismic activity cloud resulting from the fracture tip phenomenon as described below.

In the first approach, the weak planes were explicitly created in the matrix (or, grid) by specifying weaker properties to certain zones (or, gridblocks). The orientations and locations of these weak planes were chosen randomly. Then, a hydraulic fracture was created, as mentioned in previous sections, and after the simulation, a check was made to see if there was any shear failure occurring in those “weaker” zones. Then, in the next

simulation, the location of those weak planes was changed, and a check for failure was made. This process was repeated till there was no observed failure in those weak planes. In this manner, the potential microseismic cloud resulting due to fracture tip phenomenon was observed.

In the second approach, the weak planes were implicit in nature i.e. no weak planes were specified in the matrix. The hydraulic fracture was created and after the end of simulation, the f^s function, described in detail in the theory section above (Eq. 3-8), and repeated below for convenience, was evaluated for each gridblock, and its contour was plotted.

$$f^s = \sigma_1 - \sigma_3 N_\phi - 2c\sqrt{N_\phi} \tag{3.8}$$

where σ_1 and σ_3 are the maximum and minimum principal effective) stresses respectively (compressive stresses are positive), ϕ is the friction angle, c is the cohesion, and

$$N_\phi = \frac{1+\sin(\phi)}{1-\sin(\phi)} \tag{3.9}$$

Eq. 4.4 implies that $f^s>0$ indicates potential failure. Thus, looking at the contour plot of f^s, a potential microseismic cloud was observed. Please note that the weak planes within this cloud will fail only if they are favorably oriented, otherwise they will remain intact. Outside this cloud, weak planes will not fail, irrespective of the orientation and the properties.

This latter approach towards modeling the microseismic activity cloud offers advantages over the former approach. Firstly, the former approach is very time consuming and iterative as one has to keep changing the locations of weak planes in order to observe the boundary of the potential failure cloud. Considering that each simulation takes approximately two to three hours, the entire process can take a very long

time. Secondly, the latter approach allows us to include the non-vertical weak planes in the analysis as we don't have to model the weak planes explicitly. In the former approach, creation of multiple dipping and inclined (on x-y plane) weak planes is not easy, thus typically limiting us to only the inclined but vertical weak planes. There is, however, a potential disadvantage of choosing implicit approach over the explicit one. When there are many weak planes present in the matrix, one could argue that the failure of the weak plane closest to the hydraulic fracture might result in stress relaxation, and might affect the failure tendency of the weak plane farther away from it. To address this issue, a simulation was performed where weak planes were placed near the fracture and after the end of simulation, subsequent extent of f^s envelope was observed. It was seen that the overall extent of potential microseismic cloud is very similar to the case when f^s envelope was calculated without any weak planes present (shown in the next chapter). Thus, the second approach (i.e. the implicit approach) was adopted for all subsequent simulations and studies.

MODEL VALIDATION

In this section, a simplistic comparison between numerical results and the analytical results available in the literature for the fracture widths is presented. This enables us to have a confidence in the capabilities of the commercial code/software FLAC3D that has been used to perform the subsequent simulations. A more rigorous comparison of numerical results with experimental results is presented in the following chapter.

As mentioned in the chapter 2, Khristianovic and Zheltov (1955) presented a 2D fracture geometry assuming plane strain in the vertical direction. Geertsma and Klerk

(1969) improved this model by using an equation for plane strain (developed by England and Green (54)) and presented the following expression for fracture width:

$$w(x) = \frac{4(1-\upsilon^2)L_f(P_{fluid} - S_{h,\min})}{E}\sqrt{1-x^2} \tag{3.21}$$

where ν is the formation's poisson's ratio, E is the formation's Young Modulus, L_f is the fracture half-length, and x is the coordinate along fracture length

Similarly, for PKN type fracture geometry, Nordgren (1972) presented the following analytical formula for the case of no leak-off.

$$w(x) = \frac{2(1-\upsilon^2)h_f(P_{fluid} - S_{h,\min})}{E}\sqrt{1-x^2} \tag{3.22}$$

where h_f is the total fracture height.

Base case simulations were performed in the FLAC3D using the same procedure as described in the previous section. The material was assumed to be perfectly elastic, homogeneous, and isotropic. Table 3-1 lists the values of all the properties and stresses that were used for these base case simulations. Table 3-2 shows that the results obtained from the developed model and the analytical expressions match with each other. Figures 3-8 and 3-9 show the fracture geometries created by FLAC3D for these two cases. Using the parameters of Table 3-1, the simulations gave similar fracture widths at the wellbore (origin) to the 2D analytical models (Table 3-2), indicating that the model can be used for more complex cases as discussed in the next chapter.

Table 3-1: List of the parameters used for base case simulations

Parameters	**KGD Geometry**	**PKN Geometry**
Payzone length (m)	180	180
Payzone width (m)	80	80
Payzone height	60	60
Young's modulus (Payzone), psi	4.5e10	4.5e10
Poisson's ratio (Payzone), psi	0.2	0.2
Young's modulus (Bounding Layers), psi	-	3.5e10
Poisson's ratio (Bounding Layers)	-	0.2
Vertical stress, S_{vv} (psi)	7000	7000
Max. horizontal stress, $S_{H,max}$ (psi)	5500	5500
Min. horizontal stress, $S_{h,min}$ (psi)	4000	4000
Reservoir's pore pressure, P_p (psi)	3000	3000
Fracture half-length, L_f (m)	50	50
Fracture height, h_f (m)	-	60
Net fluid pressure, P_{net} (psi)	400	400

Table 3-2: Results obtained from the model and the analytical expressions

Max. fracture half-width (mm) for fracture type:	**Analytical result**	**Simulation result**
KGD	5.88	5.902
PKN	3.53	3.56

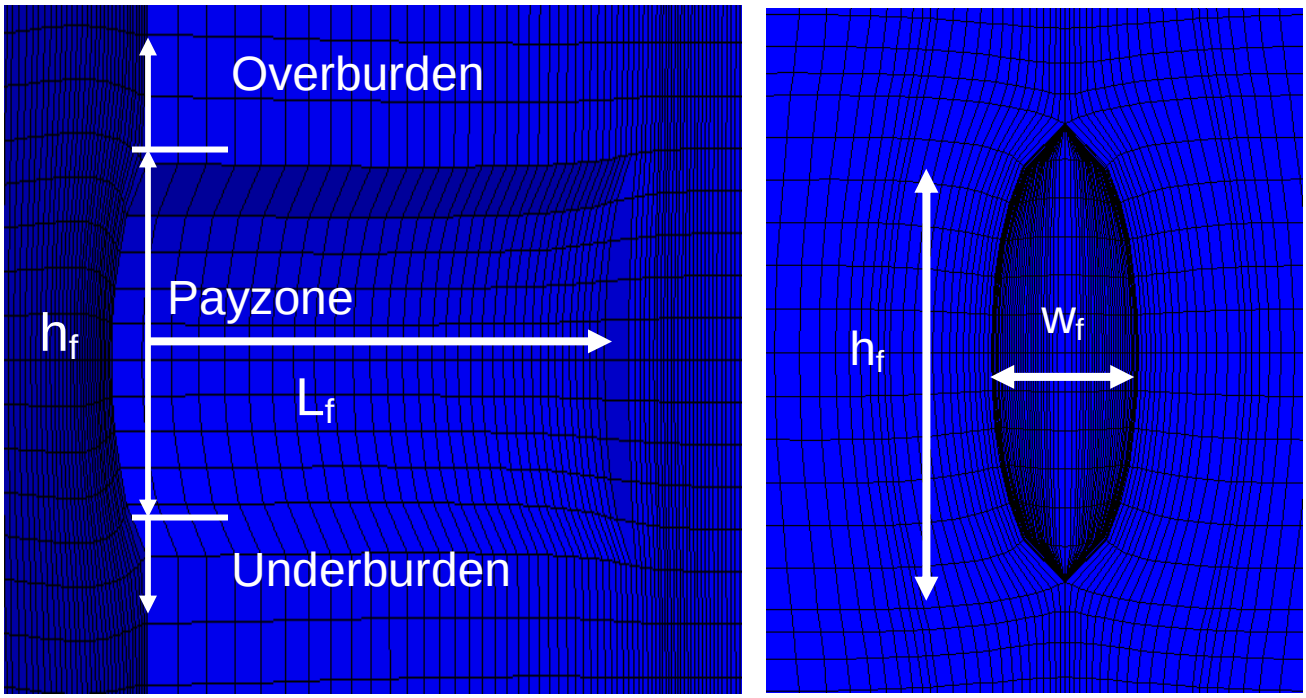

Figure 3-8: Elliptical (PKN type) fracture geometry resulting from the uniform pressure condition at the fracture face

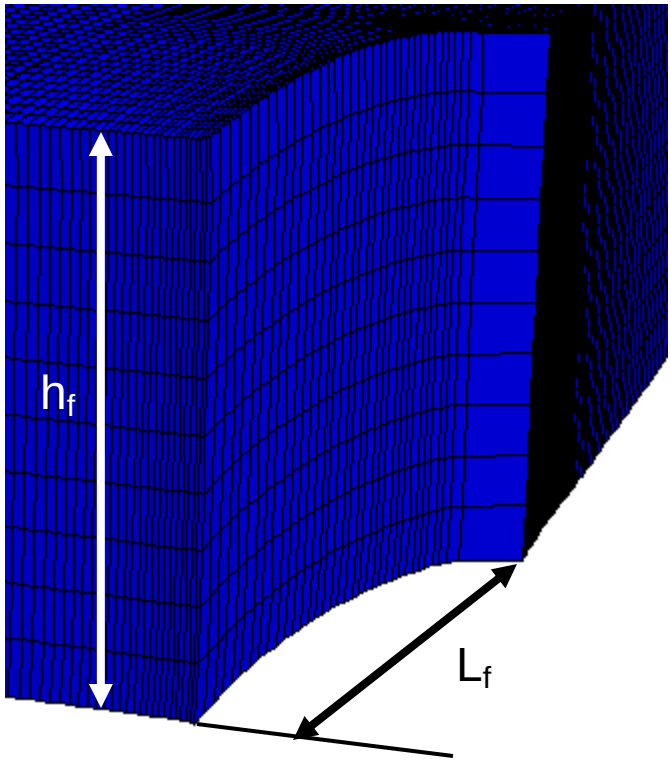

Figure 3-9: KGD type fracture geometry (characterized by the rectangular shape in vertical direction) in FLAC3D. Please note that there are no bounding layers above or below the payzone. Fluid pressure is uniform on the fracture face.

Chapter 4: Results and Discussion

This chapter presents the results of the numerical simulations that were carried out during this project. It is divided into two different sections. The first section deals with the hydraulic fracture path prediction in naturally fractured formations, and the second section presents the results for microseismic activity extent (or, cloud) from hydraulic fracturing in these naturally fractured formations. This chapter begins with a series of base case simulation results that help us to better understand the phenomena of hydraulic fracture interaction with natural fractures present in the formation. It then presents the results obtained for prediction of the hydraulic fracture propagation path after intersecting the natural fractures. A comparison of results obtained from the numerical simulations and experimental work in the literature has been made. This comparison again underlines the validity of the model developed.

In the second section, results for quantifying the extent of possible microseismic activity cloud have been presented. Two different approaches to build the models have been discussed and compared. Lastly, a comprehensive sensitivity analysis is presented for different parameters involved in the model.

HYDRAULIC FRACTURE PROPAGATION PATH PREDICTION

The work here is focused on the interaction of the hydraulic fracture with an existing natural fracture at the moment when hydraulic fracture tip is very close to, or just touches the natural fracture. As mentioned previously, this is because of the assumption of uniform fluid pressure (or, a pressure profile using analytical expressions). This limits us to study the fracture interaction from only the mechanics standpoint without considering fluid flow.

Any crack, when internally pressurized, exerts normal and shear stresses which are dominant around the crack tip. Analytical results have been given by Pollard and Segall (1987) for the stress field around a hydraulic fracture as:

$$\sigma_{xx} = \frac{P_{net}\sqrt{\pi x_f}}{\sqrt{2\pi r}}\cos\frac{\theta}{2}\left(1-\sin\frac{\theta}{2}\sin\frac{3\theta}{2}\right) \tag{4.1}$$

$$\sigma_{yy} = \frac{P_{net}\sqrt{\pi x_f}}{\sqrt{2\pi r}}\cos\frac{\theta}{2}\left(1+\sin\frac{\theta}{2}\sin\frac{3\theta}{2}\right)+P_{net} \tag{4.2}$$

$$\sigma_{xy} = \frac{P_{net}\sqrt{\pi x_f}}{\sqrt{2\pi r}}\sin\frac{\theta}{2}\cos\frac{\theta}{2}\cos\frac{3\theta}{2} \tag{4.3}$$

where r and θ are the polar coordinates at the crack tip. P_{net} is the net fluid pressure inside the crack.

The hydraulic fracture exerts normal and shear tractions on the natural fracture that is very close and ahead of the fracture tip. For the cases where natural fracture is orthogonal to the hydraulic fracture, a part of the natural fracture that is within the specific radius from the hydraulic fracture is under the tensile stress. Due to this tensile stress, a part of natural fracture may open even before hydraulic fracture intersects it. Figure 4-1 shows the width profile of the natural fracture as a result of tensile stress exerted by an approaching hydraulic fracture. Distance between the hydraulic fracture tip and the natural fracture was varied as shown in the plot. From the plots, one can conclude that it is most likely to get opening mode fracture growth initiated ahead of the tip of an approaching hydraulic fracture. The plot indicates that as the hydraulic fracture approaches the natural fracture, the width of natural fracture increases, however, the extent of this opening reduces. The natural fracture was assumed to have zero tensile strength in this case.

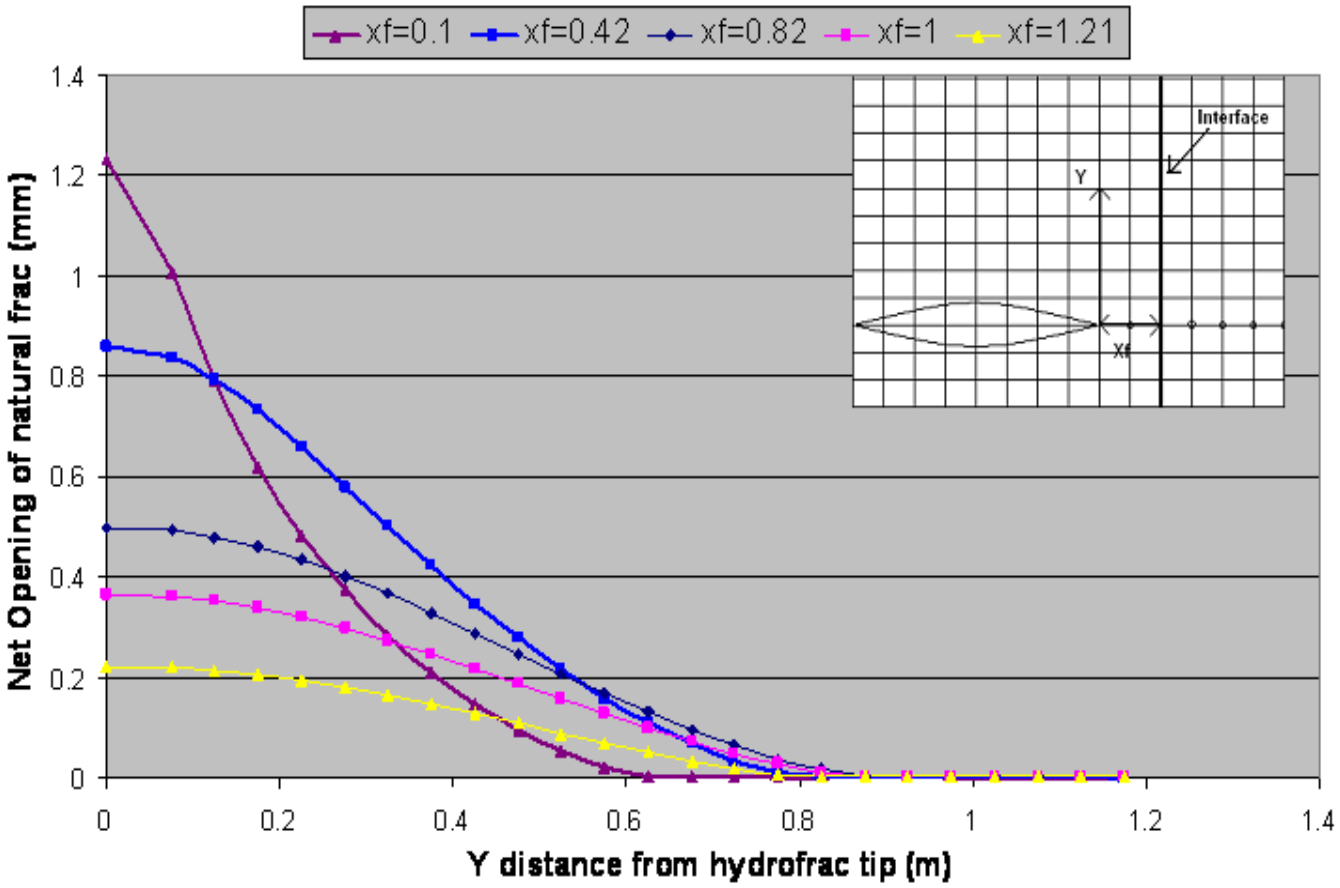

Figure 4-1: Width profile of the natural fracture under the influence of stress field exerted by an approaching hydraulic fracture at different times.

Figure 4-2 shows the maximum width profile of the natural fracture with varying distance of the natural fracture from the hydraulic fracture tip. It shows that the width opening of the natural fracture is less when it is farther away from the hydraulic fracture, which is not difficult to understand since the tensile stresses decrease as we move away from the tip.

To see the effect of plasticity, two plastic models (using Mohr-Coulomb constitutive model) were simulated. In the first case, the cohesion of the rock matrix was

8 GPa, while in the second case, matrix was made softer/weaker by lowering the cohesion to 2 MPa. It was observed that there was no opening or shearing of the natural fracture due to the shear failure of the matrix occurring on the other side of the natural fracture. This indicates that soft shales might not indicate microseismicity in some cases as compared to hard shales.

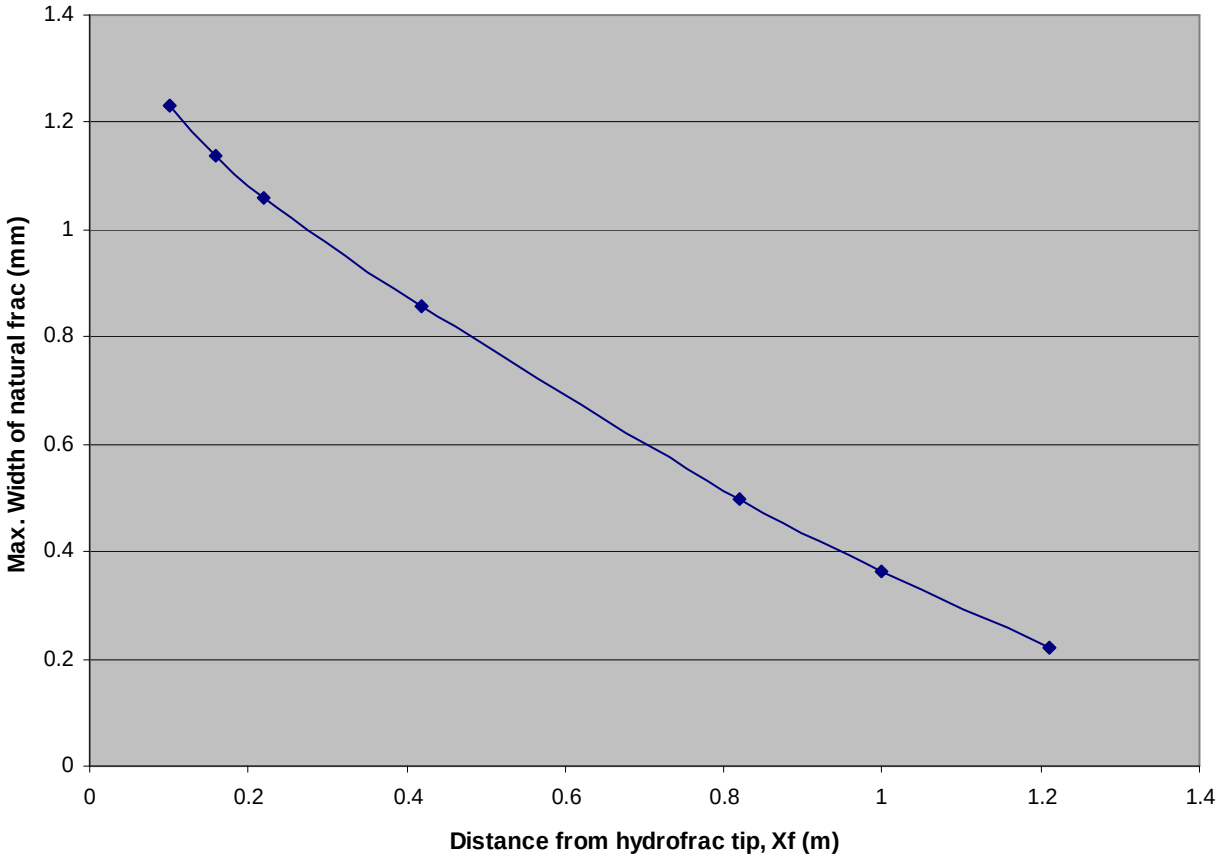

Figure 4-2: Maximum width opening profile of the natural fracture with varying distance between the hydraulic fracture tip and the natural fracture

Similarly, shear stress acting on a natural fracture due to an approaching hydraulic fracture was plotted as shown in Figure 4-3. The shear traction peak is slightly offset with respect to the hydraulic fracture tip with a right lateral shear sense. The analytical

expressions given by Pollard and Segall (1987) above also give the similar shear traction profile.

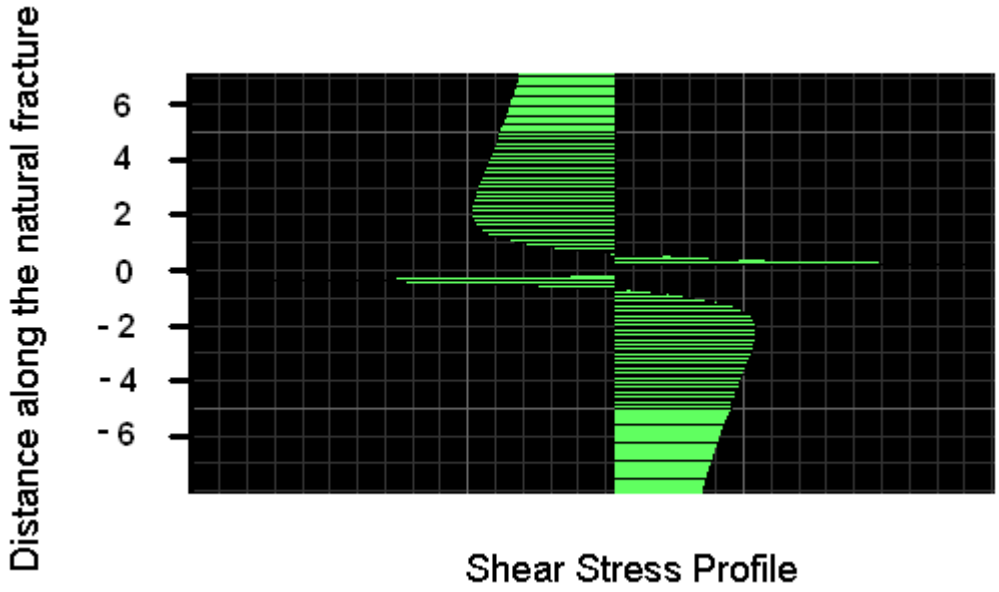

Figure 4-3: Profile of the shear stresses exerted by an approaching hydraulic fracture on the orthogonal natural fracture. Distance between the fracture tip and the natural fracture was approximately 0.04 m.

The next step, i.e. the interaction between the hydraulic fracture and the natural fracture at the moment when hydraulic fracture tip just intersects the natural fracture, was modeled using an interaction criterion previously stated in Chapter 3. It is repeated below for convenience.

For crossing to occur, stresses exerted by the hydraulic fracture tip should be such that the interface doesn't slip, and rock fails in tension on the other side of the interface to initiate a new fracture. If, however, interface slips, the stresses exerted by the

fracture tip aren't transmitted to the other side forcing hydraulic fracture to be either arrested momentarily, or dilate the natural fracture and propagate along it.

Figure 4-4 shows the grid and the natural fracture (non-orthogonal) along with the far-field stresses used for this simulation. Note that the hydraulic fracture tip just touches the natural fracture. Fluid pressure inside the fracture was not constant, and an analytical expression (Eq. 3.16) was used. The orientation of the natural fracture with respect to the hydraulic fracture was varied in simulations and its effect is discussed in the next section.

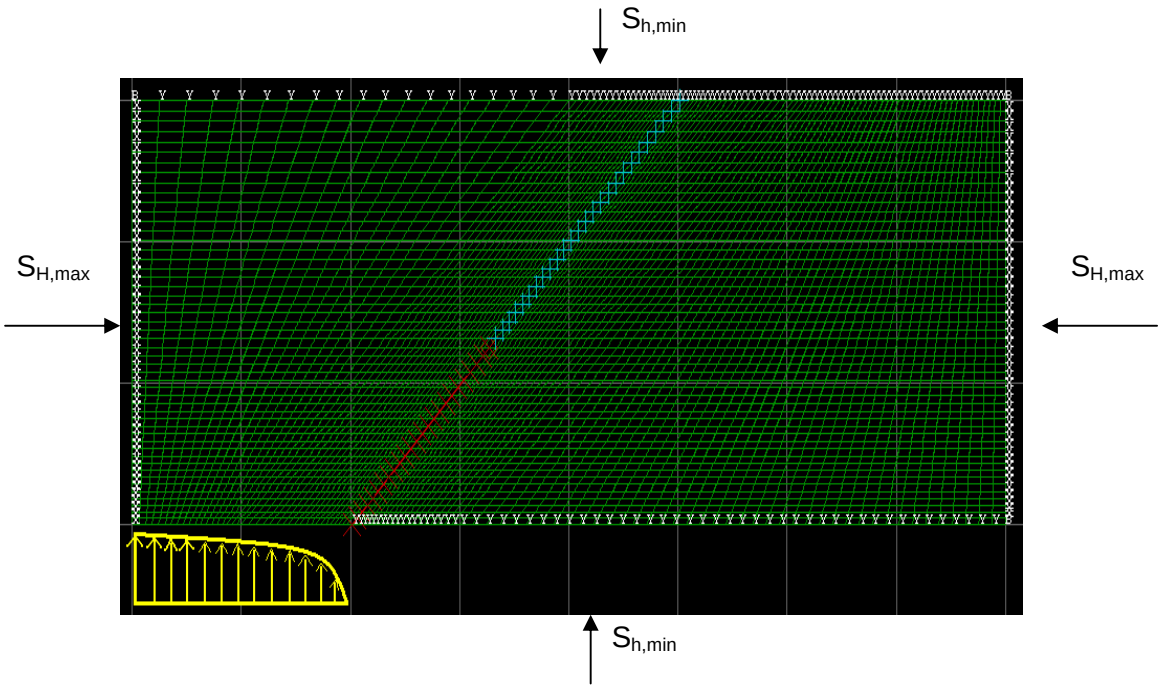

Figure 4-4: Grid used in the model. White marks on the boundary indicate zero normal displacement boundary condition. Red line indicates the interface element (i.e. natural fracture) and light blue line indicates the grid points attached together (no natural fracture)

Figure 4-5 shows the results using the fracture interaction criterion described above. In this plot, orientation of the natural fracture was fixed at 75 degrees, and the effect of differential horizontal stress (S_{Hmax}-S_{hmin}) and coefficient of friction of the

natural fracture can be seen. For this case, cohesion of the natural fracture was assumed to be zero. It shows that as the differential horizontal stress increases, it is easier for the hydraulic fracture to cross the natural fractures of lower friction angle. The plot also indicates that one might draw a line, to the right of which is the region for crossing, and to the left is the region for slippage of the natural fracture or arrest of the hydraulic fracture.

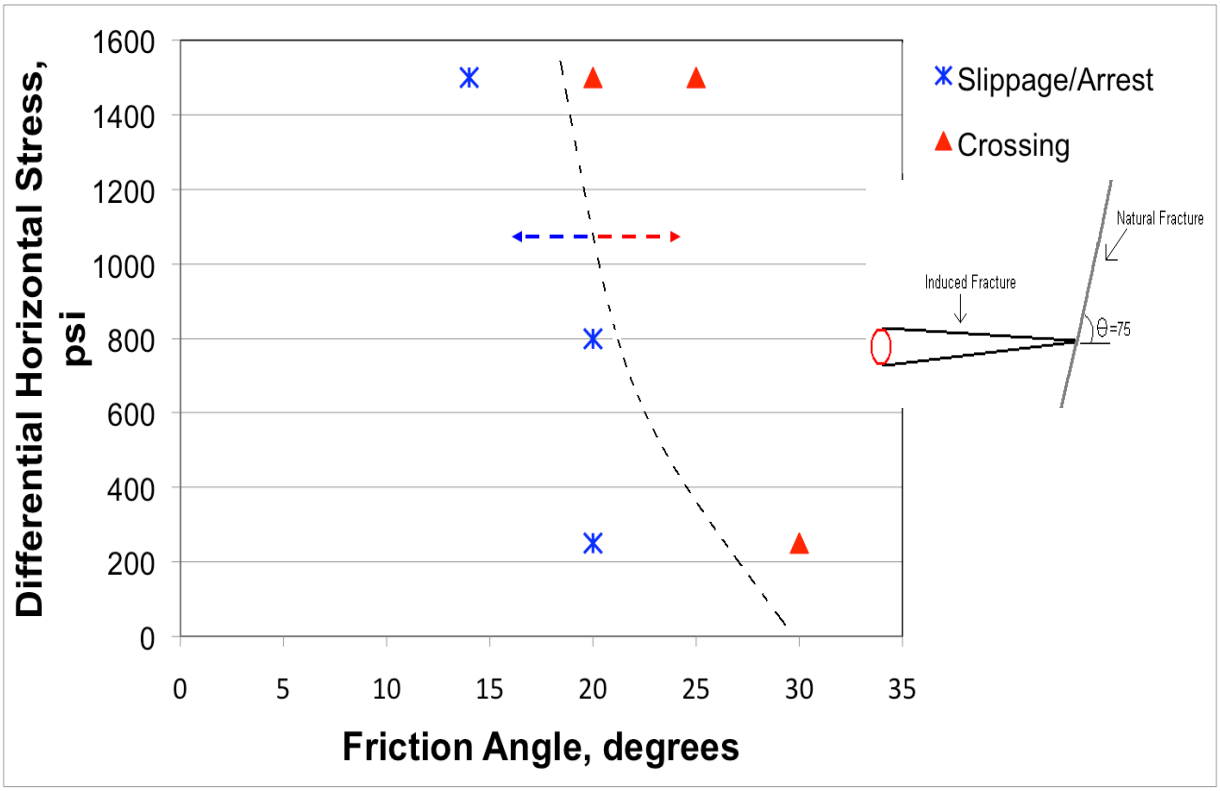

Figure 4-5: Effect of friction angle and horizontal differential stress on the fracture interaction (for a fixed orientation of the natural fracture). The dashed curved line separates the region of crossing from the region of slippage/arrest. Cohesion of the natural fracture was assumed to be zero.

Figure 4-6 below shows the fracture interaction behavior for different orientations of the natural fracture with respect to the hydraulic fracture. Here, coefficient of friction

of the natural fractures is fixed at μ=0.58 and cohesion is again assumed to be zero. The plot indicates that as the angle increases from 90^{o} (representing orthogonal natural fracture), the tendency of the hydraulic fracture to simply cross the natural fracture decreases and it is more likely to get arrested or propagate along the natural fracture. The plot indicates that the fracture interaction behavior is very sensitive to the orientation of the natural fracture. The typical values of coefficient of friction observed in the field are around 0.5-0.9. Thus, the parameters chosen are realistic in nature. A very similar work has been done by Gu et al. (2011). They developed a comprehensive hydraulic fracturing simulator using a similar interaction criterion. Their model too predicts similar results for interaction between a hydraulic fracture and an existing natural fracture. A more detailed discussion of their work will be presented in the next chapter.

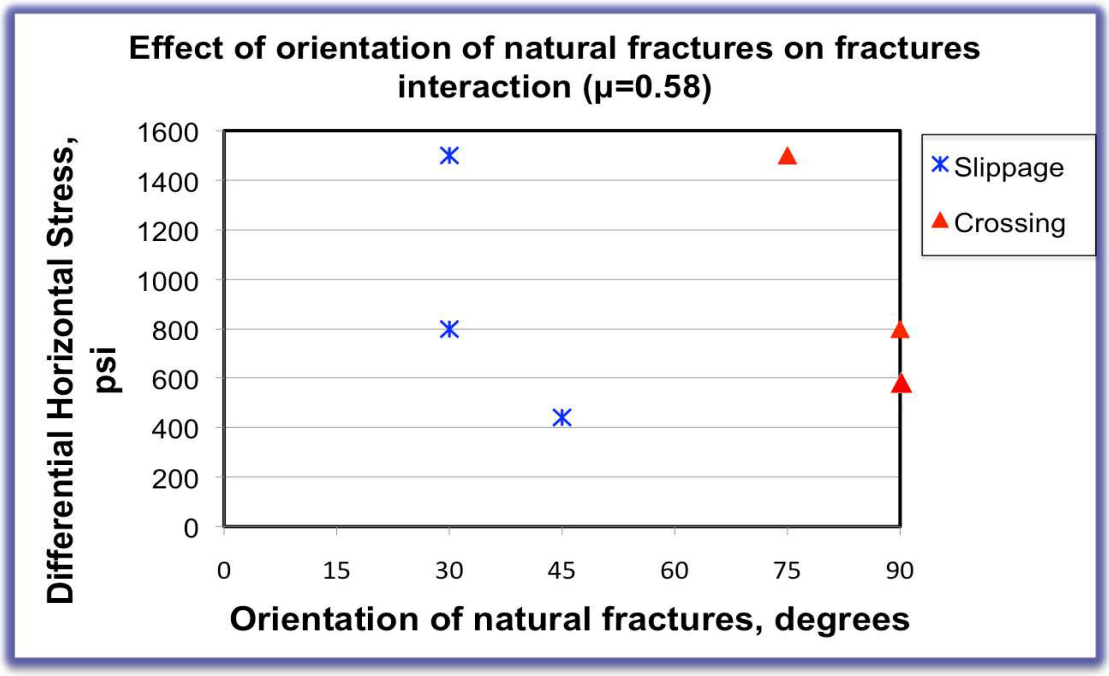

Figure 4-6: Effect of angle of orientation of the natural fracture on the fracture interaction (for a fixed coefficient of friction value for the natural fracture). Cohesion is again assumed to be zero.

In the case of slippage or arrest, there are two further possibilities for fracture propagation as shown in Figure 3-7. The hydraulic fracture can either be arrested by the natural fracture, or it can dilate the natural fracture and propagate along it. These two possibilities depend on the fluid pressure of the hydraulic pressure. If the fluid pressure near the tip is greater than the normal stress acting on the natural fracture, natural fracture will open up and hydraulic fracture may propagate along it. If, however, the fluid pressure is lower than the normal stress acting on the natural fracture, hydraulic fracture will remain arrested, at least for sometime. Figure 4-7 below shows the conditions under which these two possibilities might occur. The coefficient of friction was again fixed to be 0.58 and cohesion of the natural fracture was again set to zero. The plot indicates that as the differential horizontal stress decreases, hydraulic fracture is more likely to dilate the natural fracture and might propagate along it. Table 4-1 lists the values of some key parameters that were used in these simulations.

Model Validation

The results obtained from the developed geomechanical model, using the abovementioned fracture interaction criterion, were compared with the experimental results published in the literature. As mentioned in Chapter 2, Zhou et al. (2008) performed laboratory hydraulic fracturing experiments to investigate the fracture propagation in the cement blocks with pre-fractures. He used three types of paper – rice paper, printer paper, and wrapping paper (with coefficient of friction being 0.38, 0.89, and 1.21 respectively). The cohesion of paper was measured to be around 3.2 MPa and the tensile strength of the 300 mm cube blocks used was found to be around 3 MPa. Although majority of the cases were compared with the experimental results, only the comparison with the experimental results obtained from the rice paper tests has been

shown here. The comparison between the model and the experimental results can be seen in the Figure 4-8.

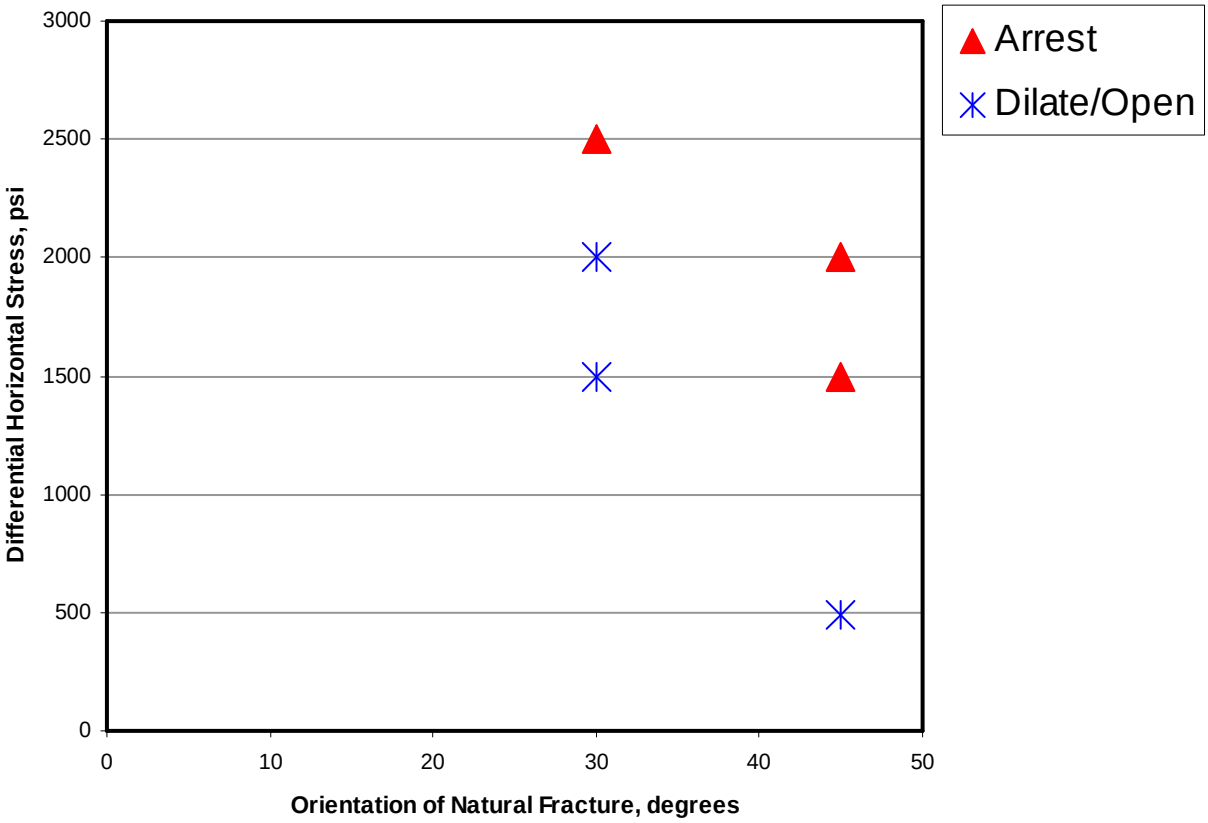

Figure 4-7: Plot showing the effect of orientation of the natural fracture and the differential horizontal stress on the fracture interaction for the cases when the hydraulic fracture does not cross the natural fracture.

From the Figure 4-8, it can be seen that the numerical results are in good agreement with the experimental results. There is only one discrepancy for the case of orientation of 60^{o}. The model suggests hydraulic fracture crossing the natural fracture at that orientation of the natural fracture and the given stress state, but experiments showed no crossing. Although there is no obvious reason for this discrepancy, one possible

reason could be the thickness of the paper used in the experiments that might have suppressed crossing. The overall comparison and good match validates the fracture interaction criterion used in this model and suggests that it can be used in more rigorous hydraulic fracturing simulators for unconventional reservoirs.

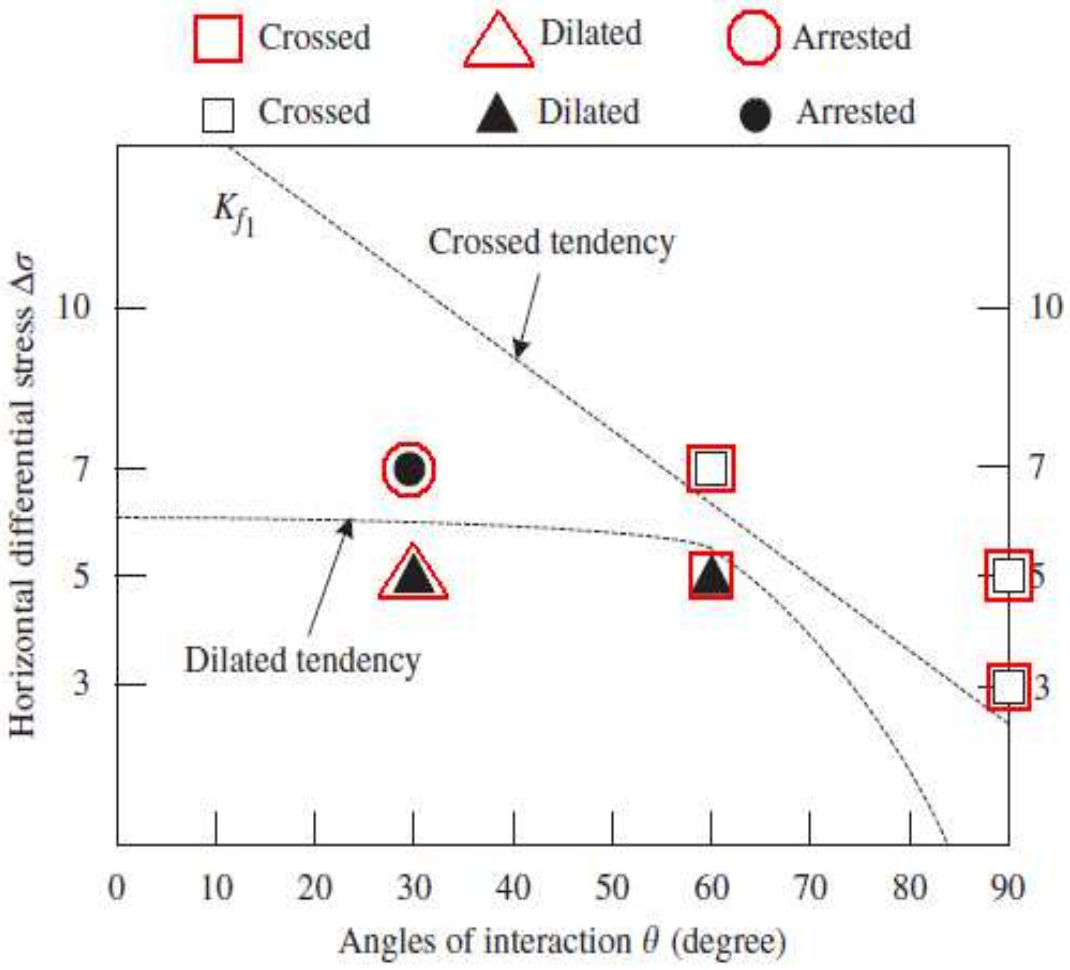

Figure 4-8: Comparison of model results with experimental results obtained by Zhou et al. (2008). The labels in red correspond to the model results and the labels in black correspond to the experimental results.

IMPACT OF GEOMECHANICS ON MICROSEISMIC ACTIVITY

In this section, the results for quantifying the extent microseismic activity cloud generated from hydraulic fracturing in the presence of weak planes have been presented. It should be noted that only the effect of hydraulic fracture tip (and resulting geomechanics) is considered in this work. Other factors, mentioned in Chapter 3, have not been included.

Figure 4-9 shows the contour plot of f^s for a 3D hydraulic fracture. The properties have been listed below in Table 4-1. The f^s in this plot has been calculated for the most favorable case i.e. assuming weak planes are favorably oriented at different locations, have coefficient of friction, μ, 0.6, and have zero cohesion. It can be seen from the plot that the failure cloud for potential microseisms is very small and extends only up to 10m from the fracture tip. Generally, the uncertainty associated with microseismic itself is of the same order and thus, we can conclude that the fracture tip phenomenon doesn't play much role in microseismicity in these scenarios.

Table 4-1: List of properties used for Figure 4-9

Parameters	**Values**
Overburden Stress, S_v, psi	12,000
Maximum Horizontal Stress, S_{Hmax}, psi	11,300
Minimum Horizontal Stress, S_{hmin}, psi	10,800
Pore Pressure, P_p, psi	9,700
Net Fluid Pressure, P_{net}, psi	830
Pay Zone Height, ft	196

Please note that the in-situ stress state for the case above is very stable whereas, many of the shale plays are overpressured. Since the effective stress is lower in those reservoirs (because of high pore pressure), any change in stresses around the fracture tip can greatly destabilize the weak planes and can cause them to fail up to farther distance. One such case is shown in the Figure 4-10. The reservoir properties are listed in the Table 4-2 (Buller (2010), Thompson et al. (2011)). Please note that the pore pressure (or, reservoir pressure) is very high. These properties are typical for Haynesville shale, located around southwestern Arkansas, northeast Louisiana and east Texas, and at large depths of 10,500 to 13,000 ft below the surface. It can be seen from the plot that contrary to the Figure 4-9, the potential microseismic cloud extends to a very large distance (around 45m from the fracture tip). Thus, we can say that fracture tip phenomenon could play a very critical role in generating microseismicity farther away into the reservoir especially when the formation is highly overpressured.

Table 4-2: List of properties used for the case of Haynesville shale

Parameters	**Values**
Overburden Stress, S_v, psi	12,000
Maximum Horizontal Stress, S_{Hmax}, psi	11,300
Minimum Horizontal Stress, S_{hmin}, psi	10,800
Pore Pressure, P_p, psi	10,190
Net Fluid Pressure, P_{net}, psi	830
Pay Zone Height, ft	196

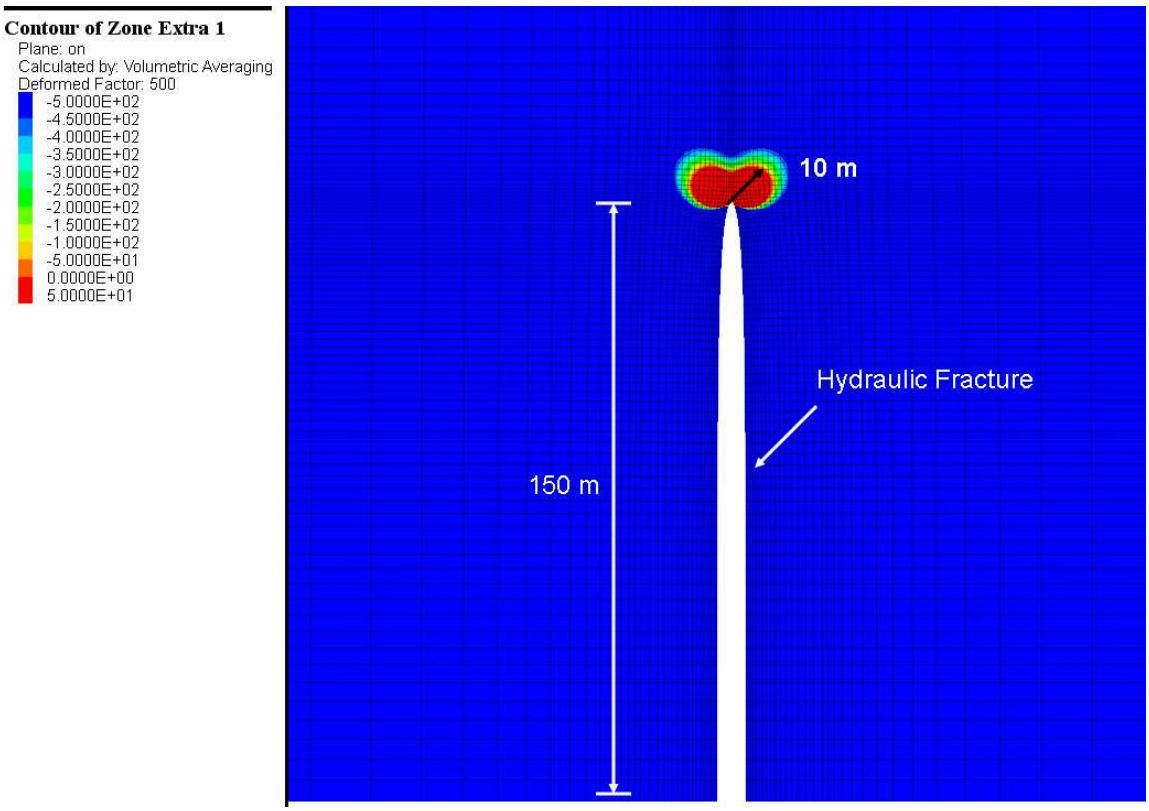

Figure 4-9: Contour map of f^s for a single hydraulic fracture. The area in the dark red indicates the potential failure zone for weak planes.

To underline the significance of fracture tip phenomenon in generating microseismicity in overpressured formations, another set of simulations was performed. The model properties are listed in Table 4-3 (Mayerhofer et al. (2006)). These properties are typical and representative of Barnett shale, located around Fort Worth basin in Texas, one of the largest gas plays in U.S. The contour map indicating potential microseismicity is shown in Figure 4-11. Again, it can be seen that the potential microseismic cloud extends to a very large distance (around 80m from the fracture tip).

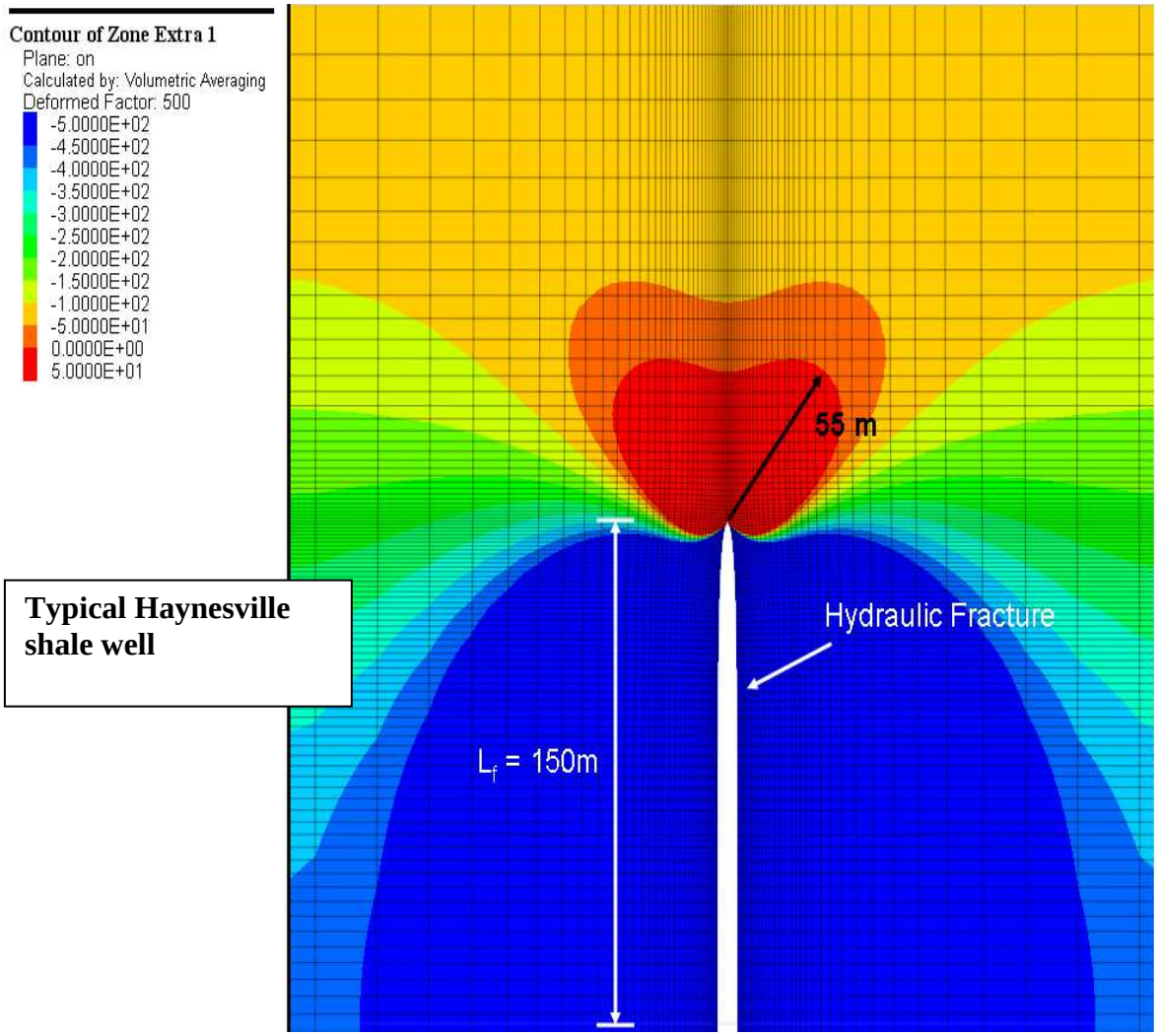

Figure 4-10: Contour map of f^s for a single hydraulic fracture for the properties listed in Table 4-2. The area in the dark red indicates the potential failure zone for weak planes. Note that the failure zone in this case is far bigger than as shown in Figure 4-9.

Table 4-3: List of properties used for the case of Barnett shale

Parameters	Values
Overburden Stress, S_v, psi	7,000
Maximum Horizontal Stress, S_{Hmax}, psi	5,100
Minimum Horizontal Stress, S_{hmin}, psi	4,900
Pore Pressure, P_p, psi	3,900
Net Fluid Pressure, P_{net}, psi	600
Pay Zone Height, ft	196

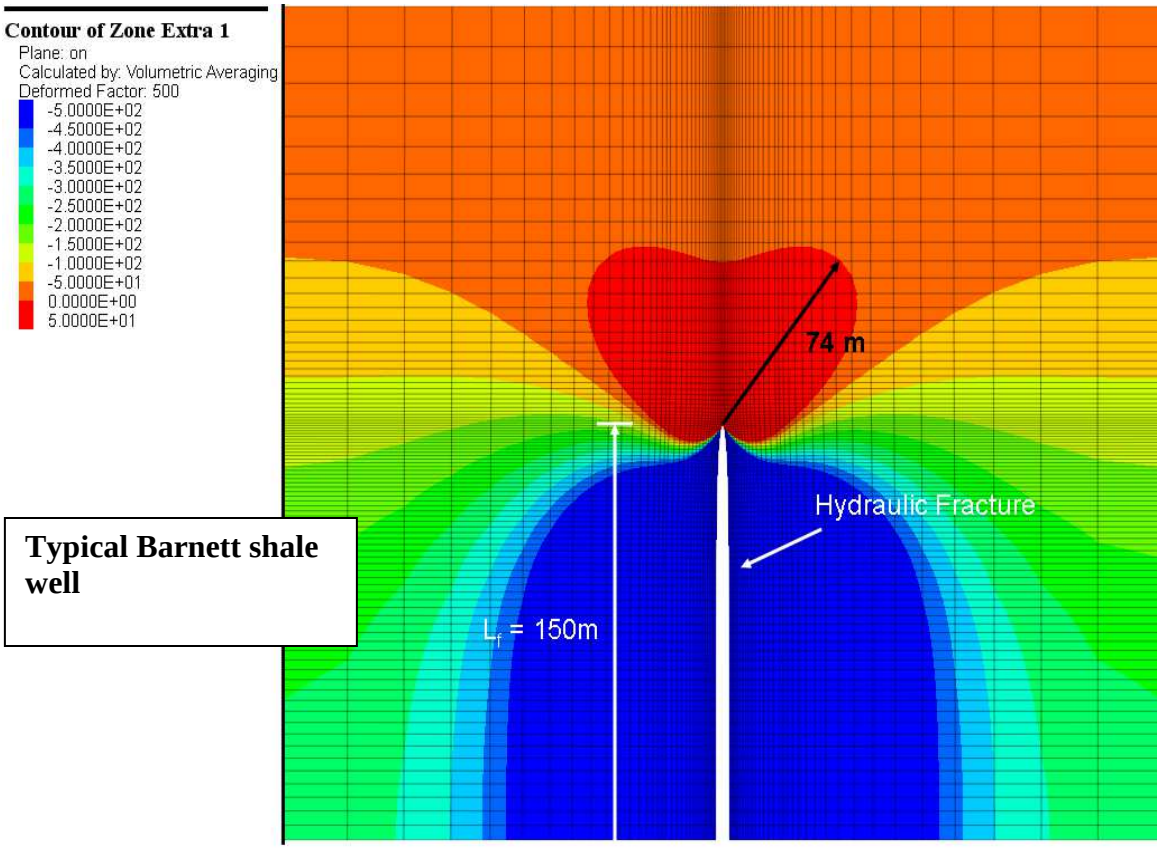

Figure 4-11: Contour map of f^s for a single hydraulic fracture for the properties listed in Table 4-3. The area in the dark red indicates the potential failure zone for weak planes. Note that the failure zone in this case is far bigger than as shown in Figure 4-9.

Microseismicity for Multiple Fractures

One of the most important steps in fracture treatment design is the fracture spacing. There are many factors like stress reversal around a fracture, interaction between multiple fractures, growth of simultaneous multiple fractures that need to be taken into account while designing fracture spacing (Olson (2008), Roussel and Sharma (2011)). In unconventional reservoirs, a complex fracture network is often desired instead of a simple bi-planar geometry because the complex network (resulting from interaction with weak planes or shearing/slippage of weak planes far away) results in more surface area in the formation. Generally, this complex fracture is deduced from the large scattering of microseismic data on a plane. Thus, another factor that could influence fracture spacing is the goal to generate microseismicity in the maximum possible region between the two fractures. In other words, the fracture spacing should be such that the potential microseismic cloud should cover the entire region between the two fracture tips (since only the fracture tip phenomenon is considered in this work). The closer the fracture spacing, greater is the extent of this potential microseismic cloud; however the cost of the fracture treatment will also rise. Therefore, a balance has to be maintained between the stimulated volume and the cost of the treatment.

Several simulations were performed for two hydraulic fractures with varying spacing between them (Figure 4-12 to Figure 4-15) using the properties listed in Table 4-2. It can be seen from these figures that for shorter fracture spacing, the potential microseismic clouds from the two fractures overlap and cover the entire region between the fractures. As the fracture spacing increases, this overlap region decreases and after certain spacing (referred to as maximum spacing from here onwards), there exists a region between the two fractures where no microseismicity could be observed. Therefore, to maximize the chances of a potential complex fracture network, one should space the

fractures closer than this maximum spacing. Please note that this "maximum spacing" will vary from one case to another as it depends on several parameters including in-situ stress state, fluid pressure inside the fracture, length of the fracture, mechanical properties of the formation, etc.

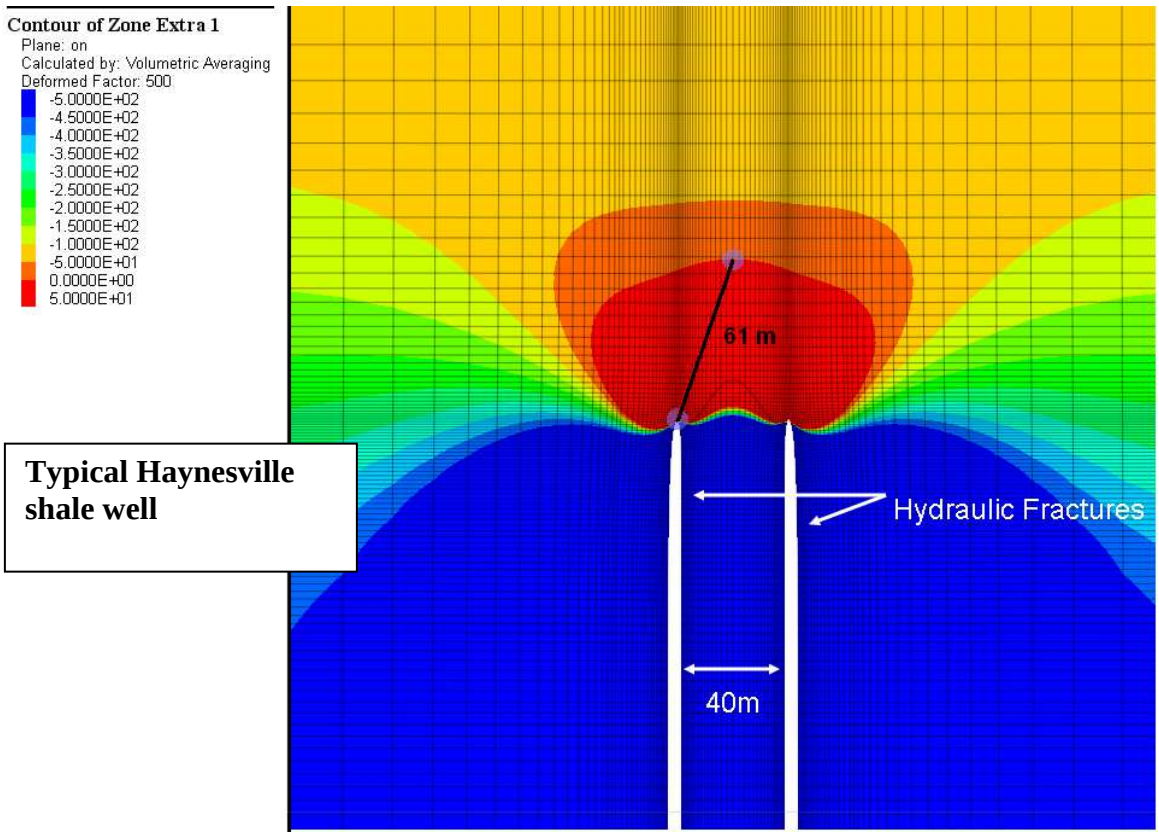

Figure 4-12: Contour map of f^s for the fracture spacing of 40m. The area in the dark red indicates the potential failure zone for weak planes. Length of the fracture is 150m.

Another way of looking at the desirable fracture spacing is to plot a normalized microseismicity zone area versus fracture spacing. The normalized microseismic area (NMSA) is defined as following:

$$NMSA = \frac{A_{multifrac}}{A_{\sin glefrac}} \tag{4.5}$$

where $A_{singlefrac}$ is the half of the total microseismicity area (on the plane z=0 i.e. plane of maximum fracture width) generated by a single hydraulic fracture, and $A_{multifrac}$ is the half of the microseismicity area confined between the two hydraulic fractures (as shown in Figure 4-16).

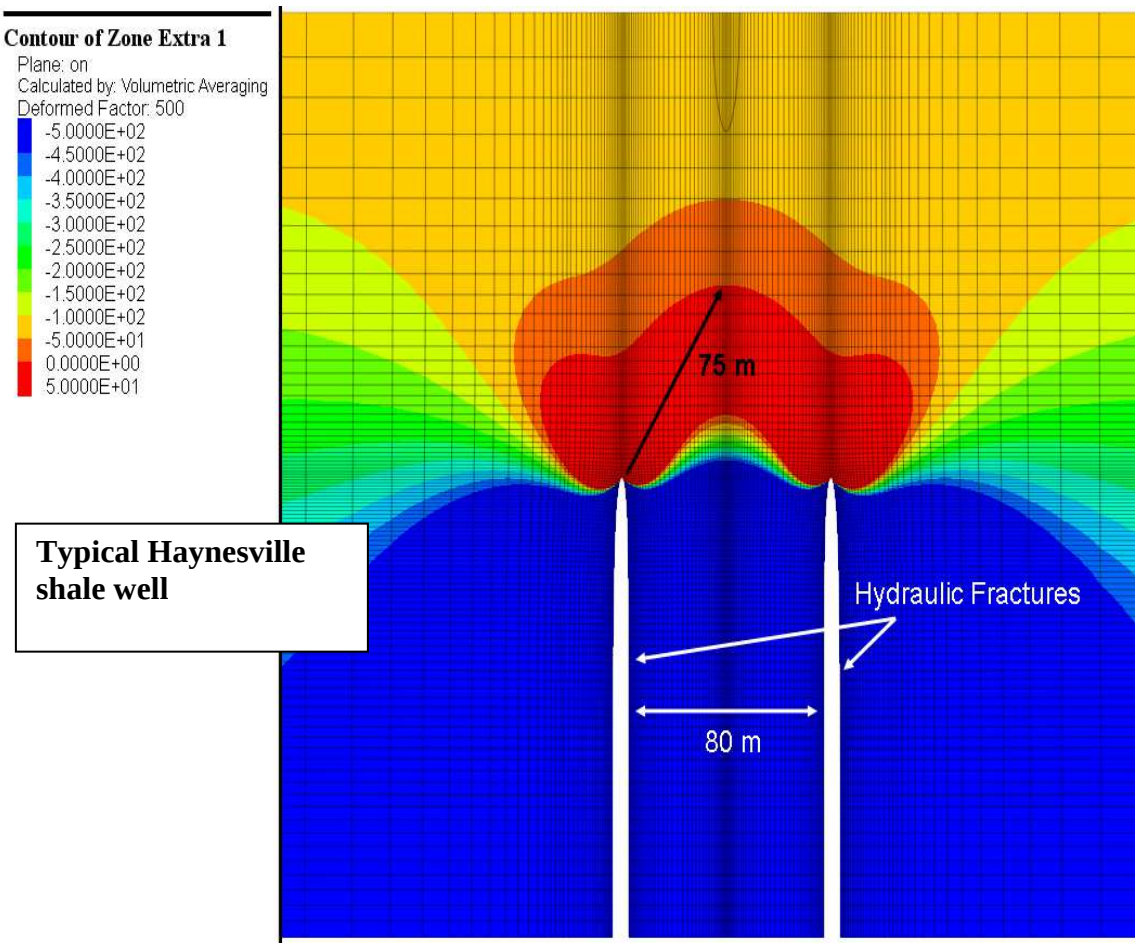

Figure 4-13: Contour map of f^s for the fracture spacing of 80m. The area in the dark red indicates the potential failure zone for weak planes. Length of the fracture is 150m.

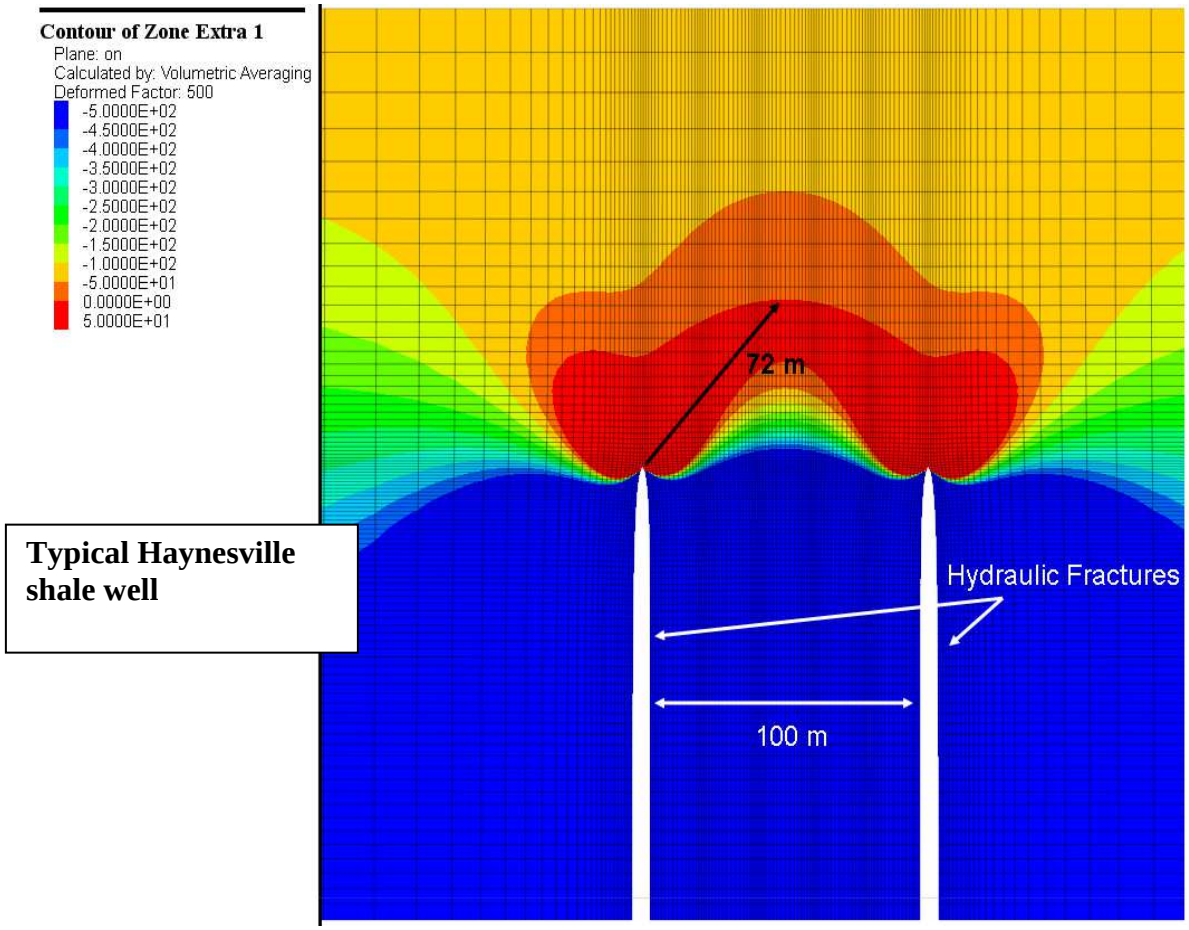

Figure 4-14: Contour map of f^s for the fracture spacing of 100m. The area in the dark red indicates the potential failure zone for weak planes. Length of the fracture is 150m.

It should however be noted that in the case of more than one hydraulic fracture, there is a mechanical interaction between the two fractures which affects the aperture of both the hydraulic fractures at the fracture mid-height (or length). This mechanical interaction can be quantified by a stiffness multiplier, ψ, which depends primarily on the ratio of fracture spacing and height of the fractures. This stiffness multiplier decreases with d/h ratio and becomes negligible at dimensionless spacing greater then three (Meyer

(2011)). Thus, in our simulations, to normalize the microseismic volume, we constrained the total width of the fractures to be same as the total width of the single fracture in the base case. This meant that a higher fracturing pressure was required in multi-fracture simulations as compared to the base case.

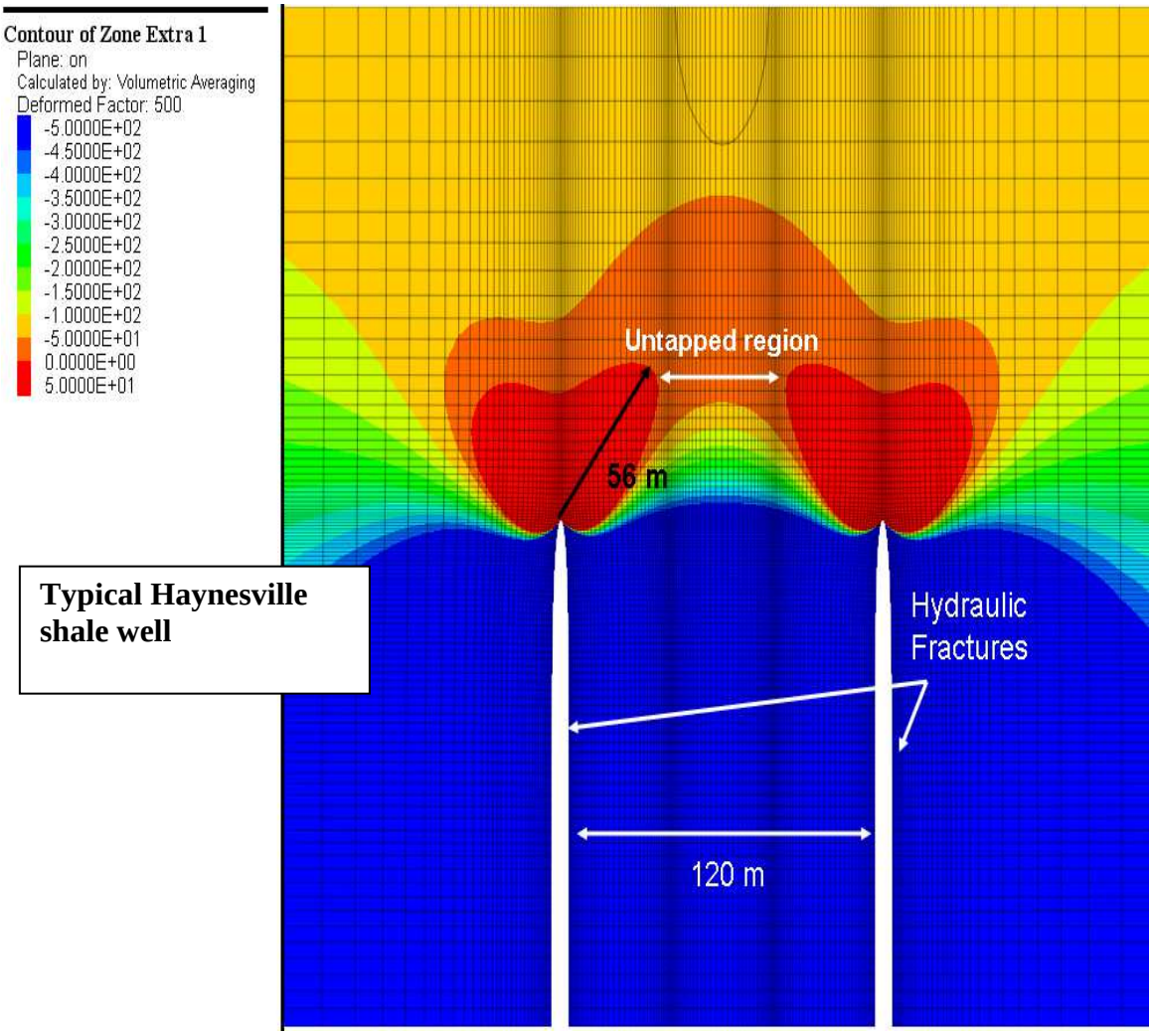

Figure 4-15: Contour map of f^s for the fracture spacing of 120m. The area in the dark red indicates the potential failure zone for weak planes. Length of the fracture is 150m. Note that the potential failure zones for two fractures don't overlap and there exists a region in the middle where no potential microseismic activity could be observed.

The normalized microseismic area was then plotted versus the fracture spacing for different cases of stress state, net fluid pressure, cohesion of weak planes, etc. (Figure 4-20 to Figure 4-23). It can be seen from the plots that there exists an optimum fracture spacing for which potential microseismicity zone could be maximized. It could prove to be very helpful in fracture treatment design for some of the overpressured unconventional formations.

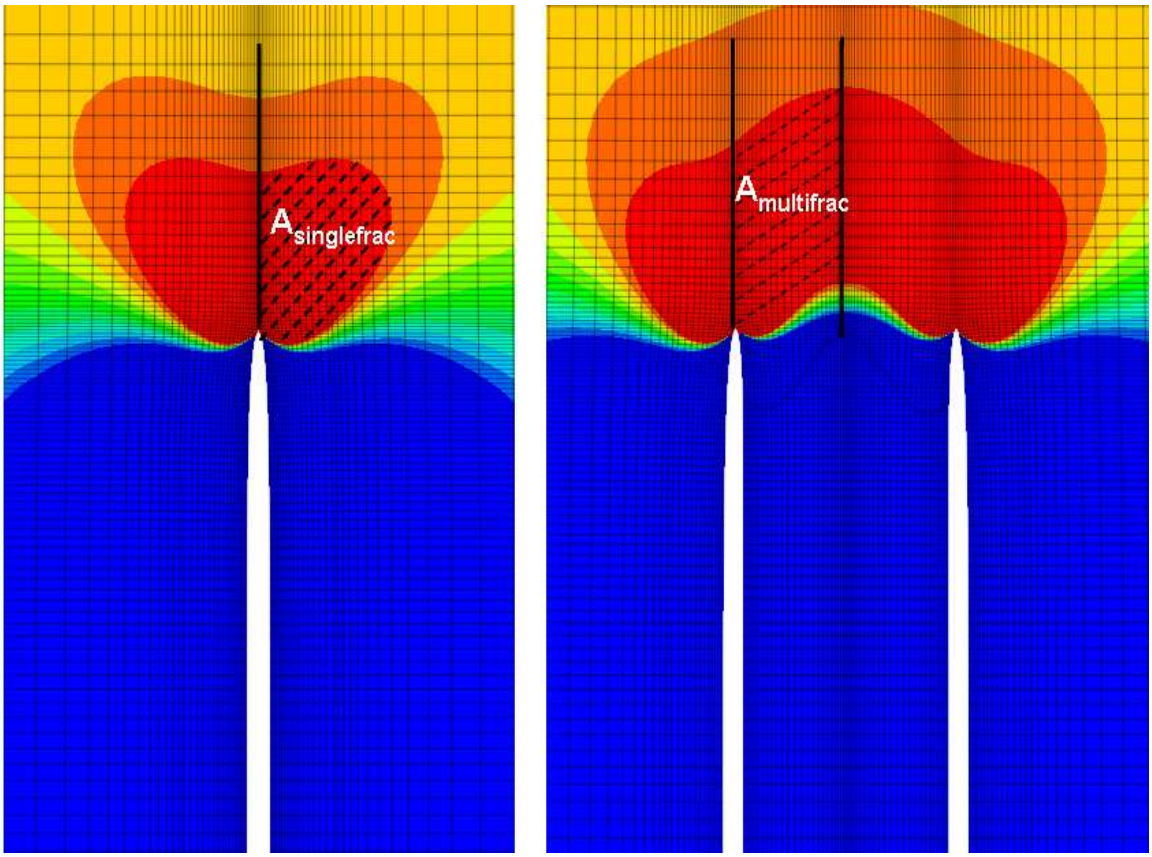

Figure 4-16: Contour maps for fs defining $A_{singlefrac}$ and $A_{multifrac}$ (used in Eq. 4-5). The zone in the dark indicates the potential microseismicity zone. The zones covered by dotted lines denote the defined areas.

Figure 4-17 shows the normalized microseismic volume versus fracture spacing for typical fracturing parameters in two different formations; Haynesville and Barnett shale. These parameters are listed in Table 4-2 and 4-3 respectively. It can be seen from the plot that the optimum fracture spacing varies for two different stress states and one can go with higher fracture spacing in the Barnett as compared to the Haynesville shale. Also, one should note that the normalized microseismic volume (Norm MSV) will tend to reach unity as the fracture spacing becomes very high as there will be no mechanical interaction between the fractures and the interior widths will be same as that of the base case.

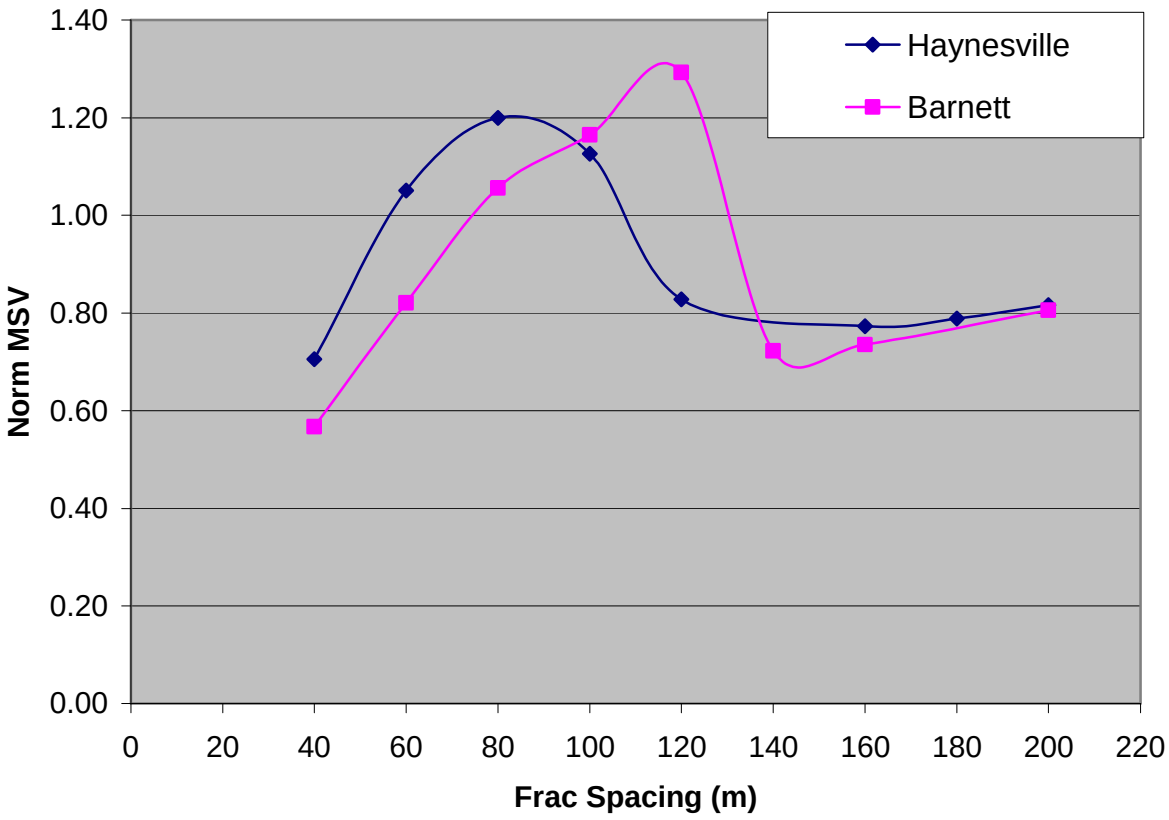

Figure 4-17: Plot of Normalized Microseismic Volume (Norm MSV) versus Fracture spacing for two typical fracturing and reservoir parameters.

Similarly, other factors including total fracture widths, fracture half-lengths, Poisson's ratio (ν) of the formation, Young Modulus (E) of the formation, cohesion of the weak planes were varied and Norm MSV versus Fracture spacing was plotted as shown below.

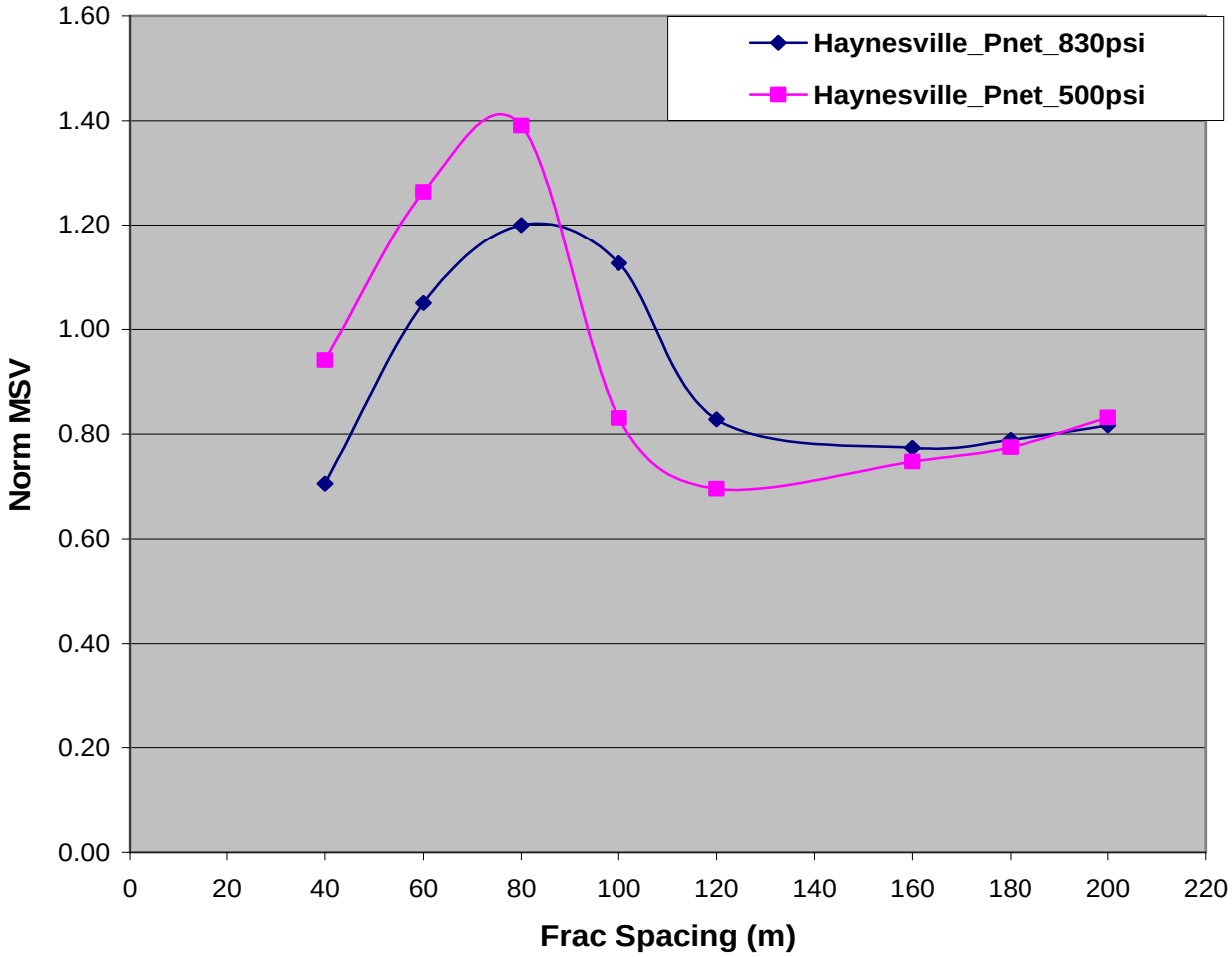

Figure 4-18: Plot of Normalized Microseismic Volume (Norm MSV) versus Fracture spacing for varying fracturing pressure (or, fracture width). Reservoir properties used are listed in Table 4-2.

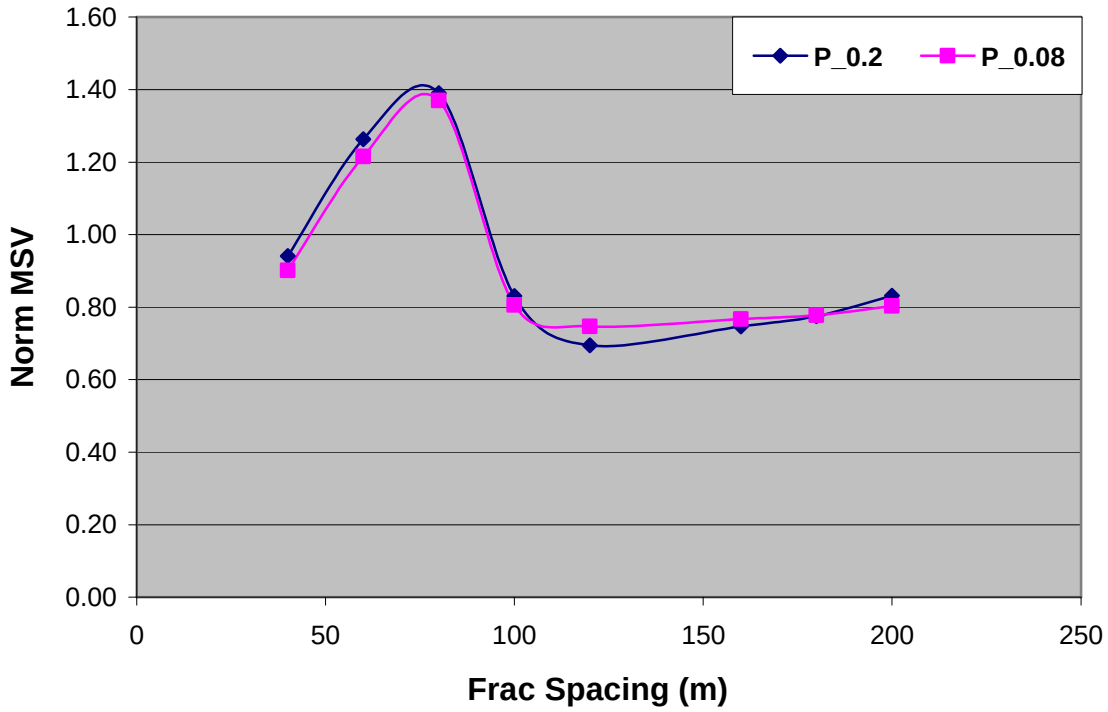

Figure 4-19: Plot of Normalized Microseismic Volume (Norm MSV) versus Fracture spacing for varying Poisson's ratio, ν, of the formation. The reservoir properties and other parameters used are listed in Table 4-2.

It can be seen from the Figure 4-19 that the effect of Poisson's ratio on the potential microseismic activity region, and thus fracture spacing, is not substantial and can be neglected. However, change in Young's modulus has a significant impact on the fracture spacing plot as can be seen in Figure 4-20. In the case of lower Young's modulus, the stresses aren't transmitted to the greater extent and thus there exists a region in the middle of the two fractures where no potential microseismic activity could be recorded even for relatively smaller fracture spacing.

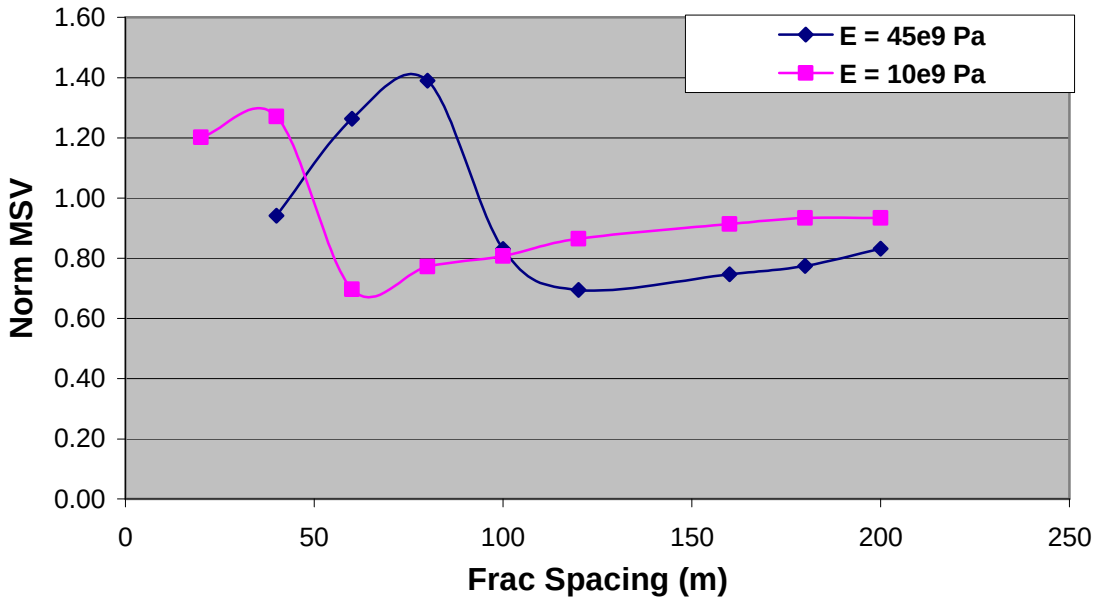

Figure 4-20: Plot of Normalized Microseismic Volume (Norm MSV) versus Fracture spacing for varying Young's modulus, E, of the formation. The reservoir properties and other fracturing parameters used are listed in Table 4-2.

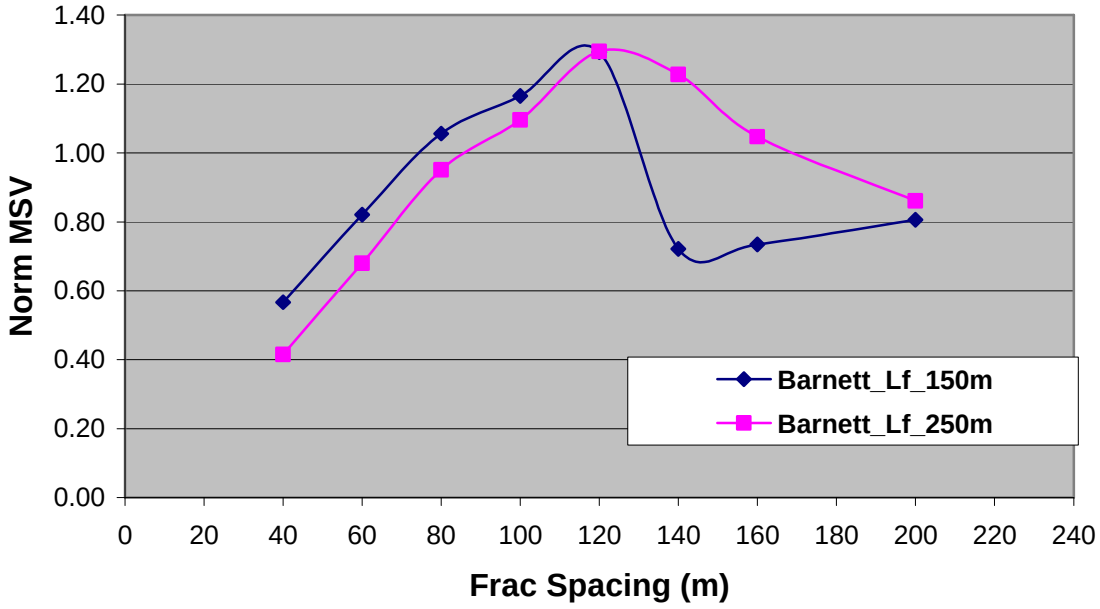

Figure 4-21: Plot of Normalized Microseismic Volume (Norm MSV) versus Fracture spacing for varying fracture half-length, L_f, of the formation. The reservoir properties and other fracturing parameters used are listed in Table 4-3.

Figure 4-22 shows the effect of cohesion of weak planes on the optimum fracture spacing window. Intuitively, as the cohesion of weak planes increases, it is increasingly difficult for them to fail for a given stress state. Moreover, looking at the expression for f^s, one can deduce that the optimum fracture spacing should go down with an increase in cohesion value which is confirmed by the plot below. However, this effect is very substantial and increasing the cohesion even by a little margin greatly reduces the optimum fracture spacing.

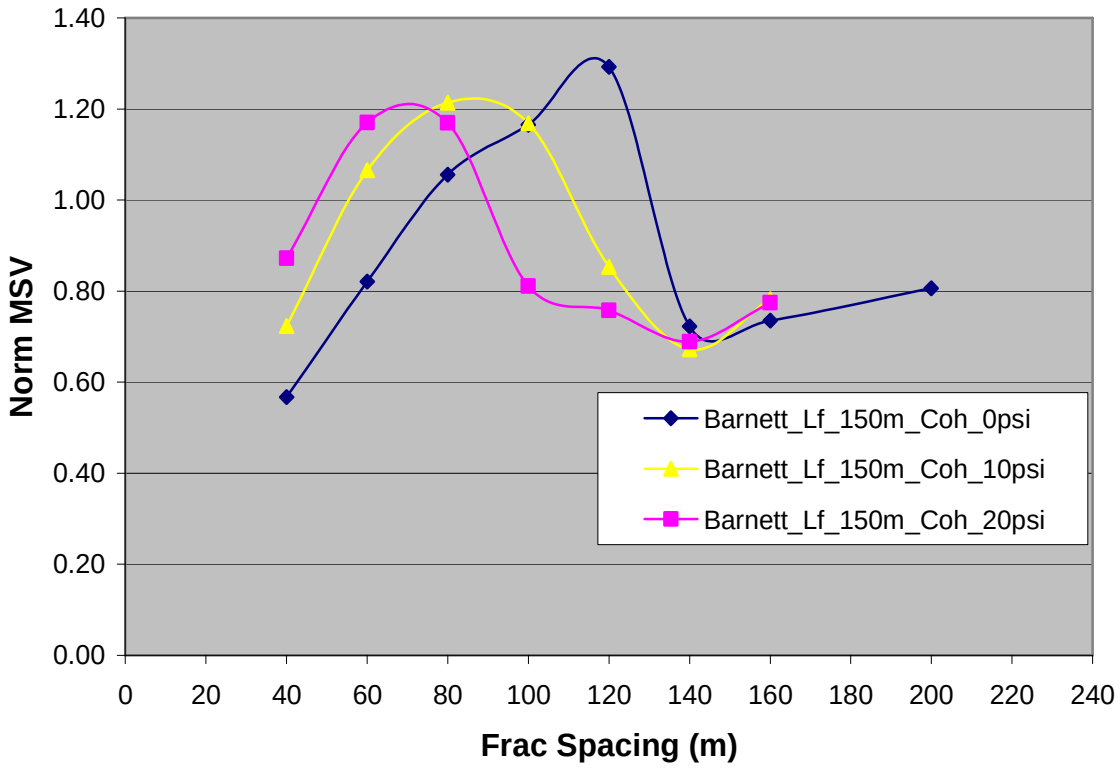

Figure 4-22: Plot of Normalized Microseismic Volume (Norm MSV) versus Fracture spacing for varying cohesion of the weak planes. The reservoir properties and other fracturing parameters used are listed in Table 4-3.

Another set of simulations was performed for a shale play gaining lot of attention and drilling activity in the USA, Eagle Ford shale. Major problem to simulate Eagle Ford shale lies in the fact that the reservoir is highly heterogeneous. The variation in depths, thickness, pressure, etc. is very large and thus, an average set of values was used as input parameters. For example, the depth ranges from 4500-1200 ft; the reservoir pressure is typically 0.6-0.8 psi/ft and so on. The average reservoir properties are listed in the Table 4-4 below.

Table 4-4: List of properties used for the case of Eagle Ford shale (courtesy: BP America Inc.)

Parameters	**Values**
Overburden Stress, S_v, psi	8200
Reservoir Pressure Gradient, psi/ft	0.72
Maximum Horizontal Stress, S_{Hmax}, psi	7183
Minimum Horizontal Stress, S_{hmin}, psi	6683
Pore Pressure, P_p, psi	5904
Net Fluid Pressure, P_{net}, psi	450
Pay Zone Height, ft	196
Young's Modulus, E, psi	2.5×10^6

The plot of Norm MSV versus fracture spacing using these parameters for Eagle Ford shale is shown in Figure 4-23. Due to a very ductile nature of the formation (very low Young's modulus), the extent of potential microseismicity zone is smaller as compared to Barnett or Haynesville shale and thus, the optimum fracture spacing is smaller too, as can be seen in Figure 4-23.

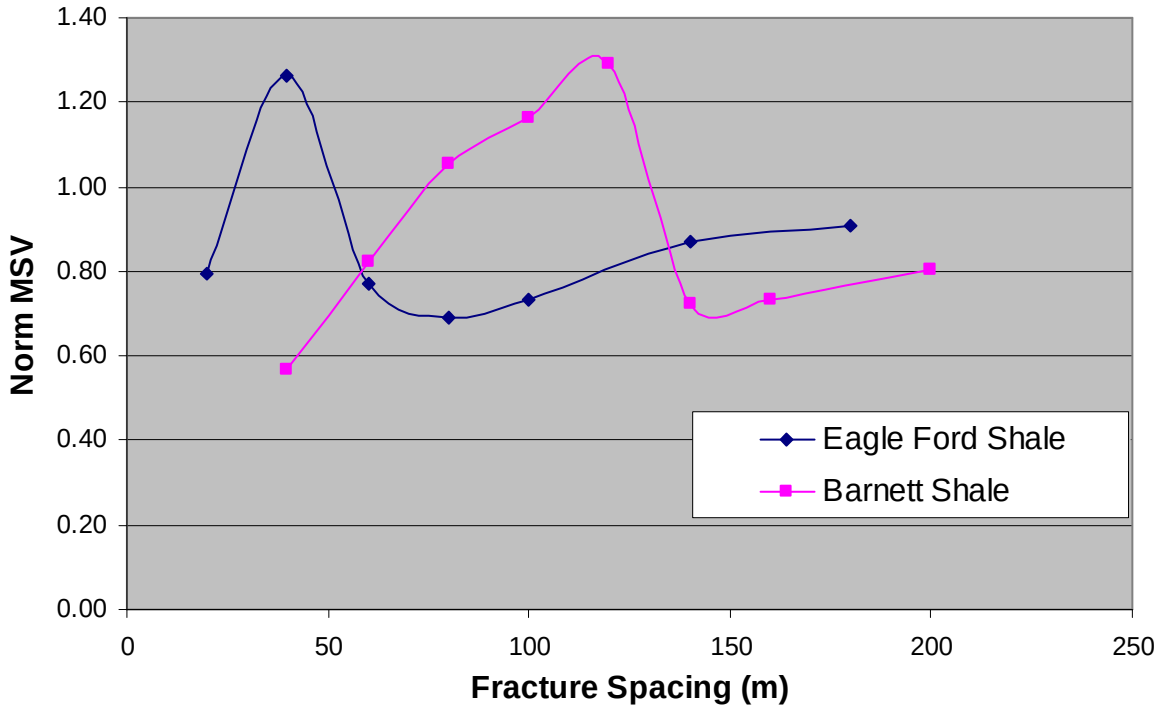

Figure 4-23: Plot of Normalized Microseismic Volume (Norm MSV) versus Fracture spacing for Eagle Ford formation. The reservoir properties and other fracturing parameters used are listed in Table 4-4.

Microseismicity Evolution with Fracture Length

The section above describes and illustrates the potential microseismicity cloud resulting from the stress changes around the fracture tip. It shows that the region behind the fracture tip is in compressive stress state and might not show microseismicity. However, it is likely to observe microseismicity in that region as fracture grows from a small half-length. This section deals qualitatively with the evolution of the potential microseismic volume with time, i.e. as the fracture length grows.

A series of simulations was run with varying fracture lengths, but keeping the fracture width fixed. Figures 4-24 and 4-25 show the potential microseismicity zones for

the case of Barnett shale (i.e. for the parameters listed in Table 4-3). It can be seen from these figures that the entire region between the two fractures, including the region behind the fracture tip, might show microseismicity in the field. Figure 4-26 shows a plot for this microseismic volume versus the fracture length for the cases of Barnett shale and the Eagle Ford shale. The plot shows a maximum, which can be described by the fact that stress field around the fracture tip is directly proportional to $P_{net}*\sqrt{x_f}$. Thus, as the fracture length grows, x_f increases, however, P_{net} required to keep the same width will be lower. Hence, the graph is not a monotonically increasing or decreasing function.

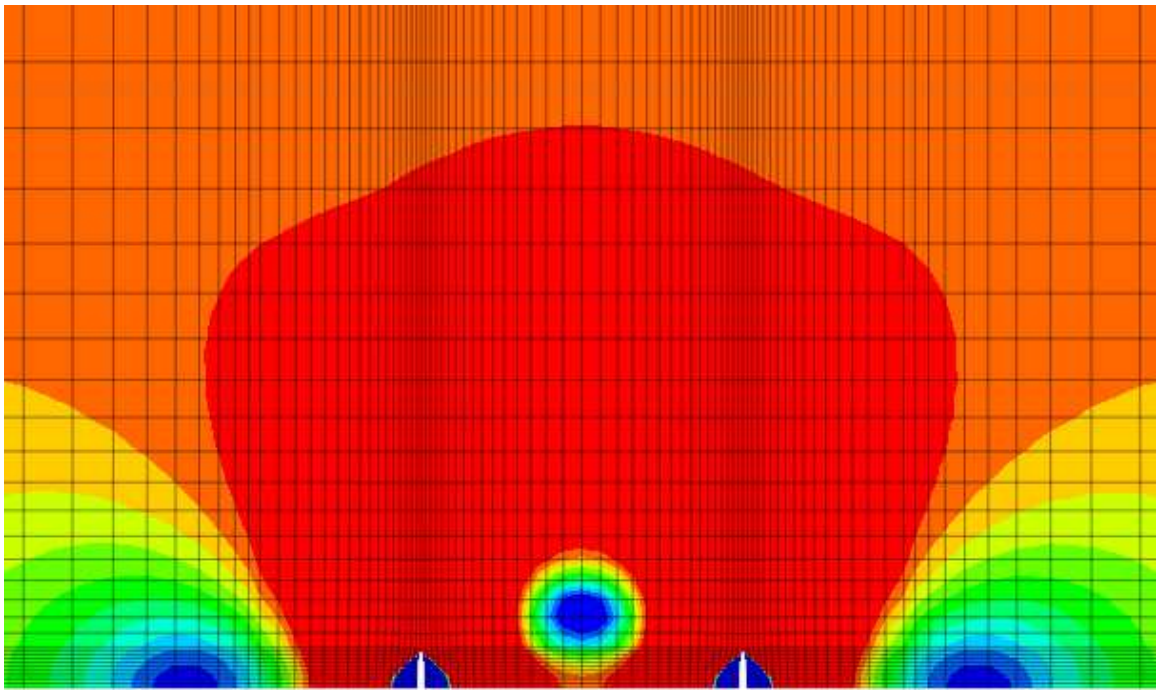

Figure 4-24: Contour map of f^s showing potential failure region (the dark red region) for the fracture length of 5 m.. The reservoir properties and other fracturing parameters used are typical of the Barnett shale, and are listed in Table 4-3.

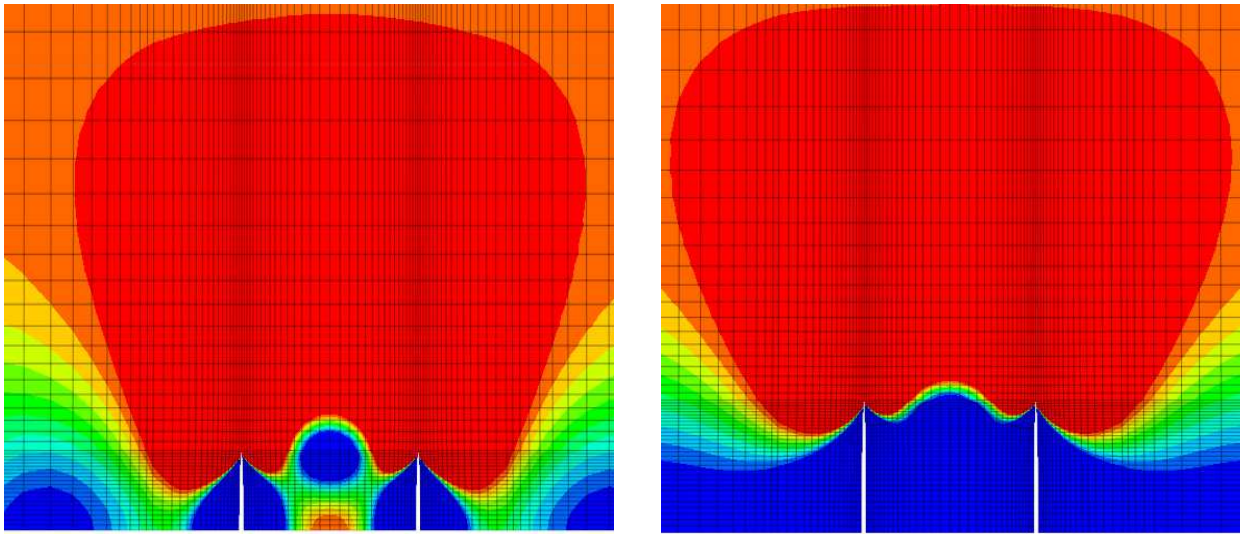

(a) (b)

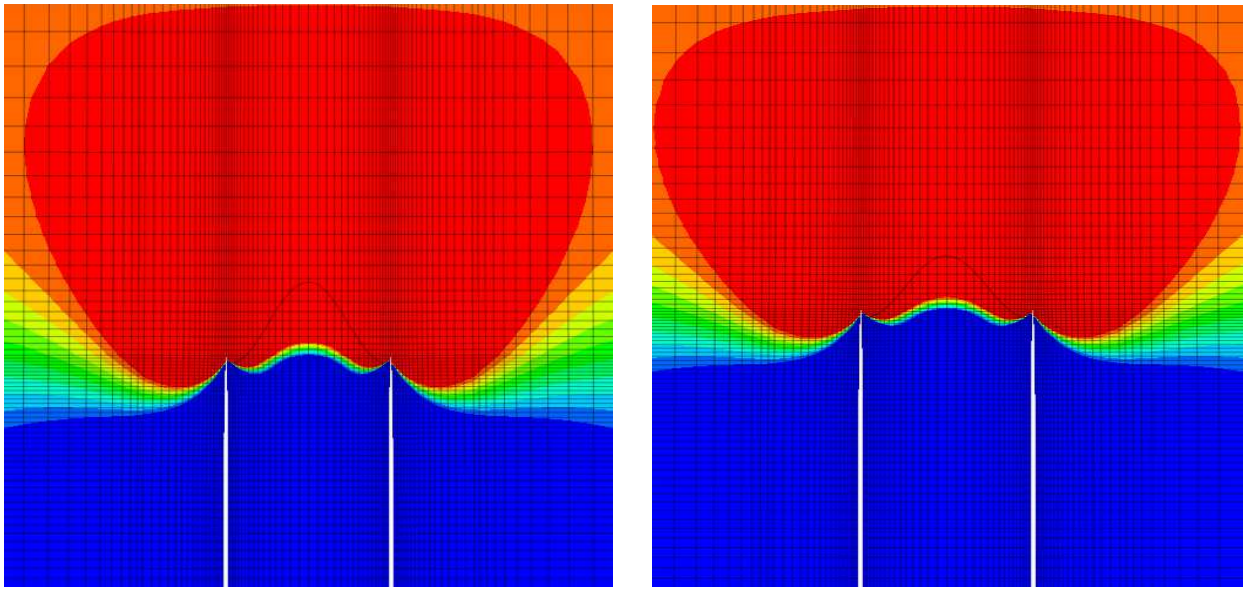

(b) (d)

Figure 4-25: Contour maps of f^s showing potential failure region (the dark red region) for the fracture length of: (a)15 m, (b)30m, (c)60m, and (d)90m. The reservoir properties and other fracturing parameters used are typical of the Barnett shale, and are listed in Table 4-3.

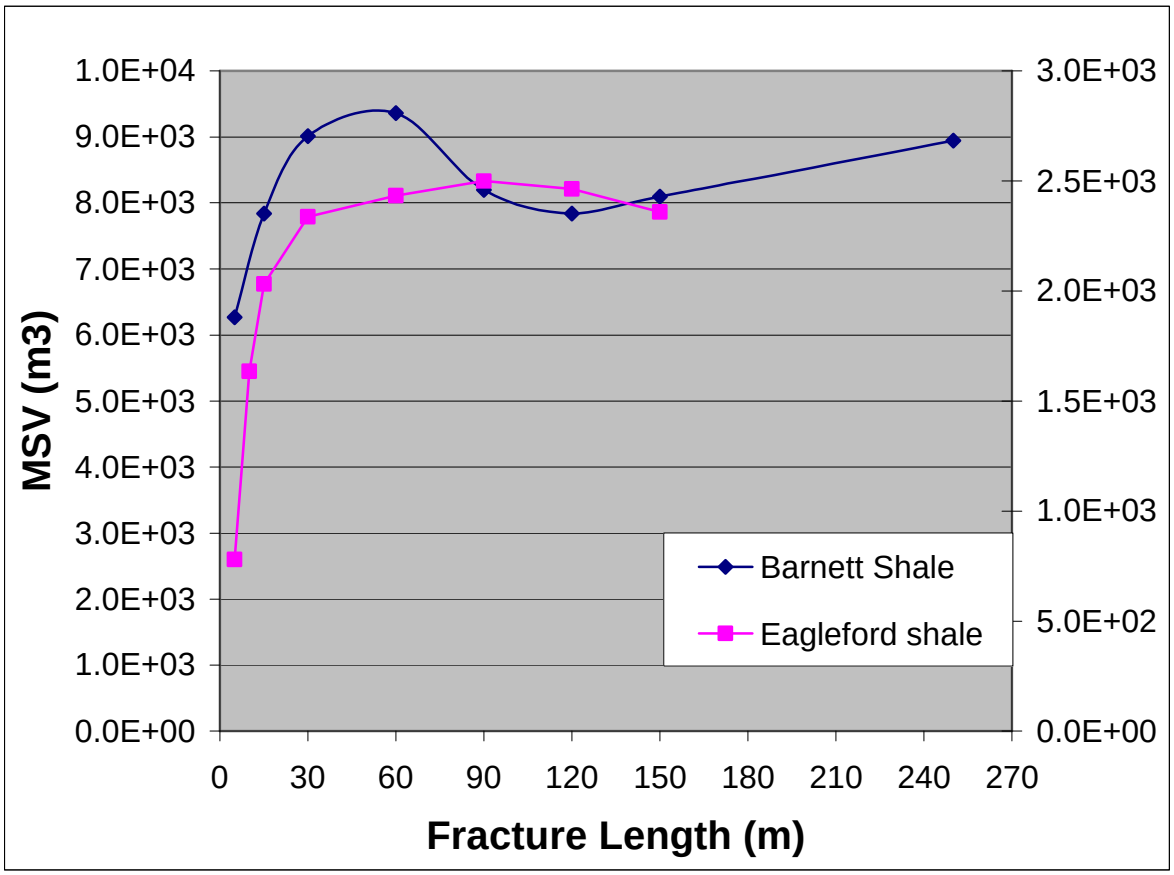

Figure 4-26: Plot of Microseismic Volume (MSV) versus Fracture length for the Barnett and Eagle Ford shale. The reservoir properties and other fracturing parameters used are listed in Table 4-3 and Table 4-4 respectively.

Chapter 5: Conclusions and Recommendations

In this study, numerical models for predicting fracture propagation path, and to observe the impact of geomechanics on induced microseismicity have been presented. The models developed are static in nature, i.e. propagation is not explicitly modeled, due to the convergence issues faced while modeling the fully coupled fracturing model.

The geomechanical model developed to predict the fracture propagation path in naturally fractured formations used a simple crossing criterion and was validated by comparing the model results with the experimental results published in the literature. It was observed that three parameters play a key role in determining the fracture propagation path; horizontal differential stress, orientation of weak planes, and shear strength of weak planes. The model indicates that higher differential stress and orthogonal weak planes (or, higher angle of orientation of weak planes with respect to the hydraulic fracture) promote the chances of hydraulic fracture crossing the weak planes without any change in propagation direction and vice-versa. Lower strength of weak planes (lower cohesion or lower friction angle) increases the possibility of slippage of weak planes under the influence of hydraulic fracture and propagation direction of fracture might change under these circumstances.

Another numerical model was developed to observe the impact of geomechanics on microseismicity in unconventional formations. The model was limited to observe the effect of only the fracture tip mechanism. The model used an implicit approach to model weak planes (i.e. weak planes were not explicitly modeled). It was observed that in certain formations where the reservoir pressure is low or moderate, the potential microseismicity zone is very small and is around 10 m. However, in formations where the reservoir pressure is high (overpressured formations), this zone extends to a larger

distance and can even extend to around 80-100 m around the fracture. The model was then used for multiple fractures in order to observe the effect of the fracture spacing in horizontal wells on microseismicity. The results indicated that there exists an optimum window for fracture spacing, where one can maximize the potential microseismicity and thus, the chances of fracture complexity. Effects of different parameters like stress state, fracture half-length, mechanical properties of the formation, fracturing pressure, strength of weak planes, etc. on the optimum fracture spacing window were observed. In particular, strength of the weak planes and their Young's modulus were found to be very dominant and highly sensitive parameters controlling the optimum fracture spacing window.

The presented models are static in nature and do not model the fracture propagation explicitly. Weng et al. (2011) developed a pseudo-3D unconventional fracturing model that takes into account the interaction of hydraulic fractures with the natural fractures. It inspires confidence because the model is very comprehensive in the sense that it includes stress shadowing effect, multiple fractures growing at the same time, interaction with natural fractures, proppant transport, etc. Thus, future work needs to be done to develop a fully coupled 3D fracture propagation model which takes into account all these factors and is computationally less expensive.

The model developed to observe the effect of geomechanics on microseismicity takes into account only the fracture tip mechanism. Other effects including fissure opening, leak-off, etc. could be further studied in the future. Finally, the model results for optimum fracture spacing should be compared with a systematic field study to make the model better and more accurate.

Bibliography

Adachi, J.I., and Detournay, E. 2002. Self-similar Solution of a Plane-Strain Fracture Driven by a Power-Law Fluid. International Journal For Numerical and Analytical Methods in Geomechanics, 26(6): 579-604.

Advani, S.H., Lee, T.S., and Lee, J.K. 1990. Three-Dimensional Modeling of Hydraulic Fractures in Layered Media: Part I-Finite Element Formulations. Journal of Energy Resources Technology, 112: 1-9.

Akulich, A.V., and Zvyagin, A.V. 2008. Interaction between Hydraulic and Natural Fractures. Fluid Dynamics, 43(3): 428-435.

Azeemuddin, M., Ghori, S.G., Saner, S., and Khan, M.N. 2002. Injection-Induced Hydraulic Fracturing in a Naturally Fractured Carbonate Reservoir: A Case Study from Saudi Arabia. Paper SPE 73784 presented at the SPE International Symposium & Exhibition on Formation Damage Control, Lafayette, U.S.A., 20-21 February.

Barenblatt, G.I. 1962. The Mathematical Theory of Equilibrium Cracks in Brittle Fracture. Advances in Applied Mechanics (1962), 7: 55-129.

Beugelsdijk, L.J.L., de Pater, C.J., and Sato, K. 2000. Experimental Hydraulic Fracture Propagation in a Multi-Fractured Medium. Paper SPE 59419-MS presented at the SPE Asia Pacific Conference on Integrated Modelling for Asset Management, Yokohoma, Japan, 25-26 April.

Blair, S.C., Thorpe, R.K., Heuze, F.E., and Shaffer, R.J. 1989. Laboratory Observations of the Effect of Geologic Discontinuities on Hydrofracture Propagation. Paper ARMA 89-0443 presented at The 30th U.S. Symposium on Rock Mechanics (USRMS), Morgantown, WV, U.S.A., 19-22 June.

Blanton, T.L. 1982. An Experimental Study of Interaction Between Hydraulically Induced and Pre-Existing Fractures. Paper SPE 10847 presented at the SPE Unconventional Gas Recovery Symposium, Pittsburgh, PA, U.S.A., 16-18 May.

Blanton, T.L. 1986. Propagation of Hydraulically and Dynamically Induced Fractures in Naturally Fractured Reservoirs. Paper SPE 15261 presented at the SPE Unconventional Gas Technology Symposium, Louisville, Kentucky, U.S.A., 18-21 May.

Britt, L.K., and Hager, C.J. 1994. Hydraulic Fracturing in Naturally Fractured Reservoir. Paper SPE 28717 presented at the SPE International Petroleum Conference and Exhibition, Veracruz, Mexico, 10-13 October.

Buller, D. 2010. Haynesville Shale. Presentation at Tulsa SPE Luncheon. 11th March.

Choate, P.R. 1992. A New 3D Hydraulic Fracture Simulator That Implicitly Computes the Fracture Boundary Movements. Paper SPE 24989-MS presented at the European Petroleum Conference, Cannes, France, 16-18 November.

Cleary, M.P. 1980. Comprehensive Design Formuale for Hydraulic Fracturing. Paper SPE 9259-MS presented at the SPE Annual Technical Conference and Exhibition, Dallas, Texas, U.S.A., 21-24 September.

Clifton, R.J., and Abou-Sayed, A.S. 1981. A Variational Approach to the Prediction of the Three-Dimensional Geometry of Hydraulic Fractures. Paper SPE 9879-MS presented at the SPE/DOE Low Permeability Gas Reservoirs Symposium, Denver, Colorado, U.S.A., 27-29 May.

Dahi-Taleghani, A. 2009. Analysis of Hydraulic Fracture Propagation in Fractured Reservoirs: An Improved Model for the Interaction Between Induced and Natural Fractures. Ph.D. thesis, The University of Texas at Austin, U.S.A.

Dahi-Taleghani, A., and Olson, J.E. 2011. Numerical Modeling of Multistranded-Hydraulic-Fracture Propagation: Accounting for the Interaction Between Induced and Natural Fractures. . SPE Journal, 16(3): 575-581.

Daneshy, A.A. 1974. Hydraulic Fracture Propagation in the Presence of Planes of Weakness. Paper SPE 4852-MS presented at the SPE European Spring Meeting, Amsterdam, Netherlands, 29-30 May.

de Pater, C.J., and Beugelsdijk, L.J.L. 2005. Experiments and Numerical Simulation of Hydraulic Fracturing in Naturally Fractured Rock. Paper ARMA 05-780 presented at The 40th U.S. Symposium on Rock Mechanics (USRMS), Anchorage, Alaska, 25-29 June.

Desroches, J., Detournay, E., Lenoach, B., Papanastasiou, P., Pearson, J.R., Thiercelin, M., and Cheng, A. 1994. The Crack Tip Region in Hydraulic Fracturing. Proceedings of the Royal Society of London, Series A (447): 39-48.

Detournay, E., and Garagash, D. 2003. The Tip Region of a Fluid-Driven Fracture in a Permeable Elastic Solid. Journal of Fluid Mechanics, 494: 1-32.

Doe, T.W., and Boyce, G. 1989. Orientation of Hydraulic Fractures in Salt under Hydrostatic and Non-Hydrostatic Stresses. International Journal of Rock Mechanics and Mining Sciences & Geomechanics Abstracts, 26(6): 605-611.

Fisher, M.K., Wright, C.A., Davidson, B.M., Goodwin, A.K., Fielder, E.O., Buckler, W.S., and Steinsberger, N.P. 2005. Integrating Fracture-Mapping Technologies to

Improve Stimulations in the Barnett Shale. SPE Production & Facilities, 20(2): 85-93. SPE 77441-PA-P.

Geertsma, J., and de Klerk, F. 1969. A Rapid Method of Predicting Width and Extent of Hydraulically Induced Fractures. Journal of Petroleum Technology, 21 (12): 1571-1581. SPE 2458-PA.

Gu, H., and Leung, K.H. 1993. 3D Numerical Simulation of Hydraulic Fracture Closure with Application to Minifracture Analysis. Journal of Petroleum Technology, 45(3): 206-211. SPE 20657-PA.

Gu, H., Weng, X., Lund, J., Mack, M., Ganguly, U., and Suarez-Rivera, R. 2011. Hydraulic Fracture Crossing Natural Fracture at Non-Orthogonal Angles, A Criterion, Its Validation and Applications. Paper SPE 139984 presented at the SPE Hydraulic Fracturing Technology Conference and Exhibition, The Woodlands, Texas, U.S.A., 24-26 January.

Howard, G.C., and Fast, C.R. 1957. Optimum Fluid Characteristics for Fracture Extension. Paper API 57-261 presented at the Drilling and Production Practice Meeting, Tulsa, Oklahoma, U.S.A., April.

Hubbert, M.K., and Willis, D.G. 1957. Mechanics of Hydraulic Fracturing. Paper SPE 686-G presented at Petroleum Branch Fall Meeting, Los Angeles, California, U.S.A., 14-17 October.

Jeffrey, R.G., Vandamme, L., and Roegiers, J.C. 1987. Mechanical Interactions in Branched or Subparallel Hydraulic Fractures. Paper SPE 16422 presented at the SPE Low Permeability Reservoirs Symposium, Denver, Colorado, U.S.A., 18-19 May.

Jeffrey Jr., R.G., Brynes, R.P., Lynch, P.J., and Ling, D.J. 1992. An Analysis of Hydraulic Fracture and Mineback Data for a Treatment in the German Creek Coal Seam. Paper SPE 24362-MS presented at the SPE Rocky Mountain Regional Meeting, Casper, Wyoming, U.S.A., 18-21 May.

Khristianovic, S.A., and Zheltov, Y.P. 1955. Formation of Vertical Fractures by Means of Highly Viscous Liquid. Proceedings: Fourth World Petroleum Congress (1955) II: 579-586.

LaFollette, R. 2010. Key considerations for hydraulic fracturing of gas shales. Online Webinar presented at the AAPG E-Seminar, 9th September.

Lam, K.Y., and Cleary, M.P. 1984. Slippage and Re-Initiation of (Hydraulic) Fractures at Frictional Interfaces. International Journal for Numerical and Analytical Methods in Geomechanics, 8(6): 589-604.

Lam, K.Y., Cleary, M.P., and Barr, D.T. 1986. A Complete Three-Dimensional Simulator for Analysis and Design of Hydraulic Fracturing. Paper SPE 15266-MS presented at the SPE Unconventional Gas Technology Symposium, Kentucky, Louisville, U.S.A., 18-21 May.

Lamont, N., and Jessen, F.W. 1963. The Effects of Existing Fractures in Rocks on the Extension of Hydraulic Fractures. Journal of Petroleum Technology, 15(2): 203-209. SPE 419-PA.

Lecampion, B. 2009. An Extended Finite Element Method for Hydraulic Fracture Problems. Communications in Numerical Methods in Engineering, 25(2): 121-133.

Lenoach, B. 1995. The Crack Tip Solution for Hydraulic Fracturing in a Permeable Solid. Journal of Mechanics of Physics and Solids, 43(7): 1025-1043.

Mayerhofer, M.J., Lolon, E.P., Youngblood, J.E., and Heinze, J.R. 2006. Integration of Microseismic Fracture Mapping Results with Numerical Fracture Network Production Modeling in the Barnett Shale. Paper SPE 102103 presented at the SPE Annual Technical Conference and Exhibition, San Antonio, Texas, U.S.A., 24-27 September.

Morita, N., Whitfill, D.L., and Wahl, H.A. 1988. Stress-Intensity Factor and Fracture Corss-Sectional Shape Predictions from a Three-Dimensional Model for Hydraulically Induced Fractures. Journal of Petroleum Technology, 40(10): 1329-1342. SPE 14262-PA.

Murphy, H.D., and Fehler, M.C. 1986. Hydraulic Fracturing of Jointed Formations. Paper SPE 14088 presented at the SPE International Meeting on Petroleum Engineering, Beijing, China, 17-20 March.

Naceur, K.B., Thiercelin, M., and Touboul, E. 1990. Simulation of Fluid Flow in Hydraulic Fracturing: Implications for 3D Propagation. SPE Production Engineering, 5(2): 133-141. SPE 16032-PA.

Navigant Consulting 2008. North American Natural Gas Supply Assessment. Report.

Nolte, K.G., and Smith, M.B. 1981. Interpretation of Fracturing Pressures. Journal of Petroleum Technology, 33(9): 1767-1775. SPE 8297-PA.

Nordgren, R.P. 1972. Propagation of a Vertical Hydraulic Fracture. SPE Journal, 12(4): 306-314.

Olson, J.E. 1993. Joint Pattern Development: Effects of Subcritical Crack Growth and Mechanical Crack Interaction. Journal of Geophysical Research, 98(7): 12251-12265.

Olson, J.E. 1995. Fracturing from Highly Deviated and Horizontal Wells: Numerical Analysis of Non-Planar Fracture Propagation. Paper SPE 29573 presented at the SPE Rocky Mountain Regional/Low Permeability Reservoirs Symposium, Denver, Colorado, U.S.A., 20-22 March.

Olson, J.E. 2008. Multi-fracture propagation modeling: Applications to hydraulic fracturing in shales and tight gas sands. Paper ARMA 08-327 presented at the 42nd US Rock Mechanics Symposium and 2nd U.S.-Canada Rock Mechanics Symposium, San Francisco, U.S.A., June 29- July 2.

Paul, J.R., and Taylor, L.C. 1958. Increased secondary recovery by hydraulic fracturing. Paper SPE 1051-G presented at the Petroleum Conference on Production and Reservoir Engineering, Tulsa, Oklahoma, U.S.A., 20-21 March.

Perkins, T.K., and Kern, L.R. 1961. Widths of Hydraulic Fractures. Journal of Petroleum Technology, 13(9): 937-949.

Pollard, D.D., and Segall, P. 1987. Theoretical Displacement and Stresses Near Fractures in Rock: With Applications to Faults, Joints, Veins, Dikes, and Solution Surfaces. In B.K. Atkinson, ed., Fracture Mechanics of Rock, Academic Press, Inc., pp. 277-349.

Rahman, S.S., Rahman, M.K., and Hossain, M.M. 2000. Hydraulic Fracture Initiation and Propagation: Roles of Wellbore Trajectory, Perforation and Stress Regimes. Journal of Petroleum Science and Engineering, 27: 129-149.

Rahman, M.M., and Rahman, S.S. 2009. A Fully Coupled Numerical Poroelastic Model to Investigate Interaction Between Induced Hydraulic Fracture and Pre-Existing Natural Fracture in a Naturally Fractured Reservoir: Potential Application in Tight Gas and Geothermal Reservoirs. Paper SPE 124269 presented at the SPE Annual Technical Conference and Exhibition, New Orleans, Louisiana, U.S.A., 4-7 October.

Renshaw, C.E., and Pollard, D.D. 1995. An Experimentally Verified Criterion for Propagation across Unbonded Frictional Interfaces in Brittle, Linear Elastic Materials. International Journal of Rock Mechanics and Mining Sciences, 32(3): 237-249.

Rodgerson, J.L. 2000. Impact of Natural Fractures in Hydraulic Fracturing of Tight Gas Sands. Paper SPE 59540 presented at the SPE Permian Basin Oil and Gas Recovery Conference, Midland, Texas, U.S.A., 21-23 March.

Roussel, N.P., and Sharma, M.M. 2011. Optimizing Fracture Spacing and Sequencing in Horizontal-Well Fracturing. SPE Productions & Completions 26(2): 173-184.

Settari, A., and Cleary, M.P. 1984. Three-Dimensional Simulation of Hydraulic Fracturing. Journal of Petroleum Technology 36(7): 1177-1190.

Sharma, M.M., Gadde, P.B., Sullivan, R., Sigal, R., Fielder, R., Copeland, D., Griffin, L., and Weijers, L. 2004. Slick Water and Hybrid Fracs in the Bossier: Some Lessons Learnt. Paper SPE 89876 presented at the SPE Annual Technical Conference and Exhibition, Houston, U.S.A., 26-29 September.

Siebrits, E., and Peirce, A.P. 2002. An Efficient Multi-Layer Planar 3D Fracture Growth Algorithm using a Fixed Mesh Approach. International Journal For Numerical Methods in Engineering, 53: 691-717.

Simonson, E.R., Abou-Sayed, A.S., and Clifton, R.J. 1978. Containment of Massive Hydraulic Fractures. SPE Journal, 18(1): 27-32.

Spence, D.A., and Sharp, P.W. 1985. Self-Similar Solution for Elastohydrodynamic Cavity Flow. Proceedings of the Royal Society of London, Series A (400), pp. 289-313.

Thomspon, J.W., Fan, L., Grant, D., Martin, R.B., Kanneganti, K.T., and Lindsay, G.J. 2011. An Overview of Horizontal-Well Completions in the Haynesville Shale. Journal of Canadian Petroleum Technology, 50(6): 22-35.

Vermeer, P.A., and de Borst, R. 1984. Non-Associated Plasticity for Soils, Concrete and Rock. Heron, 29(3): 3-64.

Vinod, P.S., Flindt, M.L., Card, R.J., and Mitchell, J.P. 1997. Dynamic Fluid-Loss Studies in Low-Permeability Formations with Natural Fractures. Paper SPE 37486 presented at the SPE Production Operations Symposium, Oklahoma, 9-11 March.

Warpinski, N.R., and Teufel, L.W. 1987. Influence of Geologic Discontinuities on Hydraulic Fracture Propagation. Journal of Petroleum Technology, 39(2): 209-220. SPE 13224-PA.

Warpinski, N.R., Mayerhofer, M.J., Vincent, M.C., Cipolla, C.L., and Lolon, E.P. 2008. Stimulating Unconventional Reservoirs: Maximizing Network Growth while Optimizing Fracture Conductivity. Paper SPE 114173 presented at the 2008 SPE Unconventional Reservoirs Conference, Keystone, Colorado, U.S.A., 10-12 February.

Wawersik, W.R., and Stone, C.M. 1989. A Characterization of Pressure Records in Inelastic Rock Demonstrated by Hydraulic Fracturing Measurements in Salt. International Journal of Rock Mechanics and Mining Sciences & Geomechanics Abstracts, 26(6): 613-627.

Weng, X., Kresse, O., Cohen, C., Wu, R., and Gu, H. 2011. Modeling of Hydraulic Fracture Network Propagation in a Naturally Fractured Formation. Paper SPE 140253 presented at the SPE Hydraulic Fracturing Technology Conference and Exhibition, The Woodlands, Texas, U.S.A., 24-26 January.

Yew, C.H., and Liu, G.F. 1993. Fracture Tip and Critical Stress Intensity Factor of a Hydraulically Induced Fracture. SPE Production and Facilities 8(3): 171-177. SPE 22875-PA.

Zhang, X., and Sanderson, D.J. 2002. Numerical Modeling and Analysis of Fluid Flow and Deformation of Fractured Rock Masses. Permagon press.

Zhao, X.P., and Young, R.P. 2009. Numerical Simulation of Seismicity Induced by Hydraulic Fracturing in Naturally Fractured Reservoirs. Paper SPE 124690 presented at the SPE Annual Technical Conference and Exhibition, New Orleans, Louisiana, U.S.A., 4-7 October.

Zhou, J., Chen, M., Jin, Y., and Zhang, G. 2008. Analysis of Fracture Propagation Behavior and Fracture Geometry using a Tri-Axial Fracturing System in Naturally Fractured Reservoirs. International Journal of Rock Mechanics and Mining Sciences, 45(7): 1143-1152.